**Title**

Structure-based Design of Diagnostics and Therapeutics for Neurodegenerative Diseases



**Author**

Pan, Hope

**Publication Date**

2024

Peer reviewed|Thesis/dissertation

UNIVERSITY OF CALIFORNIA

Los Angeles

# Structure-based Design of Diagnostics and Therapeutics for Neurodegenerative Diseases

A dissertation submitted in partial satisfaction of the requirements for the degree Doctor of Philosophy in Molecular Biology

by

Hope Pan

2024

ABSTRACT OF THE DISSERTATION

Structure-based Design

of Diagnostics and Therapeutics

for Neurodegenerative Diseases

by

Hope Pan

Doctor of Philosophy in Molecular Biology

University of California, Los Angeles, 2024

Professor David S. Eisenberg, Chair

Alzheimer's disease (AD) and Parkinson's disease (PD) are the most common neurodegenerative diseases. Although AD is a disease of dementia and PD is predominantly a motor disease, both diseases are characterized by histological hallmarks formed from aggregates of amyloid-forming proteins. Amyloid plaques and neurofibrillary tangles, composed of amyloid-β and tau respectively, are the hallmarks of AD while Lewy bodies, composed of α-synuclein (α-syn), are the hallmarks of PD. Amyloid-forming proteins such as amyloid-β, tau, and α-syn are soluble and functional in their monomeric state. They can misfold and aggregate into fibrils, which themselves aggregate to form amyloid plaques, neurofibrillary tangles, and Lewy bodies. There is a tight correlation between neurofibrillary tangle formation and progression of AD, and between Lewy body formation and progression of PD, so it has long been hypothesized that amyloid fibrils are toxic and contribute to the pathogenesis of AD and PD. Supporting this hypothesis are studies demonstrating that existing amyloid fibrils can

propagate or “seed” the formation of additional fibrils among cultured cells and in mice. Using the wealth of atomic resolution structures of amyloid fibrils determined by x-ray crystallography and cryo-electron microscopy, the Eisenberg group has designed peptides, antibodies, and small molecules that target tau and α-syn fibrils. In this dissertation research, I focus on characterizing three of these structure-based designs as potential diagnostics and therapeutics for AD and PD. First, I characterize magnetic nanoparticles functionalized with an α-syn-targeting peptide and determine that they can be used as an MRI contrast agent to distinguish mice with α-syn pathology from wild-type control mice. Second, I characterize a bivalent nanobody that can inhibit seeding by post-mortem brain extracts from AD patients and determine it can cross the blood-brain barrier in mice. Third, I characterize three small molecules that can disaggregate AD brain-extracted fibrils and determine that they can each reduce levels of aggregated tau in mice with tau pathology. Together, the studies in this dissertation demonstrate the potential of using structure-based design of diagnostics and therapeutics for diseases caused by the misfolding of amyloid-forming proteins.

The dissertation of Hope Pan is approved.

Feng Guo

Gregory M. Cole

Harry V. Vinters

Lin Jiang

David S. Eisenberg, Committee Chair

University of California, Los Angeles

2024

TABLE OF CONTENTS

LIST OF FIGURES AND TABLES

# ACKNOWLEDGEMENTS

First and foremost, I thank my advisor, David Eisenberg, who gave me the opportunity to do my dissertation research in his group four years ago. David has dedicated over 60 years of his life to science and over 20 years of his career to studying protein misfolding diseases. He is a model for the kind of scientist I hope to be one day. In his research group, he has created an ideal environment for success by taking on the brightest students and post-doctoral scholars, hiring the most knowledgeable staff to guide them, and encouraging us all to collaborate with one another. He has also created an ideal environment for enjoying our work with daily coffee hour breaks and weekly book clubs. My graduate training experience would not have been the same in any other research group.

In addition to David, I thank two other leaders in our group, Dr. Duilio Cascio and Dr. Michael Sawaya. Duilio is responsible for keeping all the x-ray crystallography and electron microscopy equipment running, which is a monumental task. He also leads M230, the structural biology course that all first-year students take, which formed the foundation of my career in structural biology. Michael is an excellent scientist, but even more, he is an amazing person and friend. He is kind to everyone and incredibly generous with his time, his knowledge, and his brother's baked goods. David's group would not be the same without these two great scientists.

I thank my three co-authors: Dr. Melinda Balbirnie, who I worked with on the project outlined in Chapter 2 of my dissertation, Dr. Romany Abskharon, who I worked with on the project outlined in Chapter 3, and Xinyi Cheng, who I worked with on the project outlined in Chapter 4. Melinda was my mentor when I first rotated in the lab in 2019. Since then, her meticulousness and attention to detail has been the perfect complement to my quick work style. Romany is a data

producing machine and I have been in awe of his work ethic since I joined the lab. Our work together led to my first first-author paper in my graduate training, and it gave me the confidence to finish my other dissertation projects. Xinyi has been a great colleague and friend as we both strived to finish our graduate training this year. We worked on complementary sides of the same project, so we were able to give each other advice and encourage each other to the finish line.

I thank Dr. Paul Seidler and Dr. Kevin Murray, who are both now alumni of UCLA, for mentoring me when I first joined the group in 2020. I would have been directionless that year amidst the lockdowns and restrictions if it were not for Paul's willingness to train me and Kevin's invitation to join his projects.

Most of all, I thank my partner in the lab, Dr. Ke Hou. Ke and I were the first in our structural biology group to work extensively with mouse models of Alzheimer's disease and Parkinson's disease. It was challenging paving the way for new techniques in our group, and Ke and I could not have done it without being by each other's side. In addition to learning laboratory techniques from one another, we learned much about each other's cultures and countries and became lifelong friends in the process.

I thank the many collaborators outside our group that I had the privilege of learning from the past four years. Dr. Sally Frautschy and Dr. Gregory Cole taught me about mouse models of Alzheimer's disease and Parkinson's disease. Dr. Neil Harris and Dr. Naomi Sta. Maria taught me about magnetic resonance imaging of mice. Dr. Gazmend Elezi and Dr. Julian Whitelegge taught me how to use LC/MS for pharmacokinetic studies. Eileen Olivares, Dr. Joseph Loo, and Dr. Rachel Loo were invaluable collaborators on studies outlined in Chapter 3. Christopher Kazu Williams and Dr. Harry Vinters provided all the patient tissue used in these studies. Dr. Hilda Mirbaha taught me how to interpret immunohistochemical staining.

I thank my committee: Dr. Feng Guo, Dr. Gregory Cole, Dr. Harry Vinters, and Dr. Lin Jiang. Feng has been an important advisor to me as my Molecular Biology Institute Home Area Director, Greg has co-mentored me with David and complemented David's structural biology expertise with his mouse model expertise, Harry is an excellent physician who has inspired my own interest in a career in neuropathology, and Lin has given me guidance since being my written qualifying exam advisor.

I thank the Medical Scientist Training Program for giving me the opportunity to pursue my graduate education at UCLA. I thank my MSTP faculty advisors Dr. Maureen Su, Dr. Olujimi Ajijola, and Dr. David Dawson and I thank my MSTP student advisors and friends Dr. Bryce Bajar and Dr. Melina Mastrodimos. I thank the 2018 MSTP Cohort and Nicholas Cho for taking the MD-PhD journey alongside me.

I thank the generous funding I have received throughout my medical and graduate training: the UCLA-Caltech Medical Scientist Training Program (T32-GM08042), the UCLA Chemistry-Biology Interface Training Grant (T32-GM008496), and the Ruth L. Kirschstein National Research Service Award (F30-AG077832-01A1).

I thank the donors and their families without whom this research would have not been possible.

In addition to those who have taught me at UCLA, I thank the mentors that helped me reach my dream of graduate school. I thank my parents, Yingdong Pan and Xin Wang, for being my earliest scientific mentors. My mom instilled a love for math in me from a young age, and my dad helped me complete my first science project titrating Vitamin C in orange juice when I was 13 years old. I thank Dr. Lei Zhou at the University of Florida and Dr. James Bliska at Stony

Brook University for giving me early start on research during high school. I thank Dr. Ana Carneiro and Dr. Michael Stone at Vanderbilt University for being my research advisors in college and helping me develop an important foundation for graduate school.

Finally, I thank my friends and family for their unwavering support during my graduate training. I thank my brother, Harold Pan, who has grown up to be a kind and caring friend and my biggest supporter. I thank the Cascio family and the Chao family for hosting me during the Thanksgiving and Christmas holidays when I stayed in LA to continue working on my research projects. I thank Victoria Mevs, Brian Lee, Sayali Khare, Brandon Wanke, Terri Shih, and Marisa Mekkittikul for making my time outside of the laboratory just as enjoyable as my time in the laboratory during the past four years.

VITA

## Education

Vanderbilt University — December 2017
B.A. Chemistry and Applied Mathematics, *Cum Laude*

## Positions and Scientific Appointments

| | |
|---|---|
| 2020-Present | PhD Candidate, UCLA, Eisenberg Lab |
| 2019 | Rotation Student, UCLA Eisenberg Lab |
| 2018 | Rotation Student, UCLA, Yang Lab |
| 2016-2017 | Undergraduate Research Assistant / Beckman Scholar, Vanderbilt University, Stone Lab |
| 2014-2016 | Undergraduate Research Assistant, Vanderbilt University, Carneiro Lab |
| 2010-2014 | High School Research Assistant, University of Florida, Zhou Lab |
| 2013 | Simons Summer Research Fellow, Stony Brook University, Bliska Lab |

## Other Experience and Professional Memberships

| | |
|---|---|
| 2018 | MCAT & GRE Instructor, Kaplan Test Prep |
| 2016-2017 | Member, AAAS |
| 2014-2017 | Member, American Chemical Society |
| 2016-2017 | President, American Chemical Society, Vanderbilt University Chapter |
| 2015-2017 | Volunteer (Inpatient Visitor), Vanderbilt University Medical Center |

## Honors

| | |
|---|---|
| 2023-Present | F30 Ruth L. Kirschstein National Research Service Award (NRSA) |
| 2021-2023 | T32 UCLA Chemistry-Biology Interface Training Program |
| 2018 | Phi Beta Kappa, National Honor Society |
| 2017 | Highest Honors in Chemistry, Vanderbilt University |
| 2016 – 2017 | Scholarship, Beckman Scholars Program |
| 2014 | Scholarship, AMETEK National Merit Scholarship Program |
| 2014 | Scholarship, Plum Creek Community Scholar |

## Publications

1. Dohn MR, Kooker CG, Bastarache L, Jessen T, Rinaldi C, Varney S, Mazalouskas MD, **Pan H**, Oliver KH, Velez Edwards DR, Sutcliffe JS, Denny JC, Carneiro AMD. The Gain-of-Function Integrin β3 Pro33 Variant Alters the Serotonin System in the Mouse Brain. *J Neurosci.* 2017 Nov 15;37(46):11271-11284. doi: 10.1523/JNEUROSCI.1482-17.2017. Epub 2017 Oct 16. PMID: 29038237; PMCID: PMC5688530.
2. Yuan Y, DiCiaccio B, Li Y, Elshikha AS, Titov D, Brenner B, Seifer L, **Pan H**, Karic N, Akbar MA, Lu Y, Song S, Zhou L. Anti-inflammaging effects of human alpha-1 antitrypsin. Aging Cell. 2018 Feb;17(1):e12694. doi: 10.1111/acel.12694. Epub 2017 Oct 17. PMID: 29045001; PMCID: PMC5770780.

3. **Pan H**, Dohn MR, Kingston R, Carneiro AMD. Integrin αVβ3 Function Influences Citalopram Immobility Behavior in the Tail Suspension Test. Front Neurosci. 2019 Feb 6;13:70. doi: 10.3389/fnins.2019.00070. PMID: 30787865; PMCID: PMC6372549.
4. Bassett B, Subramaniyam S, Fan Y, Varney S, **Pan H**, Carneiro AMD, Chung CY (2021) Minocycline alleviates depression-like symptoms by rescuing decrease in neurogenesis in dorsal hippocampus via blocking microglia activation/phagocytosis. *Brain Behav Immun.* Jan;91:519-530. doi: 10.1016/j.bbi.2020.11.009. Epub 2020 Nov 8. PMID: 33176182.
5. Bamberger SN, Malik CK, Voehler MW, Brown SK, **Pan H**, Johnson-Salyard TL, Rizzo CJ, Stone MP. Configurational and Conformational Equilibria of N6-(2-Deoxy-d-erythropentofuranosyl)-2,6-diamino-3,4-dihydro-4-oxo-5- N-methylformamidopyrimidine (MeFapy-dG) Lesion in DNA. *Chem Res Toxicol.* 2018 Sep 17;31(9):924-935. doi: 10.1021/acs.chemrestox.8b00135. Epub 2018 Aug 31. PMID: 30169026; PMCID: PMC6352716.
6. Murray KA, Hughes MP, Hu CJ, Sawaya MR, Salwinski L, **Pan H**, French SW, Seidler PM, Eisenberg DS. Identifying amyloid-related diseases by mapping mutations in low-complexity protein domains to pathologies. *Nat Struct Mol Biol.* 2022 Jun;29(6):529-536. doi: 10.1038/s41594-022-00774-y. Epub 2022 May 30. PMID: 35637421; PMCID: PMC9205782.
7. Murray KA, Hu CJ, Griner SL, **Pan H,** Bowler JT, Abskharon R, Rosenberg GM, Seidler PM, Eisenberg DS. De novo designed protein inhibitors of amyloid aggregation and seeding. *Proc Natl Acad Sci U S A.* 2022 Jul; In Press.
8. Seidler PM*, Murray KA*, Boyer DR*, Ge P, Sawaya MR, Hu CJ, Cheng X, Abskharon R, **Pan H,** DeTure MA, Williams CK, Dickson DW, Vinters HV, Eisenberg DS. Structure-based discovery of small molecules that disaggregate tau fibrils from Alzheimer's disease. *Nat Commun.* 2022 Aug; Accepted.
9. Murray KA, Hu CJ, **Pan H**, Lu J, Abskharon R, Bowler JT, Rosenberg GM, Williams CK, Elezi G, Balbirnie M, Faull KF, Vinters HV, Seidler PM, Eisenberg DS. Small molecules disaggregate alpha-synuclein and prevent seeding from patient brain-derived fibrils. Proc Natl Acad Sci U S A. 2023 Feb 14;120(7):e2217835120. doi: 10.1073/pnas.2217835120. Epub 2023 Feb 9. PMID: 36757890; PMCID: PMC9963379.
10. Tayeb-Fligelman E, Bowler JT, Tai CE, Sawaya MR, Jiang YX, Garcia G Jr, Griner SL, Cheng X, Salwinski L, Lutter L, Seidler PM, Lu J, Rosenberg GM, Hou K, Abskharon R, **Pan H**, Zee CT, Boyer DR, Li Y, Anderson DH, Murray KA, Falcon G, Cascio D, Saelices L, Damoiseaux R, Arumugaswami V, Guo F, Eisenberg DS. Low complexity domains of the nucleocapsid protein of SARS-CoV-2 form amyloid fibrils. Nat Commun. 2023 Apr 25;14(1):2379. doi: 10.1038/s41467-023-37865-3. PMID: 37185252; PMCID: PMC10127185.
11. Abskharon R*, **Pan H***, Sawaya MR, Seidler PM, Olivares EJ, Chen Y, Murray KA, Zhang J, Lantz C, Bentzel M, Boyer DR, Cascio D, Nguyen BA, Hou K, Cheng X, Pardon E, Williams CK, Nana AL, Vinters HV, Spina S, Grinberg LT, Seeley WW, Steyaert J, Glabe CG, Ogorzalek Loo RR, Loo JA, Eisenberg DS. Structure-based design of nanobodies that inhibit seeding of Alzheimer's patient-extracted tau fibrils. Proc Natl Acad Sci U S A. 2023 Oct 10;120(41):e2300258120. doi: 10.1073/pnas.2300258120. Epub 2023 Oct 6. PMID: 37801475; PMCID: PMC10576031.
12. Hou K, **Pan H**, Shahpasand-Kroner H, Hu C, Abskharon R, Seidler P, Mekkittikul M, Balbirnie M, Lantz C, Sawaya MR, Dolinsky JL, Jones M, Zuo X, Loo JA, Frautschy S, Cole G, Eisenberg DS. D-peptide-magnetic nanoparticles fragment tau fibrils and rescue behavioral deficits in a mouse model of Alzheimer's disease. Sci Adv. 2024 May 3;10(18):eadl2991. doi: 10.1126/sciadv.adl2991. Epub 2024 May 1. PMID: 38691615.

*Denotes equal contribution

CHAPTER 1

# Introduction

During my graduate training, I had the opportunity to work on multiple projects. Tying these different projects together is the common theme of structure-based design of diagnostics and therapeutics for diseases caused by the misfolding of amyloid-forming proteins.

Chapter 2 is a reprint of the manuscript currently under review titled “Liganded magnetic nanoparticles for magnetic resonance imaging of α-synuclein”. This work was co-authored by me and Dr. Melinda Balbirnie. Melinda identified a 25-residue peptide, R8, that can bind α-synuclein. She functionalized a magnetic nanoparticle with this peptide, forming R8-LMNPs, and found that R8-LMNPs can bind *ex vivo* fibrils extracted from the brains of dementia with Lewy bodies (DLB) and multiple systems atrophy (MSA) patients. I administered R8-LMNPs to mice with α-synuclein pathology and found that they can cross the blood-brain barrier with mannitol adjuvant. With Dr. Ke Hou and Dr. Naomi Sta. Maria, I performed magnetic resonance imaging (MRI) of mice with α-synuclein pathology and found that R8-LMNPs can be used an MRI contrast agent to distinguish mice with α-synuclein pathology from wild-type controls. The work in this chapter provides evidence for the potential of magnetic nanoparticles that target α-synuclein for diagnosis of synucleinopathies.

Chapter 3 is a reprint of the published manuscript titled “Structure-based design of nanobodies that inhibit seeding of Alzheimer’s patient-extracted tau fibrils”. This work was co-authored by Dr. Romany Abskharon and me. Romany grafted tau-capping peptide inhibitors, designed by Dr. Paul Seidler, into the complementarity determining region 3 of a nanobody scaffold to create tau-capping nanobodies. These nanobodies block seeding by post-mortem brain extracts from

Alzheimer's disease (AD) and progressive supranuclear palsy (PSP) patients in a tau aggregation cell culture model. Romany then designed a bispecific nanobody composed of a nanobody that targets a receptor on the blood-brain barrier and a tau capping nanobody inhibitor, conjoined by a flexible linker. With Eileen Oliveras, I administered the bispecific nanobody to wild-type mice and determined that they can cross the blood-brain barrier using quantitative liquid chromatography-tandem mass spectrometry. The work in this chapter suggests that structure-based design of nanobodies that target sequences that drive protein aggregation may be a promising approach to inhibit seeding of tau in AD and related tauopathies.

Chapter 4 is a reprint of a manuscript in preparation titled "Structure-based discovery of small molecules that disaggregate tau fibrils in a mouse model of tauopathy". This work was co-authored by me and Xinyi Cheng. In a previous study, Dr. Paul Seidler, Dr. Kevin Murray, and Dr. David Boyer discovered a small molecule, CNS-11, that can prevent seeding by AD post-mortem brain extract in a tau aggregation cell culture model and can disaggregate AD brain-derived fibrils *in vitro*. With Tyler Halladay, I discovered that eight weeks of treatment with CNS-11 significantly reduced levels of insoluble tau in the hippocampus of mice with tau pathology. With Jeffrey Zhang, Xinyi screened four chemical analogs of CNS-11 and identified two that can disaggregate AD brain-derived fibrils *in vitro* and can prevent seeding by AD post-mortem brain extract in a tau aggregation cell culture model: CNS-11D and CNS-11G. With Dr. Ke Hou, I discovered that eight weeks of treatment with either CNS-11D or CNS-11G significantly reduced levels of insoluble tau in the hippocampus of mice with tau pathology. This work in this chapter suggests the potential of structure-based discover of small molecules for targeting tau in AD and related tauopathies.

CHAPTER 2

# Liganded magnetic nanoparticles for magnetic resonance imaging of α-synuclein

Hope Pan[1]*, Melinda Balbirnie[1]*, Ke Hou[1], Naomi S. Sta Maria[2], Shruti Sahay[1], Paul Denver[3,4], Stefano Lepore[5], Mychica Jones[3,4], Xiaohong Zuo[3.4], Chunni Zhu[4,6], Hilda Mirbaha[7], Hedieh Shahpasand-Kroner[3,4], Marisa Mekkittikul[3,4], Jiahui Lu[1], Carolyn Hu[1], Xinyi Cheng[1], Romany Abskharon[1], Michael R. Sawaya[1], Christopher K. Williams[4,7], Harry V. Vinters[4,7], Russell E. Jacobs[2], Neil G. Harris[5], Gregory M. Cole[3,4], Sally A. Frautschy[3,4], David S. Eisenberg[1]**

[1]Department of Chemistry and Biochemistry, Department of Biological Chemistry, UCLA-DOE Institute, Molecular Biology Institute, and Howard Hughes Medical Institute, UCLA, Los Angeles CA, 90095; [2]Department of Research Physiology, Department of Neuroscience, Keck School of Medicine at USC, Los Angeles, CA 90033; [3]Geriatric Research Education and Clinical Center, Greater Los Angeles Veterans Affairs Healthcare System, West Los Angeles VA Medical Center, Los Angeles, CA, 90073; [4]Department of Neurology, David Geffen School of Medicine at UCLA, Los Angeles, CA, 90095; [5]Department of Neurosurgery, David Geffen School of Medicine at UCLA, Los Angeles, CA 90095; [6]Brain Research Institute Electron Microscopy Core Facility, David Geffen School of Medicine, UCLA, Los Angeles, CA 90095; [7]Department of Pathology and Laboratory Medicine, David Geffen School of Medicine, UCLA, Los Angeles, CA 90095

*These authors contributed equally

**To whom correspondence should be addressed: David S. Eisenberg: University of California-Los Angeles 611 Charles E Young Drive, Boyer 201, Los Angeles, CA 90095; david@mbi.ucla.edu; Tel. (310) 825-3754, Fax. (310) 206-3914

**Abstract**

Aggregation of the protein α-synuclein (α-syn) is the histopathological hallmark of neurodegenerative diseases such as Parkinson's disease (PD), dementia with Lewy bodies (DLB), and multiple system atrophy (MSA), which are collectively known as synucleinopathies. Currently, patients with synucleinopathies are diagnosed by physical examination and medical history, often at advanced stages of disease. Because synucleinopathies are associated with α-syn aggregates, and α-syn aggregation often precedes onset of symptoms, detecting α-syn aggregates would be a valuable early diagnostic for patients with synucleinopathies. Here, we design a liganded magnetic nanoparticle (LMNP) functionalized with an α-syn-targeting peptide to be used as a magnetic resonance imaging (MRI)-based biomarker for α-syn. Our LMNPs bind to aggregates of α-syn *in vitro* and can be used to distinguish mice with α-synucleinopathy from age-matched, wild-type mice by MRI *in vivo*. These results provide evidence for the potential of magnetic nanoparticles that target α-syn for diagnosis of synucleinopathies. (149/150 words)

**Teaser**

Liganded magnetic nanoparticles offer a possible early diagnostic for Parkinson's and related diseases. (103/125 characters)

**Introduction**

Parkinson's disease (PD) is a neurodegenerative disease that affects nearly 1 million people in the United States and more than 6 million people worldwide(*1*). PD occurs when dopaminergic neurons in the substantia nigra die or lose their function, causing motor symptoms in patients

such as bradykinesia, or slowness, tremor, stiffness, and walking and balance problems(*2*). In patients of older age or with longer duration of PD, cognitive impairment and dementia can also develop (PD with dementia, or PDD)(*3*). Histologically, PD is characterized by the formation of Lewy bodies in neurons of the substantia nigra, composed of the protein α-synuclein (α-syn)(*4*). There is a tight correlation between α-syn aggregation and progression of PD(*5*), so it has been hypothesized that there is a causative link between α-syn aggregation, its toxicity to dopaminergic neurons, and onset of motor symptoms(*6*–*9*). Aggregation of α-syn is a histological hallmark of other, rarer neurodegenerative diseases, including dementia with Lewy bodies (DLB), in which Lewy bodies are found in neurons similarly to PD(*10*), and multiple system atrophy (MSA), in which α-syn aggregates are found in glial cells(*11*). Together, these neurodegenerative diseases are termed synucleinopathies(*6*).

Currently, patients are diagnosed with PD using a combination of medical history and physical exam findings. There are no biomarkers in blood, CSF, or medical imaging that can definitively confirm the diagnosis of PD or measure the progression of disease. Medical nuclear imaging, such as single-photon emission computed tomography (SPECT) and positron emission tomography (PET), can provide additional information for the diagnosis and stage of the disease, as well as biodistribution images of radiotracer targets with high specificity. Clinicians can order a Dopamine Transporter Scan (DaT scan) in which a radio-labeled agent with high affinity for dopamine transporters is administered and detected by single-photon emission computed tomography (SPECT) to measure the loss of dopaminergic neurons. However, the DaT scan is not completely predictive of PD and is best used to validate a clinical diagnosis(*12*). Recently, progress has been made in pre-clinical development of positive emission tomography (PET) tracers that can track α-syn *in vivo*(*13*),(*14*, *15*) and be used as a diagnostic for PD. These nuclear imaging procedures involve ionizing radiation, therefore, the number of times

they can be repeated is limited to minimize the effective dose a patient is exposed to. Radiologists and physicians must consider the risks and benefits of performing repeated ionizing procedures to diagnose, stage, and inform the patient(*16*),(*17*). Alternatively, magnetic resonance imaging (MRI) is non-ionizing, less expensive, and has greater availability than PET (40.4 MRI scanners vs. 5.5 PET scanners per million people in the United States(*18*)). Further, MRI can provide high spatial resolution images that cannot be achieved in nuclear imaging.

MRI can take advantage of its high sensitivity to the paramagnetic effects of iron oxide nanoparticles. Iron oxide MNPs create local magnetic field inhomogeneities, shortening the relaxations times measured by MRI (T2 and T2*), and its presence in tissues results in hypointense regions in the images(*19*, *20*). The relaxation rates R2 (1/T2) and R2* (1/T2*) are directly proportional to iron concentration in tissues and have been used to accurately estimate liver and heart concentrations in healthy and disease states(*21–23*). Recently, there has been demonstrated potential for liganded iron-oxide nanoparticles to function as an MRI contrast agent for brain metastases(*24*) and neurodegenerative disease(*19*, *25*). Iron oxide nanoparticles can cross the blood brain barrier (BBB)(*25*), are non-toxic(*26*) and non-radioactive, and have sufficient magnetic contrast to be visible by MRI. Iron oxide nanoparticles are already FDA approved and used off-label for MRI(*27*, *28*). Functionalizing magnetic nanoparticles to target alpha-synuclein can potentially provide a non-invasive, highly sensitive, repeatable imaging procedure that is readily translatable to the clinic.

In this study, our goal is to develop a safe and effective diagnostic for PD using an MRI-based agent that targets aggregates of α-syn in the brain. Our agent, which we call liganded magnetic nanoparticles (LMNPs), consists of a dextran-coated iron-oxide nanoparticle conjugated to

peptide ligands designed to target α-syn. Our LMNPs bind to aggregates of α-syn *in vitro*, cross the blood-brain barrier in mice with mannitol adjuvant, and can be used as an MRI contrast agent to distinguish mice with α-synucleinopathy from age-matched, wild-type control mice *in vivo*. Because formation of α-syn aggregates often precedes the onset of symptomatic PD(*6*), this biomarker would enable early detection of PD well before clinical symptoms appear. In addition, our MRI contrast agent would be more amenable to longitudinal studies, whereas the amount of exposure to radiation limits the number of PET scans a patient can safely undergo.

## Results

### Rational design of an 11-residue peptide that binds recombinant α-syn

The NACore ($^{68}$GAVVTGVTAVA$^{78}$) is a region of α-syn critical for its aggregation and pathology(*29*). In a previous study, we applied computational and structure-based approaches to identify a 24-residue peptide (24mer) composed of GAVVWGVTAV, designed to bind to the NACore, and GRKKRRQRRRPQ, a cell penetrating peptide(*30*, *31*), conjoined by a two lysine linker. 24mer binds recombinant α-syn fibrils and prevents aggregation of recombinant α-syn *in vitro*(*32*).

In this study, we sought to pursue a similar approach to generate peptides with greater affinity for binding α-syn. First, we modified the top and bottom strands of the NACore ($^{68}$GAVVTGVTAVA$^{78}$) beta-sheet structure at positions 68, 70, 72, and 74, one at a time and then in pairs. These NACore variants were modified in Coot in CCP4(*33*) and then energy minimized in Rosetta(*34*) to find potential capping inhibitors. We also looked for peptides that would block the addition of more beta-strands to the N- and C- termini of the beta-sheet by extending the α-syn sequence N-terminally or C-terminally by two residues. In addition, terminal

arginines were added to aid in the solubility of the peptide. Through an iterative process, we identified a 25-residue peptide composed of the resulting peptide, RVGGARVWGVR, and GRKKRRQRRRPQ, a cell penetrating peptide, conjoined by a two-lysine linker. We called this peptide R8 (**Figure 1A**).

As with 24mer, R8 bound α-syn fibrils. We coated a 96-well plate with α-syn fibrils and monomer and performed an enzyme-linked immunosorbent assay (ELISA) to assess binding of R8 and 24mer at various concentrations. Both R8 and 24mer preferentially bound α-syn fibrils over monomer (**Figure 1B, Supplementary Figure 1A**). When comparing R8 and 24mer binding of α-syn fibrils, R8 bound α-syn fibrils more strongly than 24mer at lower concentrations of 3.55 μM and 0.71 μM, demonstrating that R8 is an improved design for binding α-syn fibrils compared to 24mer (**Supplementary Figure 1B**).

Next, we measured the binding affinity of R8 and 24mer for α-syn fibrils using surface plasmon resonance (SPR) (**Supplementary Fig 2**). For SPR experiments, we immobilized short, sonicated α-syn fibrils on a CM5 SPR chip and measured fibril-binding affinities of R8 and 24mer at concentrations ranging from 0.3 μM to 10 μM. SPR measurements showed an increase in SPR signal (response units) with an increase in inhibitor concentration for both R8 (**Supplementary Figure 2A**) and 24mer (**Supplementary Figure 2B**). The equilibrium dissociation constant ($K_d$) was calculated by steady state analysis. The apparent $K_d$ for R8 and 24mer were determined to be 0.47 μM and 3.7 μM, respectively, demonstrating that R8 was an improved design for binding α-syn fibrils compared to 24mer. These apparent $K_d$s are for a single peptide binding to a fibril.

**Liganded nanoparticles bind recombinant α-syn fibrils, DLB brain-derived fibrils, and MSA brain-derived fibrils *in vitro***

We purchased 10 nm, dextran-coated, amine-functionalized iron oxide magnetic nanoparticles (amine MNPs). We used Sulfo-NHS and EDC crosslinking chemistry to couple R8 with the amine MNPs and create R8-liganded magnetic nanoparticles (R8-LMNPs) (**Figure 2A, Supplementary Figure 3A**). Before and after conjugation, amine-functionalized MNPs (**Supplementary Figure 3B**) and R8-LMNPs (**Supplementary Figure 3C**) were homogenous and well-dispersed. When an equal volume of amine-functionalized MNPs and R8-LMNPs were blotted onto a nitrocellulose membrane, R8-LMNPs spread less far on the nitrocellulose membrane, indicating a change in functionalization of the nanoparticle (**Supplementary Figure 3D**). When the membrane was probed with an antibody for dextran both amine-functionalized MNPs and R8-LMNPs were detected. When the membrane was probed with an antibody for the cell penetrating peptide, only R8-LMNPs were detected, demonstrating successful conjugation of R8 to MNPs (**Supplementary Figure 3D)**. For comparison, 24mer-LMNPs were constructed following the same protocol.

We first assessed binding of R8-LMNPs and 24mer-LMNPs to recombinant α-syn fibrils. We coated a 96-well plate with α-syn fibrils and monomer and performed an ELISA of R8-LMNPs and 24mer-LMNPs at various concentrations. As for both R8 and 24mer alone, both R8-LMNPs and 24mer-LMNPs preferentially bind α-syn fibrils over monomer (**Figure 2B, Supplementary Figure 3E**). R8-LMNPs bound equally well as 24mer-LMNPs at roughly 70% of the concentration of 24mer-LMNPs, demonstrating that R8-LMNPs bind α-syn fibrils more strongly than 24mer-LMNPs (**Figure 2B**). In addition, we attempted to measure the binding affinity of R8-LMNPs and 24mer-LMNPs for α-syn fibrils using SPR. The LMNPs bound so strongly to α-syn fibrils on the SPR chip that they would not dissociate from the chip, so it was not possible to

calculate a $K_d$ for R8-LMNPs or 24mer-LMNPs. Finally, we incubated recombinant α-syn fibrils (50 μM) with R8-LMNPs (10 μg/mL) for 2 hours on ice and visualized them by electron microscopy (**Figure 2C**). The LMNPs, which are electron-dense, appeared as dark circles surrounding the negatively stained α-syn fibrils (as indicated by black arrows).

We next assessed R8-LMNP binding to *ex vivo* brain-derived fibrils. We extracted fibrils from the brains of a patient with dementia with Lewy bodies (DLB) and a patient with multisystem atrophy (MSA) (**Supplementary Table 1**) and confirmed they were α-syn fibrils by immuno-gold labeling with α-syn antibody LB509 (**Supplementary Figure 4A-B**). We incubated DLB brain-derived fibrils or MSA brain-derived fibrils with R8-LMNPs (3 μg/mL) at 4°C overnight and visualized them by electron microscopy. We observed a mixture of 5 nm and 10 nm fibrils among both DLB brain-derived fibrils and MSA brain-derived fibrils, consistent with those observed in previous studies (*35*, *36*). R8-LMNPs bound strongly to 5 nm DLB brain-derived fibrils (**Figure 2D**) and modestly to 10 nm DLB brain-derived fibrils (**Supplementary Figure 4C**). R8-LMNPs bound strongly to both 5 nm and 10 nm MSA brain-derived fibrils **(Figure 2E)**. Unconjugated, amine-functionalized MNPs did not bind MSA brain-derived fibrils (**Supplementary Figure 4D**), demonstrating that α-syn fibril binding by R8-LMNPs is a result of conjugation with the R8 peptide. As a second method to verify R8-LMNP binding, we performed double labeling of DLB brain-derived fibrils or MSA brain-derived fibrils with α-syn antibody LB509 (and secondary antibody conjugated to 6 nm gold) and R8-LMNPs (10 nm iron oxide nanoparticles). We visualized both sizes of nanoparticles binding the DLB brain-derived fibrils (**Supplementary Figure 4E**) and MSA brain-derived fibrils (**Supplementary Figure 4F**).

Next, we assessed the specificity of R8-LMNPs for α-syn fibrils. We extracted fibrils from the brain of an Alzheimer's disease (AD) patient (**Supplementary Table 1**). We performed double labeling of AD brain-derived fibrils with α-syn antibody LB509 (and secondary antibody conjugated to 6 nm gold) and R8-LMNPs (10 nm iron oxide nanoparticles). LB509 did not bind to AD brain-derived fibrils, demonstrating that they were not α-syn fibrils, and R8-LMNPs did not bind fibrils with a paired helical filament morphology, indicating that R8-LMNPs do not bind to tau fibrils (**Figure 2F**). To assess whether R8-LMNPs bind amyloid-β fibrils, we performed immuno-gold labeling of AD brain-derived fibrils with amyloid-β antibody D52D2 (**Supplementary Figure 4G**). We also performed double labeling of AD brain-derived fibrils with amyloid-β antibody D54D2 (and secondary antibody conjugated to 12 nm gold) and R8-LMNPs (10 nm iron oxide nanoparticles). We visualized both sizes of nanoparticles binding some AD brain-derived fibrils, indicating non-specific binding to amyloid-β (**Supplementary Figure 4H**).

**R8-LMNPs cross the blood-brain barrier of M83 mice with mannitol adjuvant**

Once we demonstrated that R8-LMNPs could target α-syn fibrils *in vitro*, we began characterizing R8-LMNP localization in a live mouse model of PD. We chose the M83 model of α-synucleinopathy, which are transgenic mice expressing the human A53T variant α-syn in central nervous system neurons(*37*). By 16 months of age, homozygous M83 mice develop severe motor impairment and widely distributed α-syn inclusions, especially in the spinal cord, brainstem, cerebellum and thalamus. Heterozygous M83 mice develop these symptoms and α-syn inclusions around 22 to 28 months of age(*37*).

To assess the brain penetration of R8-LMNPs in M83 mice, we administered 24 μL of 2% mannitol intranasally to aid with blood-brain barrier penetration(*38*) and immediately

administered R8-LMNPs by tail vein injection (10 mg/kg) to two 20-month-old, male, heterozygous M83 mice. After six hours, we euthanized the mice via transcardiac perfusion and collected their brain tissue. The brain tissues were fixed, embedded, and cut into ultrathin sections with an ultramicrotome. The ultrathin sections were put on copper grids, stained with uranyl acetate and lead citrate, and then observed using transmission electron microscopy. In the brainstem of mice that received R8-LMNPs, electron-dense spots were visible near axons and neuron cell bodies (**Figure 3A-B**, lower magnification images in **Supplementary Figure 5A**). When measured, some electron-dense spots were larger than 10 nm in diameter and others were smaller than 10 nm, with an average diameter between 9.27 nm and 10.99 nm (**Supplementary Fig 5C**).

Mice that did not receive administration of R8-LMNPs were also euthanized and their tissue was used as a control. In control tissue, there were also electron-dense spots visible (**Figure 3C-D**) near axons and neuron cell bodies (**Figure 3C-D**, lower magnification images in **Supplementary Figure 5B**). When measured, all electron-dense spots in control tissue were smaller than 10 nm, with an average diameter between 4.69 and 4.76 nm (**Supplementary Figure 5D**). The average diameter of the electron-dense spots in brains of mice that did not receive R8-LMNPs is significantly lower than the average diameter of electron-dense spots in brains of mice that did receive R8-LMNPs (**Figure 3E**). Because R8-LMNPs were 10 nm in size, we hypothesized that only the electron-dense spots larger than 10 nm in diameter correspond to R8-LMNPs.

In addition, in mice that received R8-LMNPs, electron-dense spots were visible in the cerebellum (**Supplementary Figure 6A-B**, lower magnification images in **Supplementary**

**Figure 7A**) and hippocampus (**Supplementary Figure 6C-D**, lower magnification images in **Supplementary Figure 7B**). When measured, some electron-dense spots were larger than 10 nm in diameter and others were smaller than 10 nm, with an average diameter between 7.70 nm and 9.81 nm in the cerebellum, and 5.99 and 6.44 nm in the hippocampus. The number of electron-dense spots larger than 10 nm in diameter varied between brain regions. There were many electron-dense spots larger than 10 nm in diameter in the brainstem, less in the cerebellum, and only a few, if not zero, in the hippocampus. These findings correlated with the abundance of α-syn pathology in each brain region, with the brainstem and the cerebellum developing α-syn pathology and the hippocampus developing no α-syn pathology.

Finally, as an additional measurement to verify that R8-LMNPs were present in the brain tissue, we performed energy-dispersive X-ray spectroscopy on the stained tissue (**Supplementary Figure 8A**). The most abundant elements detected by percent weight were lead, uranium, carbon, osmium, iron, copper, chloride, arsenic, and oxygen (**Supplementary Figure 8B**). Lead and uranium were present in the lead citrate and uranyl acetate used to negatively stain the tissue. Osmium, chloride, and arsenic were present in the osmium tetroxide and cacodylate buffer used to fix the tissue. Copper was present in the grid the tissue was fixed on, and carbon and oxygen were present in the tissue itself. The high abundance of iron verified that R8-LMNPs were present in the brain tissue.

**R8-LMNPs remain in brains of M83 mice after 48 hours**

Next, we assessed the pharmacokinetic properties of R8-LMNPs in M83 mice using inductively coupled plasma mass spectrometry (ICP-MS). We administered R8-LMNPs by tail vein injection (10 mg/kg) immediately following intranasal administration of mannitol to 12-month-old, male,

heterozygous M83 mice. We euthanized the mice via transcardiac perfusion at 1 hour, 2 hours, 4 hours, 6 hours, 8 hours, 24 hours, and 48 hours of administration (n = 3 mice per time point) and collected their brain tissue. We also euthanized and collected brain tissue from 12-month-old, male, heterozygous M83 mice that did not receive R8-LMNPs to serve as a baseline (0 hour time point, n = 3 mice). We then measured the iron levels in the brain tissue using ICP-MS (**Supplementary Figure 9**). From one to eight hours after administration of R8-LMNPs, iron levels increased in the brains of M83 mice. At 24 hours and 48 hours after administration of R8-LMNPs, iron levels plateaued but were still approximately 50% higher than those at baseline.

**R8-LMNPs can be used as an MRI contrast agent to distinguish M83 mice from age-matched, wild-type control mice**

After determining that R8-LMNPs cross the blood-brain barrier in M83 mice with mannitol adjuvant, we sought to characterize their potential use as an MRI contrast agent to distinguish M83 mice from age-matched, wild-type controls. Iron oxide MNPs create local magnetic field inhomogeneities, causing an increase in R2 and R2* relaxation rates on MRI(*19*, *20*). First, we acquired MR images of various concentrations of R8-LMNPs and amine-functionalized MNPs in water on a 7T MRI (MR Solutions). Within the range of 5 to 25 μg/mL, R8-LMNPs and amine-functionalized MNPs cause a linear increase in R2 (**Supplementary Figure 10A-B**) and R2* (**Figure 4A-B**) relaxation rates.

Next, we examined whether the increase in R2 or R2* relaxation rate in M83 mice after administration of R8-LMNPs would be significantly greater than the increase in R2 or R2* relaxation rate in wild-type controls. We chose to measure differences in R2 or R2* relaxation rates in the brainstem (defined in **Supplementary Figure 10C**), a region with abundant α-syn

aggregates in aged M83 mice(*37*). We administered R8-LMNPs by tail vein injection (10 mg/kg) immediately following intranasal administration of mannitol to one 22-month-old, female, heterozygous M83 mouse and one 22-month-old, female wild-type mouse with the same genetic background (B6C3F1/J). We acquired MR images of their brains at baseline, 8 hours, 24 hours, 36 hours, 48 hours, and 120 hours post-administration. We observed an increase in the average R2 relaxation rate in the brainstem of both the M83 mouse and the wild-type control from 0 to 48 hours (**Supplementary Figure 10D**). By 120 hours, the average R2 relaxation rate in the brainstem of the wild-type control mouse had returned to baseline levels, whereas the average R2 relaxation rate in the brainstem of the M83 mouse was still elevated (**Supplementary Figure 10D**).

To assess whether these differences between M83 mice and wild-type controls would be observed in a larger group, we administered R8-LMNPs by tail vein injection (10 mg/kg) immediately following intranasal administration of mannitol to 22-month-old, female, heterozygous M83 mice (n = 5) and age-matched, female wild-type mice (n = 3). In addition, we administered amine-functionalized MNPs by tail vein injection (10 mg/kg) immediately following intranasal administration of mannitol to 22-month-old, female, heterozygous M83 mice (n = 5). The greatest differences in average R2 relaxation rate between the M83 mouse and the wild-type control mouse in the longitudinal experiment was at 48 and 120 hours post-administration, so we acquired MR images of the larger group at baseline, 48 hours, and 120 hours post-administration.

At 48 hours after administration of R8-LMNPs, we observed that the absolute difference (**Supplementary Figure 11**) and % difference (**Figure 4C-D, Supplementary Figure 12**) in

average R2* relaxation rate in the brainstem of M83 mice was significantly greater than the absolute difference and % difference in average R2* relaxation rate in the brainstem of wild-type control mice. This difference demonstrates that R8-LMNPs can be used as an MRI contrast agent to distinguish M83 mice from age-matched, wild-type controls.

At 48 hours after administration of MNPs, the absolute difference (**Supplementary Figure 11**) and % difference (**Figure 4C-D, Supplementary Figure 13**) in average R2* relaxation rate in the brainstem of M83 mice that received amine-functionalized MNPs was significantly greater than the % difference in average R2* relaxation rate in the brainstem of M83 mice that received R8-LMNPs. This difference indicates that functionalization with the R8 peptide is required to observe MRI contrast in the brainstem.

In addition, we measured differences in R2* relaxation rate in the hippocampus (defined in **Supplementary Figure 10C**), a region that does not develop α-syn aggregates in aged M83 mice(*37*). At 48 hours and 120 hours after administration of R8-LMNPs, we did not observe a significantly different increase in the average R2* relaxation rate in the hippocampus of M83 mice or wild-type control mice (**Supplementary Figure 14**). This finding indicates that the significant decrease in average R2* relaxation rate is limited to regions with abundant α-syn aggregates.

Finally, after MR imaging, we euthanized the mice via transcardiac perfusion and collected and fixed their brain tissue. We performed post-mortem immunohistochemistry on fixed brain tissue sections and observed that there was α-syn pathology in the brainstem, consistent with the increase in average R2* relaxation rate observed by MRI (**Supplementary Figure 15**).

**R8-LMNPs do not distinguish 5xFAD mice or PS19 mice from wild-type control mice**

To investigate whether R8-LMNPs bind to tau or amyloid-β aggregates *in vivo*, we assessed whether R8-LMNPs can distinguish 5xFAD mice and PS19 mice from wild-type control mice. 5xFAD mice develop amyloid-β pathology deep cortex and subiculum as early as two months of age(*39*). PS19 mice develop hyperphosphorylated tau inclusions after six months of age(*40*), and young PS19 mice can be seeded by intracranial injection of tau fibrils to rapidly induce tau pathology(*41*, *42*). We administered R8-LMNPs by tail vein injection (10 mg/kg) immediately following intranasal administration of mannitol to 5.5-month-old, male, heterozygous 5xFAD mice (n = 3) and 5-month-old, male, heterozygous PS19 mice seeded with AD brain-extracted tau fibrils in the left and right hippocampus (n = 4). We acquired MR images at baseline, 48 hours, and 120 hours post-administration.

At 48 hours and 120 hours after administration of R8-LMNPs, we observed that there was an increase in average R2* relaxation rate in the cortex of 5xFAD mice, indicating possible non-specific binding of R8-LMNPs to amyloid-β (**Supplementary Figure 16A-B**). However, the increase in average R2* relaxation rate was not significantly greater than the increase in average R2* relaxation rate in the cortex of wild-type control mice (**Supplementary Figure 16C**). Regardless of possible non-specific binding of R8-LMNPs, there is no increase in R2* in the brainstem of 5xFAD mice, allowing 5xFAD and M83 to be distinguished by the region of brain pathology.

At 48 hours and 120 hours after administration of R8-LMNPs, we observed that there was no significant increase in average R2* relaxation rate in the hippocampus of AD brain-seeded PS19

mice compared to wild-type control mice, indicating no non-specific binding of R8-LMNPs to tau (**Supplementary Figure 17**).

## Discussion

Aggregation of the protein α-synuclein (α-syn) is a histological hallmark of multiple neurodegenerative diseases collectively known as synucleinopathies, including Parkison's disease (PD), PD with dementia (PDD), dementia with Lewy bodies (DLB), and multiple systems atrophy (MSA)(*4*, *10*, *11*). In this study, our goal was to develop a liganded magnetic nanoparticle (LMNP) that could target fibrillar aggregates of α-syn in the brain and be used as an MRI contrast agent for the diagnosis of PD and other synucleinopathies.

First, we identified a 25 residue peptide, which we termed R8, composed of an α-syn targeting peptide and a cell penetrating peptide, conjoined by a two-lysine linker. R8 preferentially binds to α-syn fibrils over monomers (**Figure 1**), and the apparent $K_d$ for R8 binding to α-syn fibrils was measured as 0.47 μM (**Supplementary Figure 2**). We coupled R8 with the amine-functionalized magnetic nanoparticles (MNPs) to create R8-liganded magnetic nanoparticles (R8-LMNPs). R8-LMNPs preferentially bind to α-syn fibrils over monomers and R8-LMNPs bind to recombinant α-syn fibrils, DLB brain-derived fibrils, and MSA brain-derived fibrils (**Figure 2**).

We administered R8-LMNPs by tail vein injection following intranasal administration of mannitol to aged M83 mice, which are known to develop pathology in the spinal cord, brainstem, cerebellum, and thalamus. We observed electron-dense, 10 nm-large R8-LMNPs in the brains of M83 mice (**Figure 3**), and we observed that R8-LMNPs remain in the brains of M83 mice for

at least 48 hours (**Supplementary Figure 9**). Finally, we administered R8-LMNPs by tail vein injection to M83 mice and age-matched, wild-type control mice and observed that the increase in average R2* relaxation rate in the brainstem of M83 mice was significantly greater than the increase in average R2* relaxation rate in the brainstem of wild-type control mice (**Figure 4**). These findings demonstrate that R8-LMNPs can distinguish M83 mice from age-matched, wild-type controls by MRI *in vivo* and could potentially distinguish human patients with α-syn pathology from healthy human controls by MRI.

Recent studies have shown that recombinant α-syn fibrils, α-syn fibrils found in patients with MSA, and α-syn fibrils found in patients with PD/PDD/DLB all have different structural polymorphs(*43–45*). We demonstrated that R8-LMNPs can bind to recombinant α-syn fibrils, DLB brain-derived fibrils, and MSA brain-derived fibrils, so it is unknown whether they distinguish between polymorphs of α-syn fibrils. However, it is possible that R8-LMNPs could distinguish between different synucleinopathies by MRI because of the differing distribution of α-syn aggregates. In PD, Lewy bodies are mostly found in the substantia nigra(*4*), whereas in DLB, Lewy bodies are found in both the neocortex and substantia nigra(*10*). In MSA, glial α-syn aggregates are found in the substantia nigra, the brainstem, and the cerebellum(*11*). These differing distributions, paired with the knowledge that synucleinopathies feature distinct clinical features(*2*, *3*, *46–50*), may still allow for R8-LMNPs to distinguish between synucleinopathies.

There are some limitations to this study. First, R8 binds to α-syn fibrils with an apparent $K_d$ of 0.47 μM, which is weaker than the binding affinity of α-syn PET ligands being investigated(*14*, *15*). However, the nanoparticles have multiple sites for peptide conjugation. Therefore, each R8-LMNP is a multivalent peptide scaffold, increasing the binding affinity through avidity, as

demonstrated by SPR experiments in which LMNPs did not release α-syn fibrils on the SPR chip. In addition, the lower binding affinity of R8 may be compensated by the iron oxide nanoparticles' paramagnetic properties that are detected by MRI with high sensitivity(*24*). If needed, the binding affinity of R8 could be improved with affinity maturation using peptide display methods(*51*). Secondly, we observed non-specific binding of R8-LMNPs to amyloid-β *in vitro*. This result is unsurprising due to the sequence similarity between amyloid-β and the non-amyloid component region of α-syn. However, R8-LMNPs did not distinguish 5xFAD mice from control mice by MRI, so it is unclear whether R8-LMNPs have non-specific binding to amyloid-β *in vivo*. In addition, R2* relaxation rates were increased in the cortex of 5xFAD mice and in the brainstem of M83 mice, allowing them to be distinguished by distribution of pathology. Finally, it has been established that mouse models of α-synucleinopathy and other amyloidopathies do not completely replicate human pathology(*52*). Although our results demonstrated that R8-LMNPs can distinguish M83 mice from age-matched, wild-type controls by MRI, it is possible that they may not target α-syn pathology and be useful as a contrast agent in humans. However, our finding that R8-LMNPs can bind to DLB brain-extracted fibrils and MSA brain-extracted fibrils *in vitro* suggest promise for *in vivo* binding as well.

Before R8-LMNPs could be considered for use in humans, additional studies would need to be done. First, we intranasally administered mannitol to mice to increase BBB permeability because we wanted to first determine whether R8-LMNPs can bind α-syn fibrils *in vivo* before we addressed the question of brain delivery. Now that we have demonstrated that R8-LMNPs can distinguish between M83 and wild-type mice *in vivo*, we plan to study whether mannitol is necessary for effective BBB penetration of R8-LMNPs. Previous studies using similar iron oxide MNPs as MRI contrast agents have shown that MNPs can cross the BBB without the use of mannitol(*25*). However, if further testing reveals that mannitol is necessary for BBB penetration

of R8-LMNPs, R8-LMNPs and mannitol could be co-administered intravenously, similarly to the mannitol in the FDA-approved drug Feraheme, which is delivered by intravenous infusion(*27*). Secondly, our aim was to develop a LMNP that could be used as a contrast agent for early diagnosis of α-synucleinopathies; however, we assessed R8-LMNPs in aged M83 mice with abundant pathology. In future studies, we will assess whether R8-LMNPs increase R2* relaxation rates in younger M83 mice with less pathology to better characterize the sensitivity of R8-LMNPs for early stages of pathology. Finally, additional pharmacokinetic and pharmacodynamic studies will be needed to better characterize the absorption, distribution, metabolism, and excretion (ADME) of R8-LMNPs. We determined that R8-LMNPs remain in the brain of M83 mice for at least 120 hours. However, it remains unclear when they are cleared from the brain, which would affect the frequency of repeat dosing in longitudinal studies. In addition, it remains unclear whether R8-LMNPs are metabolized after administration, which would affect their ability to target α-syn pathology in the brain.

In summary, R8-LMNPs bind to recombinant, DLB brain-derived, and MSA brain-derived fibrils *in vitro*, cross the blood-brain barrier in M83 mice with mannitol adjuvant, and can be used as an MRI contrast agent to distinguish M83 mice from age-matched, wild-type controls *in vivo*. These results provide evidence for the potential of using liganded magnetic nanoparticles that target α-syn for the diagnosis of PD and other synucleinopathies.

## Methods

**Expression and purification of recombinant α-syn.** Recombinant α-syn was expressed and purified as previously described(*32*). The final step in the purification was HPLC Size exclusion chromatography on a preparative G3000 column (Tosoh Bioscience). The resulting α-syn monomer was flash frozen in small aliquots for subsequent experiments.

**Generation of recombinant α-syn fibrils.** Human recombinant α-syn fibrils were grown at 400 μM in PBS at 37˚C, shaking in a Torrey Pines shaker, level 9, over three days. Fibril formation was confirmed by taking a small aliquot, adding thioflavin T, plating in a 96-well plate and verifying fluorescence with the SpectraMax M5 plate reader (excitation wavelength of 444 nm and emission wavelength of 485 nm). Additionally, the presence of fibrils was verified by transmission electron microscopy by diluting the sample to 10 μM and spotting on a glow-discharged carbon-formvar grid, and imaging, as described above.

**Peptide ELISA.** Recombinant α-syn monomer and fibrils were plated at 3.5 μM (100 uL/well) in a high-binding ELISA plate (Greiner, 655061) and placed at 4°C overnight. The next day, wells were blocked with Superblock T20 (Thermo Fisher Scientific), washed with TBS-T (all TBS-T washes were three times for 5 minutes each), and then incubated with R8 and 24mer peptides in PBS (all concentrations in triplicate) for two hours at room temperature. After washing with TBS-T, wells were incubated with primary antibody mouse N3 anti-HIV-1 tat (Abcam) at a 1:300 dilution for one hour. Wells were washed with TBS-T and then incubated with Goat anti-mouse HRP (Sigma) diluted 1:5000 for one hour. After washing with TBS-T, wells were treated with 100 uL room temperature TMB-ELISA and left to develop a blue color. Reactions were quenched with 2 M HCl and absorbance at 450 nm was read on a Spectramax M5 plate reader

(Molecular Devices)Monomer and fibril wells without added peptide were probed with an anti-α-syn antibody (BD Transduction Labs, 610787) as a surrogate loading control.

**Surface plasmon resonance.** SPR experiments were carried out on a BiaCore T200 instrument (GE Healthcare). For preparation of the CM5 conjugated SPR chip (Cytiva), fibrils were centrifuged at 15000 rpm at 4°C for 45 minutes, and the pellet was resuspended in PBS in a volume equivalent to the removed supernatant. The fibrils were sonicated, filtered, and concentrated prior to conjugation to the CM5 chip, as described (ref Sahay and Eisenberg paper) Peptides were diluted in PBS to concentrations ranging from 300 nM to 10 μM. For R8 and 24-mer peptides, all concentrations were recorded in triplicate. R8 data were collected with a 60 second contact time, 24-mer data were collected with both 30 and 60 second contact times. Using the steady state analysis and a 1:1 binding model, the apparent Kd was determined.

**Synthesis of R8-LMNPs.** Amine-functionalized iron oxide nanoparticles, 10 nm in size, were purchased from Creative Diagnostics in New York, USA (WNM-X008). R8 peptide was synthesized by Genscript (Piscataway, NJ) or LifeTein (Somerset, NJ). 0.5 mg of R8 peptide was dissolved in 100 μL ultrapure Millipore water and filtered through a 0.22-micron filter. 2 mg of sulfo-NHS and 0.32 mg of EDC was dissolved in 100 μL activation buffer (0.1 M MES, 0.5 M NaCl, pH 6.0), respectively, before they were mixed. 100 μL sulfo-NHS/EDC mix was added to the 100 μL peptide solution and kept stirred at room temperature for 15 minutes. Next, 200 μl of the R8/EDC/NHS solution was mixed with 100 μl 20X PBS and 100 μl 5 mg/ml MNP and incubated at room temperature for 2 hours. After 2 hours, the solution was kept in a magnetic separator at 4°C overnight. The next day, the supernatant was removed from the nanoparticles,

which were adhered to the wall of the Eppendorf tube in the magnetic separator. The nanoparticles were re-dissolved in 100 µl PBS and the magnetic separation was repeated three times to wash the nanoparticles. Finally, the nanoparticles were re-dissolved in 100 µl PBS and stored at 4°C.

**Dot bot of amine-functionalized MNPs and R8-LMNPs.** 1.5 µL of amine-functionalized MNPs and R8-LMNPs were blotted onto two nitrocellulose membranes. The membranes were blocked in 5% milk in TBST for 45 minutes. One membrane was probed with an antibody for dextran (DX1, STEMCELL Technologies) in 2% milk in TBST (1:500) for 2 hours. The other membrane was probed with an antibody for the Tat peptide (N3, Invitrogen) in 2% milk in TBST (1:500) for 2 hours. The membranes were washed three times with TBST and then probed with an HRP-labeled secondary antibody in 2% milk in TBST (1:5000) for 1 hour. The membranes were washed three times with TBST and then labeled with Thermo Scientific Pierce ECL Western Blotting Substrate. The dot blot was imaged with an Azure Biosystems imaging system.

**Transmission electron microscopy of recombinant fibrils and R8-LMNPs.** Recombinant α-syn fibrils (50 µM) were mixed with R8 peptide-conjugated iron oxide magnetic nanoparticles (10 µg/mL) on ice for 2 hours and then spotted on freshly glow discharged 400 mesh carbon formvar grids (Ted Pella, Inc. 01754-F) at a final concentration of 10 µM α-syn . Grids were washed once in water and then stained for 3 minutes with 2% uranyl acetate, followed by a second water wash, and then allowed to dry. Grids were imaged at 6800x to 49,000x magnification on a FEI Tecnai Electron Microscope operating at 120 kV.

**Extraction of fibrils from DLB brain tissue.** Fresh-frozen brain regions of individuals with DLB were extracted using protocols adapted from Schweighauser et al.(*44*). Briefly, tissues were homogenized in 15 vol (v/w) extraction buffer consisting of 10 mM Tris-HCl, pH 7.5, 0.8 M NaCl, 10% sucrose and 1 mM EGTA. Homogenates were brought to 2% sarkosyl and incubated for 30 min at 37 °C. Following a 10 min centrifugation at 10,000g, the supernatants were spun at 100,000g for 22 min. The pellets were resuspended in 1 ml/g extraction buffer and centrifuged at 3,000g for 5 min. The supernatants were diluted threefold in 50 mM Tris-HCl, pH 7.5, containing 0.15 M NaCl, 10% sucrose and 0.2% sarkosyl, and spun at 166,000g for 32 min. Sarkosyl-insoluble pellets were resuspended in 250 µl/g of 30 mM Tris-HCl, pH 7.4.

**Extraction of fibrils from MSA brain tissue.** Extraction of sarkosyl-insoluble α-syn fibrils from neuropathologically confirmed brain samples of patients diagnosed with MSA was performed using the method previously described by Schweighauser et al. without any modifications(*44*).

**Immunogold labeling of DLB or MSA brain-derived fibrils with α-syn antibody.** Fibrils were spotted on a freshly glow discharged carbon formvar 400 mesh grid (Ted Pella, Inc.), blotted and then blocked in 0.1 % gelatin in PBS for 1 hour at room temp. Grids were then floated on a 50 uL drop of a 1:100 dilution of LB509 (Santa Cruz Biotechnology, sc-58480) in 0.1% gelatin for 1 hour and then washed 5x in 0.1% gelatin in PBS. Grids were floated on drops containing a secondary antibody (goat pAb to Ms IgG (6 nm gold) Abcam ab105285) diluted 1:8 in 0.1% gelatin in PBS for 30 minutes at room temperature, washed 5 x in water, and then stained with 2% uranyl acetate, as previously described(*53*). For DLB fibrils, 0.1% BSA was substituted for 0.1% gelatin.

**Transmission electron microscopy of DLB or MSA brain-derived fibrils and R8-LMNPs.** Human MSA α-syn fibrils were mixed with R8-LMNPs (3 μg/mL) and incubated at 4°C overnight. The next day 3 uL of the sample was spotted on a glow discharged carbon formvar 400 mesh grid and the sample was stained with 2% uranyl acetate, as described above. All grids were imaged at 6,800x to 49,000x magnification on a FEI Tecnai Electron Microscope operating at 120 kV.

**Extraction of fibrils from AD brain tissue.** Extraction of sarkosyl-insoluble fibrils from neuropathologically confirmed brain samples of patients diagnosed with AD was performed using the method previously described by Fitzpatrick et al. without any modifications(*54*). The fibrils were confirmed to be a mixture of tau and amyloid-β by immunogold labeling with amyloid-β antibody, D54D2 (Cell Signaling Technology), and tau antibody, Tau-5 (Invitrogen).

**Immunogold labeling of AD brain-derived fibrils with amyloid-β antibody.** Grids were glow discharged at 15 mA for 30 seconds using the PELCO easiGlow system. 3 uL of AD brain-extracted fibrils were spotted on the grids for 3 minutes. Grids were blotted and blocked in 0.1% BSA in PBS for 10 minutes, transferred to primary antibody (1:50 dilution of D54D2) for 1 hour at room temp or to blocking buffer (no primary antibody control). Grids were washed 5x in blocking buffer, transferred to secondary (1:8 Goat pAb to Rabbit IgG (12 nm gold) (Abcam ab105298) for 30 minutes at room temperature. Grids were washed 5X in water and stained with 2% uranyl acetate.

**Double labeling of DLB, MSA, or AD brain-derived fibrils with α-syn antibody.** Grids were glow discharged at 15 mA for 30 seconds with the PELCO easiGlow system. Brain-extracted

fibrils were incubated with R8-LMNPs (10 μg/mL) for 4 hours and then spotted on a grid for 4 minutes. Grids were then blocked with 0.1% gelatin in PBS for 10 minutes and transferred to a 1:100 dilution of LB509 diluted in 0.1% gelatin for 1 hour. The grids were washed 5x in 0.1% gelatin in PBS and then transferred to the secondary antibody (goat pAb to Ms – 6 nm gold, Abcam ab105285) mixed with R8-LMNPs (15 μg/mL) for 30 minutes at room temperature. Grids were washed 5x with water and stained with 2% uranyl acetate. For DLB and AD fibrils, 0.1% BSA replaced 0.1% gelatin.

**Double labeling of AD brain-derived fibrils with amyloid-β antibody.** Double labeling protocol is the same as for MSA fibrils, except 0.1% BSA in PBS was used in place of 0.1% gelatin in PBS for blocking and primary antibody was 1:50 dilution of D54D2 (Cell Signaling Technology, 8243).

**LMNP ELISA.** LMNP ELISA was carried out in the same manner as the peptide ELISA, except rather than peptide, R8-LMNPs and 24mer-LMNPs were diluted in PBS and the plates were probed with primary antibody mouse anti-dextran antibody (Dx1, Stem Cell Technologies) at a 1:300 dilution. Monomer and fibril wells without LMNPs were probed with an anti-α-syn antibody (BD Transduction Labs 610787) as a surrogate loading control. LMNP concentration was confirmed using inductively coupled plasma mass spectrometry.

**Animal Experiments.** All animal experiments were approved by the UCLA Animal Research Committee and performed under oversight of the Division of Laboratory Animal Medicine (DLAM) under the IACUC protocol number ARC-2018-086. M83 mice (Jackson Laboratories: JAX:000664) were housed on a 12-h light–dark schedule. All live animal scans were approved

and performed at the Functional Biological Imaging Core at the Zilkha Neurogenetic Institute (University of Southern California) under the IACUC protocol number 20658.

Heterozygous male and female M83 mice or wildtype controls were aged to 12-22 months. Mice were injected with R8-LMNPs or amine-MNP (10 mg/kg, i.v.) following intranasal administration of mannitol and then subjected to MR image acquisition (described below). Mice were euthanized (described below) and brain tissue was collected for transmission electron microscopy (described below), inductively coupled plasma mass spectrometry (described below) or immunohistochemical staining (described below).

**Euthanasia of mice.** Mice were sacrificed by overdose with pentobarbital and then transcardial perfusion with perfusion buffer (1x PBS with sodium vanadate, leupeptin, aprotinin, pepstatin, sodium pyrophosphate, sodium fluoride, PMSF). For biochemical studies, the brain was removed and immediately frozen in liquid nitrogen and stored at -80°C until used. For histological studies, the brain was removed and underwent three nights post-fixation in neutral buffered formalin (Thermo Fisher Scientific), transfer to 70% EtOH, and processing and embedding in paraffin. The blocks were then sectioned into 12-μm sections using a microtome (Leica Biosystems).

**Transmission electron microscopy and energy-dispersive X-ray spectroscopy of mouse brain tissue.** Tissue from each region of interest in the mouse brain was dissected, cut into small blocks, immediately fixed in 2.5% glutaraldehyde + 4% paraformaldehyde in 0.1 M sodium cacodylate buffer (pH 7.4), and further fixed with 1% osmium tetroxide in 0.1 M cacodylate buffered solution for 1 hour. The specimens were then dehydrated in 30-100% ethanol. The tissue specimens were embedded in Epon-Araldite and polymerized at 60 °C for 48 h. The

samples were cut into ultrathin sections with an ultramicrotome. The ultrathin sections were put on copper grids (200 mesh) and stained with uranyl acetate and lead citrate and then subjected to TEM observation using a JEOL 100CX transmission electron microscope with an AMT Camera System. Nanoparticle diameter was quantified using ImageJ. Energy-dispersive X-ray spectroscopy were carried out with a Titan 80–300 ST electron microscope (FEI Company) equipped with an extra-brightness field emission gun, an x-ray energy-dispersive detector (EDS), an electron energy filter and a charge-coupled device (CCD) camera.

**Inductively coupled plasma mass spectrometry of mouse brain tissue.** The left hemisphere of each mouse brain was dried at 105 °C to constant weight; 1 mL of concentrated nitric acid and 0.2 mL of concentrated hydrochloric acid were added to the weighted sample (100 mg) in a tube and heated at 80 °C for 2 h. After digestion, the solution was diluted to 10 mL with deionized water. The iron contents of brain tissue were assessed by ICP-MS (NexION 2000, PerkinElmer).

**MRI acquisition.** Data were acquired on a MR Solutions MRI 7T system equipped with a 24 cm bore diameter and 600 mT/m maximum gradient strength, and a 20 mm internal diameter quadrature birdcage mouse head coil. After mice were anesthetized by 1–1.5% isoflurane in room air in an induction chamber (SomnoSuiteTM), they were positioned on the scanner bed, maintained at a temperature of 36-37°C, and secured to prevent motion with ear bars and a bite bar. Ophthalmic ointment was applied over the subject's eyes and a pneumatic pillow was placed over the animal's abdomen to monitor respiration during the scans. Mice were maintained on 1.5-2% isoflurane in 95% oxygen from an oxygen concentrator, delivered via a

nose cone. After the scan, animals were placed in a heated recovery chamber until they were ambulatory before returning them to their home cages.

A positioning gradient echo sequence was first acquired to prepare the slice stacks for the 2D multi-gradient echo (MGE) sequence. The MGE parameters were as follows: echo times (TEs) = 4, 8.48, 12.96, 17.44, 21.92, and 26.40 ms; repetition time (TR) =1,200 ms; slice thickness = 0.5 mm; field of view (FOV) = 20 mm x 20 mm; matrix size = 256 x 256; number of slices = 28; and number of averages (NA) = 1.

**MRI image analysis.** *Quantitative parametric mapping*: Prior to parametric fitting, MGE images were preprocessed using Fiji (ImageJ)43 software with bias correction and denoising (2D median filter with radius = 0.5). Bias correction was performed by dividing each frame of the MGE image stack by its estimated bias field, which was generated using FSL FAST (FMRIB's Automated Segmentation Tool)44. Then, T2* maps were generated through a pixel-by-pixel exponential fitting of the signal intensities across the different TE times, using the MATLAB Rocketship v.1.4 module45. All fits with an $r^2$>0.6 were included. Using Fiji software, pixels with fits having $r^2$ values <0.6 were set to not-a-number (NaN) and were not included in the analysis. Additionally, brain regions were extracted by manually delineating brain outlines on each slice and outside brain regions were set to NaN. Regions of interests (ROI), such as the brainstem and the hippocampus, were manually delineated using the polygon tool in Fiji. R2* maps were generated from the T2* maps, using the relationship T2* = 1/R2*. Mean T2* and R2* values for each ROI, for each subject, were obtained. GraphPad Prism was used for planned comparisons between groups.

*Difference maps by group*: MGE data were converted to Nifti format and then averaged over all echoes to obtain a mean T2* image for each mouse. R2* maps were generated from the T2*

maps, using the relationship T2* = 1/R2*. Data were brain extracted using RATS(*55*) and then entered into the ANTS pipeline for creation of an unbiased, mean deformation template using rigid, affine and non-linear registration(*56*). The resultant transformations were applied to the raw, multi-echo data after which data were fit for R2* with a loglinear fit using Tedana(*57*) (https://zenodo.org/records/7926293). Percentage change in R2* voxel-based maps were computed for each mouse at 48 and 120h using the corresponding pre-injection data by: (post-injection-pre-injection)/pre-injection x 100.

**Immunohistochemistry of mouse brain tissue.** Immunohistochemistry was performed on 10-µm-thick coronal sections Briefly, selected sections were deparaffinized, rehydrated, and steamed with a citric acid-based unmasking solution (Vector Laboratories, Burlingame, CA) for 40 minutes to enhance antigen detection. Endogenous peroxidases were quenched with 0.6% hydrogen peroxide in methanol for 30 min and sections were permeabilized with 0.3% Triton/TBS for 10 min. Sections were blocked in 3% bovine serum albumin (BSA)-TBS with 5% normal goat serum for 45 min at 37°C. Rabbit polyclonal antibody against α-syn phosphorylated at S129 (pS129, EMD Millipore, Burlington, MA)) or monoclonal antibody against misfolded α-syn (5G4, EMD Millipore) was incubated at 37°C for 1 hour, and then overnight at 4°C. After washing, sections were incubated with a biotinylated secondary antibody for 1 hour at 37°C and followed by avidin-biotin-peroxidase complex (ABC-HRP; Vector Laboratories, Burlingame, CA) for 1 hour at 37°C. Bound antibody complexes were visualized using a 3,3'-diaminobenzidine (DAB) Substrate Kit (Vector Laboratories, Burlingame, CA). All antibodies were diluted in 1X Tris-Buffered Saline with 0.1% Tween 20 (TBST). All slides contained a control section with substitution of TBST for the primary antibodies.

**Acknowledgements**

We thank the donors and their families without whom this work would not have been possible. Research reported in this publication was supported by Michael J. Fox Foundation grants MJFF-005905 “Functionalized magnetic nanoparticles (fMNP) for magnetic resonance imaging”, MJFF-023852 “Completion of Pre-clinical Study of a Safe and Effective Image-based Biomarker for Parkinson's Disease”, and MJFF-001065 “Liganded nanoparticles to inhibit Synuclein aggregate deficits in endosomal lysosomal and autophagy pathways”. Research was also supported by the National Center for Advancing Translational Science (NCATS) of the National Institutes of Health under the UCLA Clinical and Translational Science Institute grant number UL1TR001881 (M.B. and D.S.E.). H.P. is supported by the UCLA-Caltech Medical Scientist Training Program (GM08042), the UCLA Chemistry-Biology Interface Training Grant (5T32GM008496), and the Ruth L. Kirschstein National Research Service Award (1F30AG077832-01A1). We thank Dr. Einav Tayeb-Fligelman for discussions and advice on amyloid-β. We thank Marc Diamond from UT Southwestern for the generous gift of biosensor cells. We thank the UCLA and Harvard Brain Tissue Resource Centers for providing human post-mortem brain tissue. We thank the Electron Microscopy Core Facility at the UCLA Brain Research Institute for providing control mouse brain tissue for transmission electron microscopy. We thank Chong Hyun Chang from the Nano and Pico Characterization Laboratory at the UCLA California NanoSystems Institute for assistance in performing ICP-MS. We thank Berislav Zlokovic for the generous gift of 5xFAD mice. We thank the UCLA Translational Pathology Core Laboratory for assistance in paraffin embedding mouse brain tissue.

**Author contributions**

H.P., M.B., and D.S.E. designed research; H.P., M.B., K.H., N.S.S., S.S., P.D., S.L., M.J., X.Z., C.Z., H.S.K., M.M., J.L., C.H., X.C., R.A., M.R.S., and S.A.F. performed research; C.K.W. and H.V.V .contributed new reagents/analytic tools; H.P., M.B., K.H., N.S.S., S.S., P.D., S.L., C.Z., H.M., R.J., N.G.H., G.M.C., and S.A.F. analyzed data; and H.P., M.B., and D.S.E. wrote the paper with contributions from all other authors.

**Potential conflicts**

DSE is SAB chair and equity holder in ADRx, Inc.

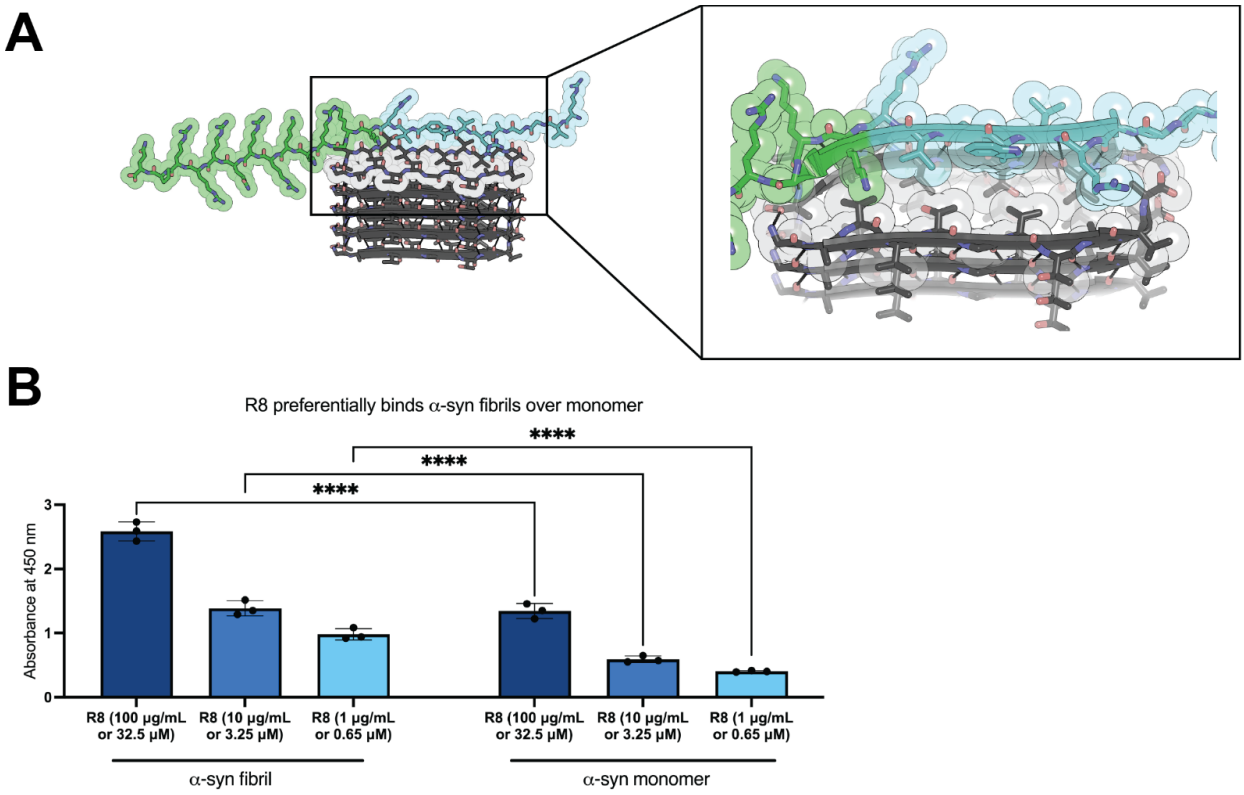


**Figure 1. R8 binds recombinant α-syn and prevents its aggregation. (A)** R8 is a 25-residue peptide containing an α-syn-binding sequence and a cell penetrating sequence conjoined by a two-lysine linker. The designed binding site of R8 on α-syn is the first part of the NACore and two residues preceding it ($^{65}$NVGGAVVTGVTA$^{76}$). **(B)** ELISA assesses binding of R8 to α-syn fibril (left) and monomer (right). R8 preferentially binds α-syn fibril over monomer. Statistical analysis was performed using two-way ANOVA (multiple comparisons using Šídák's multiple comparisons test; ns, $p > 0.05$; *, $p < 0.05$; **, $p < 0.01$; ***, $p < 0.001$; ****, $p < 0.0001$) in GraphPad Prism.

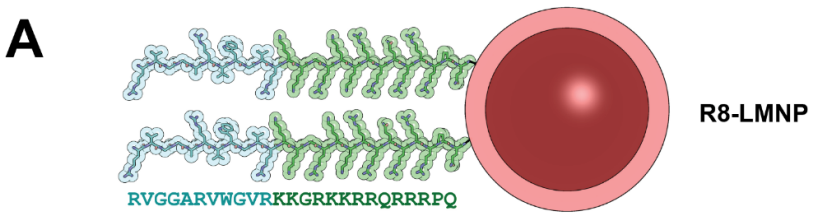
A
R8-LMNP
RVGGARVWGVRKKGRKKRRQRRRPQ

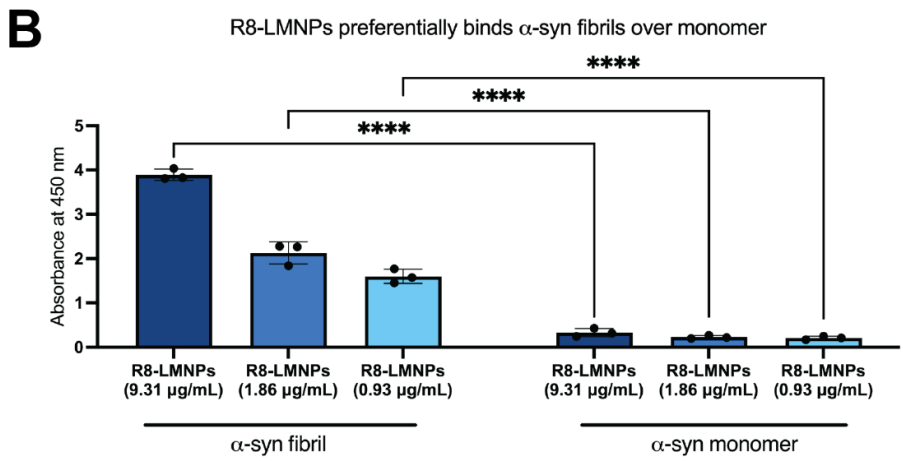
B
R8-LMNPs preferentially binds α-syn fibrils over monomer
****
****
****
Absorbance at 450 nm
0
1
2
3
4
5
R8-LMNPs (9.31 μg/mL)
R8-LMNPs (1.86 μg/mL)
R8-LMNPs (0.93 μg/mL)
R8-LMNPs (9.31 μg/mL)
R8-LMNPs (1.86 μg/mL)
R8-LMNPs (0.93 μg/mL)
α-syn fibril
α-syn monomer

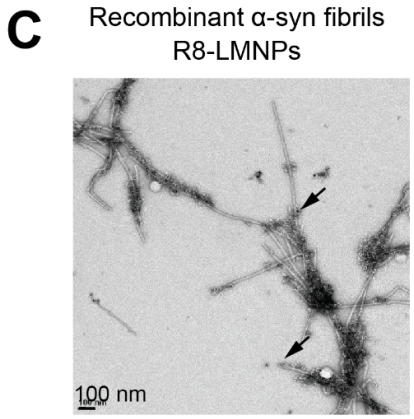
C
Recombinant α-syn fibrils
R8-LMNPs
100 nm

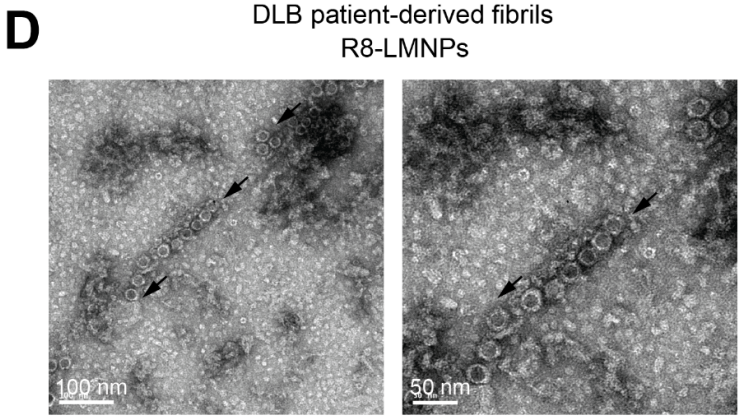
D
DLB patient-derived fibrils
R8-LMNPs
100 nm
50 nm

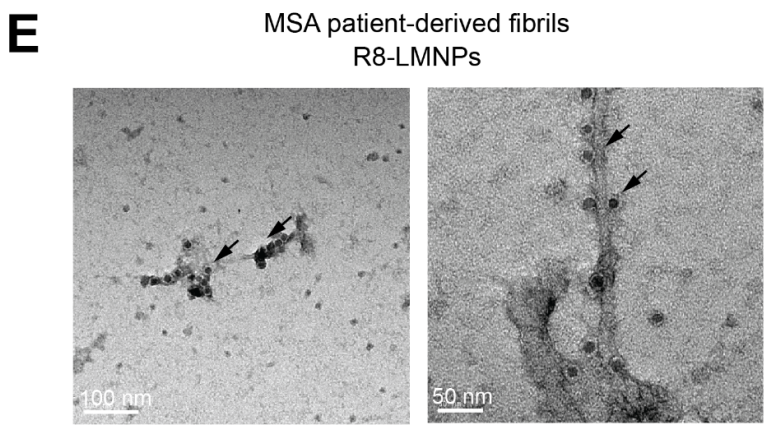
E
MSA patient-derived fibrils
R8-LMNPs
100 nm
50 nm

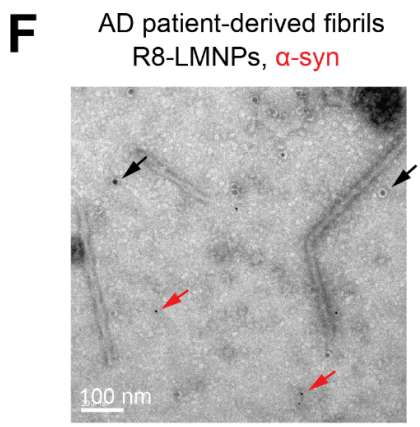
F
AD patient-derived fibrils
R8-LMNPs, α-syn
100 nm

**Figure 2. R8-LMNPs bind recombinant, DLB brain-derived, and MSA brain-derived α-syn fibrils. (A)** R8-liganded magnetic nanoparticles (R8-LMNPs) are composed of a 10 nm diameter iron oxide core (brown) coated with dextran (pink) covalently coupled to the R8 peptide. Multiple ligands on each nanoparticle promote avidity, enhancing binding. **(B)** ELISA assesses binding of R8-LMNPs to α-syn fibril (left) and monomer (right). R8-LMNPs preferentially bind α-syn fibril over monomer. Statistical analysis was performed using two-way ANOVA (multiple comparisons using Šídák's multiple comparisons test; ns, $p > 0.05$; *, $p < 0.05$; **, $p < 0.01$; ***, $p < 0.001$; ****, $p < 0.0001$) in GraphPad Prism. **(C)** Electron micrograph images of R8-LMNPs (black arrows) binding to recombinant α-syn fibrils. **(D)** R8-LMNPs (black arrows) bind to DLB brain-derived fibrils. **(E)** R8-LMNPs (black arrows) bind to MSA brain-derived fibrils. **(F)** Neither R8-LMNPs (10 nm, black arrows) nor α-syn antibody LB509 (and secondary antibody conjugated to 6 nm gold, red arrows) bind to AD brain-derived fibrils.

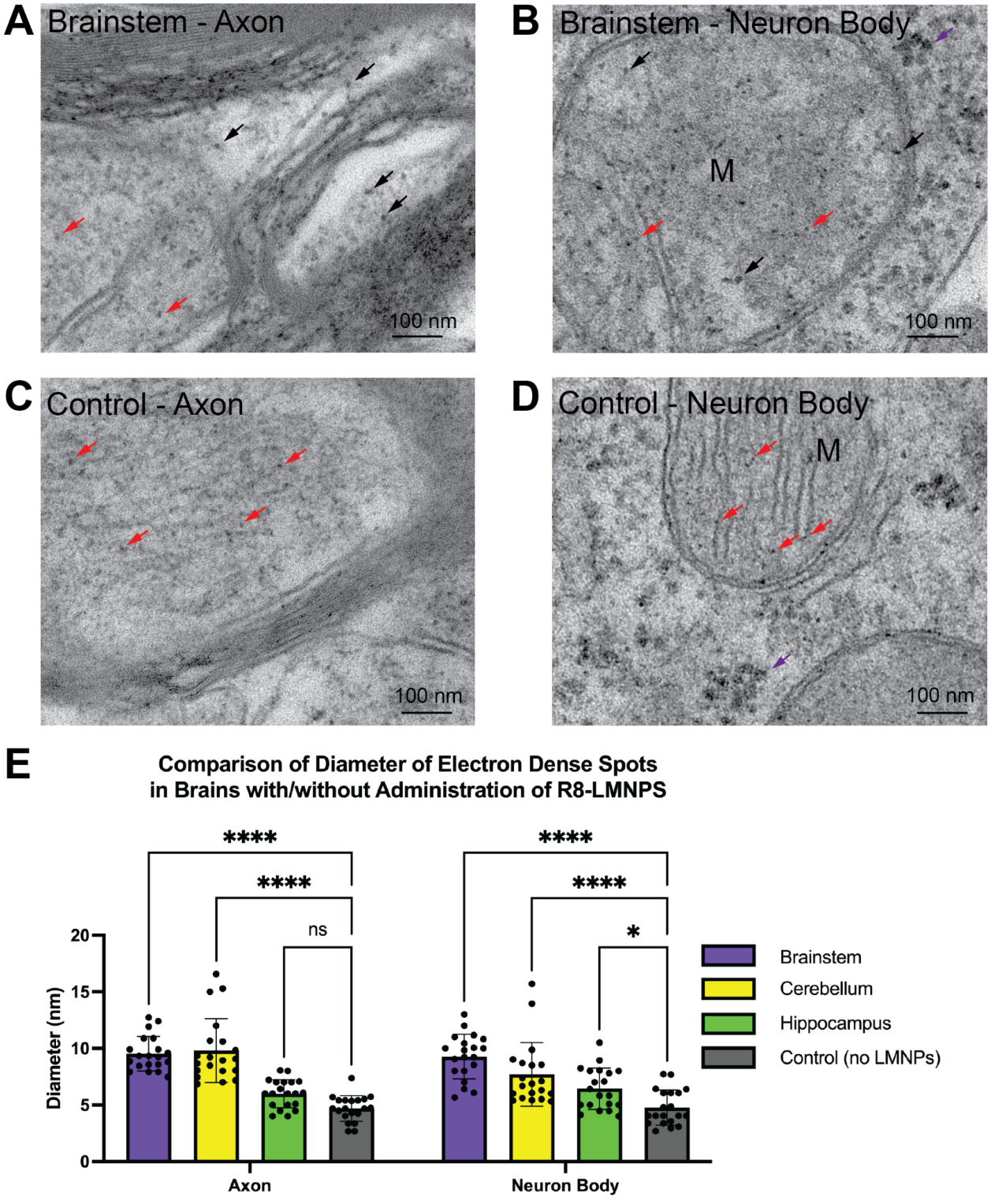


**Figure 3. Large electron-dense spots are visible in the brains of M83 mice treated with R8-LMNPs and not in control mice. (A-B)** R8-LMNPs (10 mg/kg) were administered to aged

M83 mice following intranasal administration of mannitol, and mice were euthanized six hours after administration. Images of ultrathin sections of the brainstem were acquired using electron transmission microscopy. Electron-dense spots larger than 10 nm in diameter (black arrows) and smaller than 10 nm in diameter (red arrows) are visible around (**A**) axons and (**B**) neuron cell bodies. These electron-dense spots can be distinguished from ribosomes (purple arrows) in the cytoplasm of the cell body because ribosomes are clustered and about 30 nm in size. Mitochondria are labeled with M. **(C-D)** Mice that did not receive R8-LMNPs were euthanized and their tissue was used as a control. Electron-dense spots are visible around (**C**) axons and (**D**) neuron cell bodies in control tissue, but they are all smaller than 10 nm in diameter. These electron-dense spots can be distinguished from ribosomes (purple arrows) in the cytoplasm of the cell body because ribosomes are clustered and about 30 nm in size. Mitochondria are labeled with M. (**E**) The average diameter of the electron-dense spots in brains of mice that did not receive R8-LMNPs is significantly lower than the average diameter of electron-dense spots in brains of mice that did receive R8-LMNPs. Statistical analysis was performed using two-way ANOVA (multiple comparisons using Šídák's multiple comparisons test; ns, $p > 0.05$; *, $p < 0.05$; **, $p < 0.01$; ***, $p < 0.001$; ****, $p < 0.0001$) in GraphPad Prism.

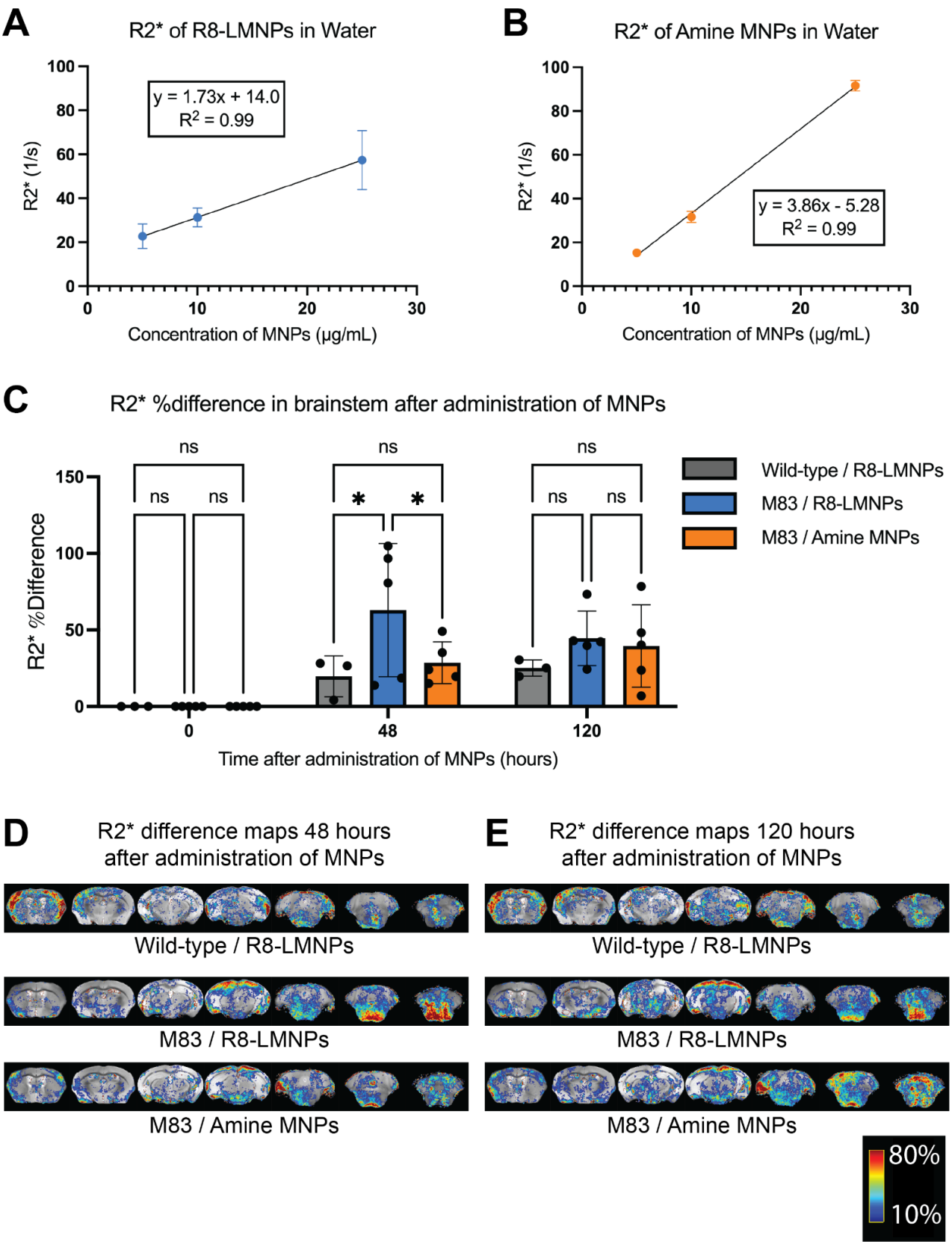
A
R2* of R8-LMNPs in Water
y = 1.73x + 14.0
R2 = 0.99
R2* (1/s)
Concentration of MNPs (µg/mL)
B
R2* of Amine MNPs in Water
y = 3.86x - 5.28
R2 = 0.99
R2* (1/s)
Concentration of MNPs (µg/mL)
C
R2* %difference in brainstem after administration of MNPs
R2* %Difference
ns
*
Wild-type / R8-LMNPs
M83 / R8-LMNPs
M83 / Amine MNPs
Time after administration of MNPs (hours)
D
R2* difference maps 48 hours after administration of MNPs
Wild-type / R8-LMNPs
M83 / R8-LMNPs
M83 / Amine MNPs
E
R2* difference maps 120 hours after administration of MNPs
Wild-type / R8-LMNPs
M83 / R8-LMNPs
M83 / Amine MNPs
80%
10%

**Figure 4. R8-LMNPs can be used as an MRI contrast agent to distinguish M83 mice from age-matched, wild-type controls. (A-B)** R2* relaxation rates of R8-LMNPs **(A)** and amine-functionalized MNPs **(B)** in water. Within the range of 5 to 25 μg/mL, R8-LMNPs and amine-functionalized MNPs cause a linear increase in R2*. **(C)** Average R2* % difference in the brainstem of M83 mice that received R8-LMNPs (n = 5, blue), wild-type control mice that received R8-LMNPs (n = 3, gray), and M83 mice that received amine-functionalized MNPs (n = 5, orange) either 0, 48, or 120 hours after administration of R8-LMNPs or amine MNPs. Statistical analysis was performed using two-way ANOVA (multiple comparisons using Šídák's multiple comparisons test; ns, $p > 0.05$; *, $p < 0.05$; **, $p < 0.01$; ***, $p < 0.001$; ****, $p < 0.0001$) in GraphPad Prism. **(D-E)** Average R2* % difference maps of the brains of M83 mice and age-matched wild-type control mice **(D)** 48 or **(E)** 120 hours after injection of R8-LMNPs or amine-functionalized MNPs. R2* % difference maps display seven anterior to posterior coronal sections of the brain. R2* % difference maps are colorized on a scale from 0 to 100 ms, with cooler colors representing smaller % increase in R2* and warmer colors representing larger % increase in R2*.

**References**


1. GBD 2015 Disease and Injury Incidence and Prevalence Collaborators, Global, regional, and national incidence, prevalence, and years lived with disability for 310 diseases and injuries, 1990-2015: a systematic analysis for the Global Burden of Disease Study 2015. *Lancet Lond. Engl.* **388**, 1545–1602 (2016).
2. J. Jankovic, Parkinson's disease: clinical features and diagnosis. *J. Neurol. Neurosurg. Psychiatry* **79**, 368–376 (2008).
3. S. Garcia-Ptacek, M. G. Kramberger, Parkinson Disease and Dementia. *J. Geriatr. Psychiatry Neurol.* **29**, 261–270 (2016).
4. M. G. Spillantini, M. L. Schmidt, V. M. Lee, J. Q. Trojanowski, R. Jakes, M. Goedert, Alpha-synuclein in Lewy bodies. *Nature* **388**, 839–840 (1997).
5. H. Braak, K. Del Tredici, U. Rüb, R. A. I. de Vos, E. N. H. Jansen Steur, E. Braak, Staging of brain pathology related to sporadic Parkinson's disease. *Neurobiol. Aging* **24**, 197–211 (2003).
6. M. Goedert, M. G. Spillantini, K. Del Tredici, H. Braak, 100 years of Lewy pathology. *Nat. Rev. Neurol.* **9**, 13–24 (2013).
7. A. R. Saha, J. Hill, M. A. Utton, A. A. Asuni, S. Ackerley, A. J. Grierson, C. C. Miller, A. M. Davies, V. L. Buchman, B. H. Anderton, D. P. Hanger, Parkinson's disease alpha-synuclein mutations exhibit defective axonal transport in cultured neurons. *J. Cell Sci.* **117**, 1017–1024 (2004).
8. T. G. Beach, C. H. Adler, L. I. Sue, J. B. Peirce, J. Bachalakuri, J. E. Dalsing-Hernandez, L. F. Lue, J. N. Caviness, D. J. Connor, M. N. Sabbagh, D. G. Walker, Reduced striatal tyrosine hydroxylase in incidental Lewy body disease. *Acta Neuropathol. (Berl.)* **115**, 445–451 (2008).
9. B. N. Dugger, D. W. Dickson, Cell type specific sequestration of choline acetyltransferase

and tyrosine hydroxylase within Lewy bodies. *Acta Neuropathol. (Berl.)* **120**, 633–639 (2010).

10. K. Kosaka, S. Oyanagi, M. Matsushita, A. Hori, Presenile dementia with Alzheimer-, Pick- and Lewy-body changes. *Acta Neuropathol. (Berl.)* **36**, 221–233 (1976).
11. M. I. Papp, J. E. Kahn, P. L. Lantos, Glial cytoplasmic inclusions in the CNS of patients with multiple system atrophy (striatonigral degeneration, olivopontocerebellar atrophy and Shy-Drager syndrome). *J. Neurol. Sci.* **94**, 79–100 (1989).
12. I. Gayed, U. Joseph, M. Fanous, D. Wan, M. Schiess, W. Ondo, K.-S. Won, The impact of DaTscan in the diagnosis of Parkinson disease. *Clin. Nucl. Med.* **40**, 390–393 (2015).
13. S. Roshanbin, M. Xiong, G. Hultqvist, L. Söderberg, O. Zachrisson, S. Meier, S. Ekmark-Lewén, J. Bergström, M. Ingelsson, D. Sehlin, S. Syvänen, In vivo imaging of alpha-synuclein with antibody-based PET. *Neuropharmacology* **208**, 108985 (2022).
14. J. Xiang, Y. Tao, Y. Xia, S. Luo, Q. Zhao, B. Li, X. Zhang, Y. Sun, W. Xia, M. Zhang, S. S. Kang, E.-H. Ahn, X. Liu, F. Xie, Y. Guan, J. J. Yang, L. Bu, S. Wu, X. Wang, X. Cao, C. Liu, Z. Zhang, D. Li, K. Ye, Development of an α-synuclein positron emission tomography tracer for imaging synucleinopathies. *Cell* **186**, 3350-3367.e19 (2023).
15. R. Smith, F. Capotosti, M. Schain, T. Ohlsson, E. Vokali, J. Molette, T. Touilloux, V. Hliva, I. K. Dimitrakopoulos, A. Puschmann, J. Jögi, P. Svenningsson, M. Andréasson, C. Sandiego, D. S. Russell, P. Miranda-Azpiazu, C. Halldin, E. Stomrud, S. Hall, K. Bratteby, E. Tampio L'Estrade, R. Luthi-Carter, A. Pfeifer, M. Kosco-Vilbois, J. Streffer, O. Hansson, The α-synuclein PET tracer [18F] ACI-12589 distinguishes multiple system atrophy from other neurodegenerative diseases. *Nat. Commun.* **14**, 6750 (2023).
16. D. S. W. Djang, M. J. R. Janssen, N. Bohnen, J. Booij, T. A. Henderson, K. Herholz, S. Minoshima, C. C. Rowe, O. Sabri, J. Seibyl, B. N. M. Van Berckel, M. Wanner, SNM practice guideline for dopamine transporter imaging with 123I-ioflupane SPECT 1.0. *J. Nucl. Med. Off. Publ. Soc. Nucl. Med.* **53**, 154–163 (2012).

17. G. Segall, D. Delbeke, M. G. Stabin, E. Even-Sapir, J. Fair, R. Sajdak, G. T. Smith, SNM, SNM practice guideline for sodium 18F-fluoride PET/CT bone scans 1.0. *J. Nucl. Med. Off. Publ. Soc. Nucl. Med.* **51**, 1813–1820 (2010).

18. OECD, “CT scanners, MRI units and PET scanners, 2019 (or nearest year)”, in Health at a Glance 2021: OECD Indicators, (2021); https://doi.org/10.1787/0ad92ec3-en.

19. K. L. Viola, J. Sbarboro, R. Sureka, M. De, M. A. Bicca, J. Wang, S. Vasavada, S. Satpathy, S. Wu, H. Joshi, P. T. Velasco, K. MacRenaris, E. A. Waters, C. Lu, J. Phan, P. Lacor, P. Prasad, V. P. Dravid, W. L. Klein, Towards non-invasive diagnostic imaging of early-stage Alzheimer’s disease. *Nat. Nanotechnol.* **10**, 91–98 (2015).

20. M. W. Winner, T. Sharkey-Toppen, X. Zhang, M. L. Pennell, O. P. Simonetti, J. L. Zweier, P. S. Vaccaro, S. V. Raman, Iron and noncontrast magnetic resonance T2* as a marker of intraplaque iron in human atherosclerosis. *J. Vasc. Surg.* **61**, 1556–1564 (2015).

21. J. C. Wood, C. Enriquez, N. Ghugre, J. M. Tyzka, S. Carson, M. D. Nelson, T. D. Coates, MRI R2 and R2* mapping accurately estimates hepatic iron concentration in transfusion-dependent thalassemia and sickle cell disease patients. *Blood* **106**, 1460–1465 (2005).

22. R. Abou Zahr, B. E. U. Burkhardt, L. Ehsan, A. Potersnak, G. Greil, J. Dillenbeck, Z. Rogers, T. Hussain, Real-World Experience Measurement of Liver Iron Concentration by R2 vs. R2 Star MRI in Hemoglobinopathies. *Diagn. Basel Switz.* **10**, 768 (2020).

23. M. Obrzut, V. Atamaniuk, K. J. Glaser, J. Chen, R. L. Ehman, B. Obrzut, M. Cholewa, K. Gutkowski, Value of liver iron concentration in healthy volunteers assessed by MRI. *Sci. Rep.* **10**, 17887 (2020).

24. S. Serres, M. S. Soto, A. Hamilton, M. A. McAteer, W. S. Carbonell, M. D. Robson, O. Ansorge, A. Khrapitchev, C. Bristow, L. Balathasan, T. Weissensteiner, D. C. Anthony, R. P. Choudhury, R. J. Muschel, N. R. Sibson, Molecular MRI enables early and sensitive detection of brain metastases. *Proc. Natl. Acad. Sci. U. S. A.* **109**, 6674–6679 (2012).

25. X.-G. Liu, S. Lu, D.-Q. Liu, L. Zhang, L.-X. Zhang, X.-L. Yu, R.-T. Liu, ScFv-conjugated

superparamagnetic iron oxide nanoparticles for MRI-based diagnosis in transgenic mouse models of Parkinson's and Huntington's diseases. *Brain Res.* **1707**, 141–153 (2019).

26. N. V. S. Vallabani, S. Singh, Recent advances and future prospects of iron oxide nanoparticles in biomedicine and diagnostics. *3 Biotech* **8**, 279 (2018).
27. M. Lu, M. H. Cohen, D. Rieves, R. Pazdur, FDA report: Ferumoxytol for intravenous iron therapy in adult patients with chronic kidney disease. *Am. J. Hematol.* **85**, 315–319 (2010).
28. A. S. Thakor, J. V. Jokerst, P. Ghanouni, J. L. Campbell, E. Mittra, S. S. Gambhir, Clinically Approved Nanoparticle Imaging Agents. *J. Nucl. Med. Off. Publ. Soc. Nucl. Med.* **57**, 1833–1837 (2016).
29. J. A. Rodriguez, M. I. Ivanova, M. R. Sawaya, D. Cascio, F. E. Reyes, D. Shi, S. Sangwan, E. L. Guenther, L. M. Johnson, M. Zhang, L. Jiang, M. A. Arbing, B. L. Nannenga, J. Hattne, J. Whitelegge, A. S. Brewster, M. Messerschmidt, S. Boutet, N. K. Sauter, T. Gonen, D. S. Eisenberg, Structure of the toxic core of α-synuclein from invisible crystals. *Nature* **525**, 486–490 (2015).
30. M. Green, P. M. Loewenstein, Autonomous functional domains of chemically synthesized human immunodeficiency virus tat trans-activator protein. *Cell* **55**, 1179–1188 (1988).
31. E. Vivès, P. Brodin, B. Lebleu, A truncated HIV-1 Tat protein basic domain rapidly translocates through the plasma membrane and accumulates in the cell nucleus. *J. Biol. Chem.* **272**, 16010–16017 (1997).
32. S. Sangwan, S. Sahay, K. A. Murray, S. Morgan, E. L. Guenther, L. Jiang, C. K. Williams, H. V. Vinters, M. Goedert, D. S. Eisenberg, Inhibition of synucleinopathic seeding by rationally designed inhibitors. *eLife* **9** (2020).
33. P. Emsley, K. Cowtan, Coot: model-building tools for molecular graphics. *Acta Crystallogr. D Biol. Crystallogr.* **60**, 2126–2132 (2004).
34. C. A. Rohl, C. E. M. Strauss, K. M. S. Misura, D. Baker, Protein structure prediction using Rosetta. *Methods Enzymol.* **383**, 66–93 (2004).

35. M. G. Spillantini, R. A. Crowther, R. Jakes, M. Hasegawa, M. Goedert, alpha-Synuclein in filamentous inclusions of Lewy bodies from Parkinson's disease and dementia with lewy bodies. *Proc. Natl. Acad. Sci. U. S. A.* **95**, 6469–6473 (1998).

36. A. Tarutani, M. Hasegawa, Ultrastructures of α-Synuclein Filaments in Synucleinopathy Brains and Experimental Models. *J. Mov. Disord.* **17**, 15–29 (2024).

37. B. I. Giasson, J. E. Duda, S. M. Quinn, B. Zhang, J. Q. Trojanowski, V. M.-Y. Lee, Neuronal alpha-synucleinopathy with severe movement disorder in mice expressing A53T human alpha-synuclein. *Neuron* **34**, 521–533 (2002).

38. R. C. Brown, R. D. Egleton, T. P. Davis, Mannitol opening of the blood-brain barrier: regional variation in the permeability of sucrose, but not 86Rb+ or albumin. *Brain Res.* **1014**, 221–227 (2004).

39. H. Oakley, S. L. Cole, S. Logan, E. Maus, P. Shao, J. Craft, A. Guillozet-Bongaarts, M. Ohno, J. Disterhoft, L. Van Eldik, R. Berry, R. Vassar, Intraneuronal beta-amyloid aggregates, neurodegeneration, and neuron loss in transgenic mice with five familial Alzheimer's disease mutations: potential factors in amyloid plaque formation. *J. Neurosci. Off. J. Soc. Neurosci.* **26**, 10129–10140 (2006).

40. Y. Yoshiyama, M. Higuchi, B. Zhang, S.-M. Huang, N. Iwata, T. C. Saido, J. Maeda, T. Suhara, J. Q. Trojanowski, V. M.-Y. Lee, Synapse loss and microglial activation precede tangles in a P301S tauopathy mouse model. *Neuron* **53**, 337–351 (2007).

41. M. Iba, J. L. Guo, J. D. McBride, B. Zhang, J. Q. Trojanowski, V. M.-Y. Lee, Synthetic tau fibrils mediate transmission of neurofibrillary tangles in a transgenic mouse model of Alzheimer's-like tauopathy. *J. Neurosci. Off. J. Soc. Neurosci.* **33**, 1024–1037 (2013).

42. S. Boluda, M. Iba, B. Zhang, K. M. Raible, V. M.-Y. Lee, J. Q. Trojanowski, Differential induction and spread of tau pathology in young PS19 tau transgenic mice following intracerebral injections of pathological tau from Alzheimer's disease or corticobasal degeneration brains. *Acta Neuropathol. (Berl.)* **129**, 221–237 (2015).

43. C. Peng, R. J. Gathagan, D. J. Covell, C. Medellin, A. Stieber, J. L. Robinson, B. Zhang, R. M. Pitkin, M. F. Olufemi, K. C. Luk, J. Q. Trojanowski, V. M.-Y. Lee, Cellular milieu imparts distinct pathological α-synuclein strains in α-synucleinopathies. *Nature* **557**, 558–563 (2018).

44. M. Schweighauser, Y. Shi, A. Tarutani, F. Kametani, A. G. Murzin, B. Ghetti, T. Matsubara, T. Tomita, T. Ando, K. Hasegawa, S. Murayama, M. Yoshida, M. Hasegawa, S. H. W. Scheres, M. Goedert, Structures of α-synuclein filaments from multiple system atrophy. *Nature* **585**, 464–469 (2020).

45. Y. Yang, Y. Shi, M. Schweighauser, X. Zhang, A. Kotecha, A. G. Murzin, H. J. Garringer, P. W. Cullinane, Y. Saito, T. Foroud, T. T. Warner, K. Hasegawa, R. Vidal, S. Murayama, T. Revesz, B. Ghetti, M. Hasegawa, T. Lashley, S. H. W. Scheres, M. Goedert, Structures of α-synuclein filaments from human brains with Lewy pathology. *Nature* **610**, 791–795 (2022).

46. I. G. McKeith, B. F. Boeve, D. W. Dickson, G. Halliday, J.-P. Taylor, D. Weintraub, D. Aarsland, J. Galvin, J. Attems, C. G. Ballard, A. Bayston, T. G. Beach, F. Blanc, N. Bohnen, L. Bonanni, J. Bras, P. Brundin, D. Burn, A. Chen-Plotkin, J. E. Duda, O. El-Agnaf, H. Feldman, T. J. Ferman, D. Ffytche, H. Fujishiro, D. Galasko, J. G. Goldman, S. N. Gomperts, N. R. Graff-Radford, L. S. Honig, A. Iranzo, K. Kantarci, D. Kaufer, W. Kukull, V. M. Y. Lee, J. B. Leverenz, S. Lewis, C. Lippa, A. Lunde, M. Masellis, E. Masliah, P. McLean, B. Mollenhauer, T. J. Montine, E. Moreno, E. Mori, M. Murray, J. T. O'Brien, S. Orimo, R. B. Postuma, S. Ramaswamy, O. A. Ross, D. P. Salmon, A. Singleton, A. Taylor, A. Thomas, P. Tiraboschi, J. B. Toledo, J. Q. Trojanowski, D. Tsuang, Z. Walker, M. Yamada, K. Kosaka, Diagnosis and management of dementia with Lewy bodies: Fourth consensus report of the DLB Consortium. *Neurology* **89**, 88–100 (2017).

47. D. P. Salmon, D. Galasko, L. A. Hansen, E. Masliah, N. Butters, L. J. Thal, R. Katzman, Neuropsychological deficits associated with diffuse Lewy body disease. *Brain Cogn.* **31**,

148–165 (1996).

48. K. Mondon, A. Gochard, A. Marqué, A. Armand, D. Beauchamp, C. Prunier, D. Jacobi, B. de Toffol, A. Autret, V. Camus, C. Hommet, Visual recognition memory differentiates dementia with Lewy bodies and Parkinson's disease dementia. *J. Neurol. Neurosurg. Psychiatry* **78**, 738–741 (2007).
49. G. K. Wenning, Y. Ben Shlomo, M. Magalhães, S. E. Daniel, N. P. Quinn, Clinical features and natural history of multiple system atrophy. An analysis of 100 cases. *Brain J. Neurol.* **117 ( Pt 4)**, 835–845 (1994).
50. G. K. Wenning, C. Colosimo, F. Geser, W. Poewe, Multiple system atrophy. *Lancet Neurol.* **3**, 93–103 (2004).
51. S. A. Kenrick, P. S. Daugherty, Bacterial display enables efficient and quantitative peptide affinity maturation. *Protein Eng. Des. Sel. PEDS* **23**, 9–17 (2010).
52. M. Schweighauser, A. G. Murzin, J. Macdonald, I. Lavenir, R. A. Crowther, S. H. W. Scheres, M. Goedert, Cryo-EM structures of tau filaments from the brains of mice transgenic for human mutant P301S Tau. *Acta Neuropathol. Commun.* **11**, 160 (2023).
53. K. A. Murray, C. J. Hu, H. Pan, J. Lu, R. Abskharon, J. T. Bowler, G. M. Rosenberg, C. K. Williams, G. Elezi, M. Balbirnie, K. F. Faull, H. V. Vinters, P. M. Seidler, D. S. Eisenberg, Small molecules disaggregate alpha-synuclein and prevent seeding from patient brain-derived fibrils. *Proc. Natl. Acad. Sci. U. S. A.* **120**, e2217835120 (2023).
54. A. W. P. Fitzpatrick, B. Falcon, S. He, A. G. Murzin, G. Murshudov, H. J. Garringer, R. A. Crowther, B. Ghetti, M. Goedert, S. H. W. Scheres, Cryo-EM structures of tau filaments from Alzheimer's disease. *Nature* **547**, 185–190 (2017).
55. I. Oguz, H. Zhang, A. Rumple, M. Sonka, RATS: Rapid Automatic Tissue Segmentation in rodent brain MRI. *J. Neurosci. Methods* **221**, 175–182 (2014).
56. B. B. Avants, N. J. Tustison, M. Stauffer, G. Song, B. Wu, J. C. Gee, The Insight ToolKit image registration framework. *Front. Neuroinformatics* **8**, 44 (2014).

57. P. Kundu, N. D. Brenowitz, V. Voon, Y. Worbe, P. E. Vértes, S. J. Inati, Z. S. Saad, P. A. Bandettini, E. T. Bullmore, Integrated strategy for improving functional connectivity mapping using multiecho fMRI. *Proc. Natl. Acad. Sci. U. S. A.* **110**, 16187–16192 (2013).

| Patient | Braak | Age | Sex | Region |
|---|---|---|---|---|
| DLB | N/A | 90 | F | Frontal |
| MSA | N/A | 65 | F | Cerebellum |
| AD | VI | 86 | F | Left temporal |

**Supplementary Table 1. Pathology information for patient-derived samples.**

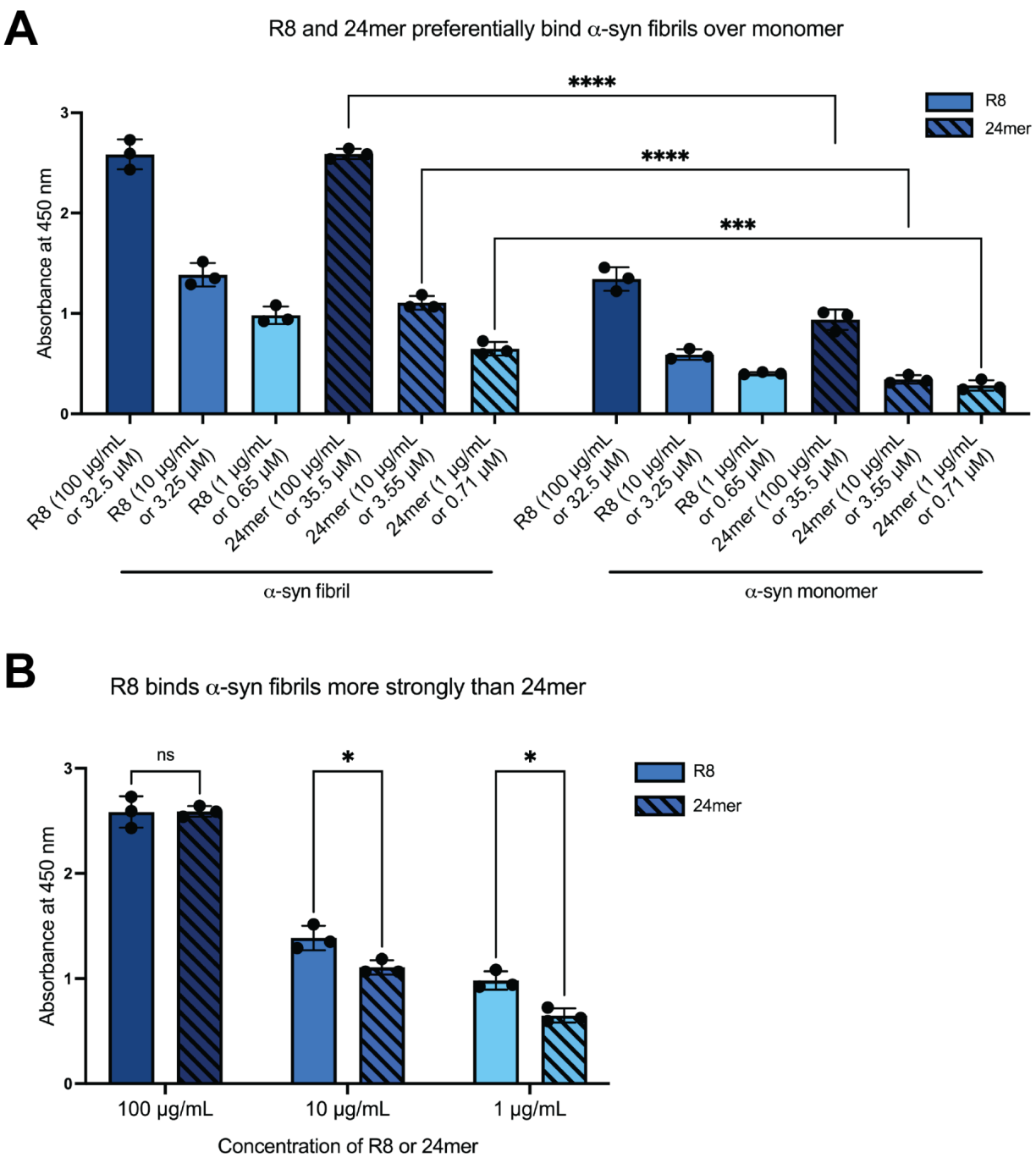


**Supplementary Figure 1. R8 binds recombinant α-syn fibrils. (A)** ELISA assesses binding of R8 and 24mer to α-syn fibril (left) and monomer (right). Both R8 (solid bars) and 24mer (striped bars) preferentially bind α-syn fibril over monomer. Statistical analysis was performed using two-way ANOVA (multiple comparisons using Šídák's multiple comparisons test; ns, $p > 0.05$; *, $p < 0.05$; **, $p < 0.01$; ***, $p < 0.001$; ****, $p < 0.0001$) in GraphPad Prism. **(B)** From the same ELISA

in (A), comparison of R8 and 24mer binding to α-syn fibril. Statistical analysis was performed using multiple unpaired t-tests (multiple comparisons using Holm-Šídák method; ns, $p > 0.05$; *, $p < 0.05$) in GraphPad Prism.

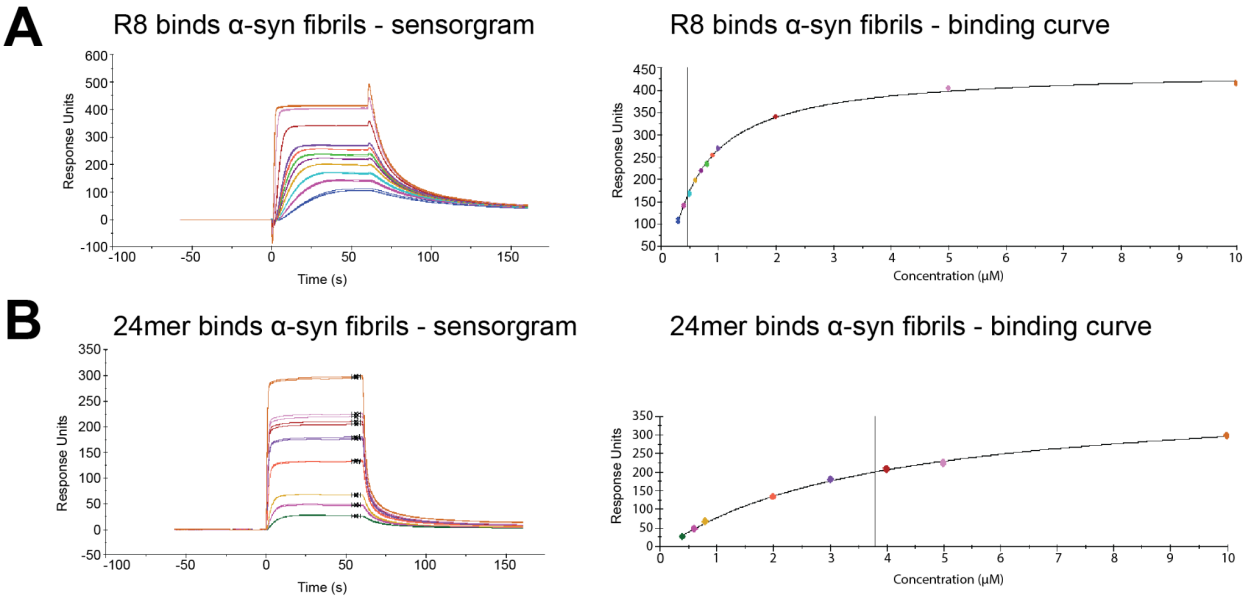


**Supplementary Figure 2. R8 binds recombinant α-syn fibrils.** To assess α-syn fibril binding by surface plasmon resonance (SPR), we immobilized α-syn fibrils on a CM5 SPR chip and measured affinities of **(A)** R8 and **(B)** 24mer. SPR measurements showed an increase in SPR signal (response units) with increase in inhibitor concentration for both peptides (left panels). The equilibrium dissociation constant ($K_d$) was calculated by steady state analysis (right panels). The apparent $K_d$ for R8 was determined to be 0.47 μM, and the apparent $K_d$ for 24mer was determined to be 3.7 μM under identical experimental conditions.

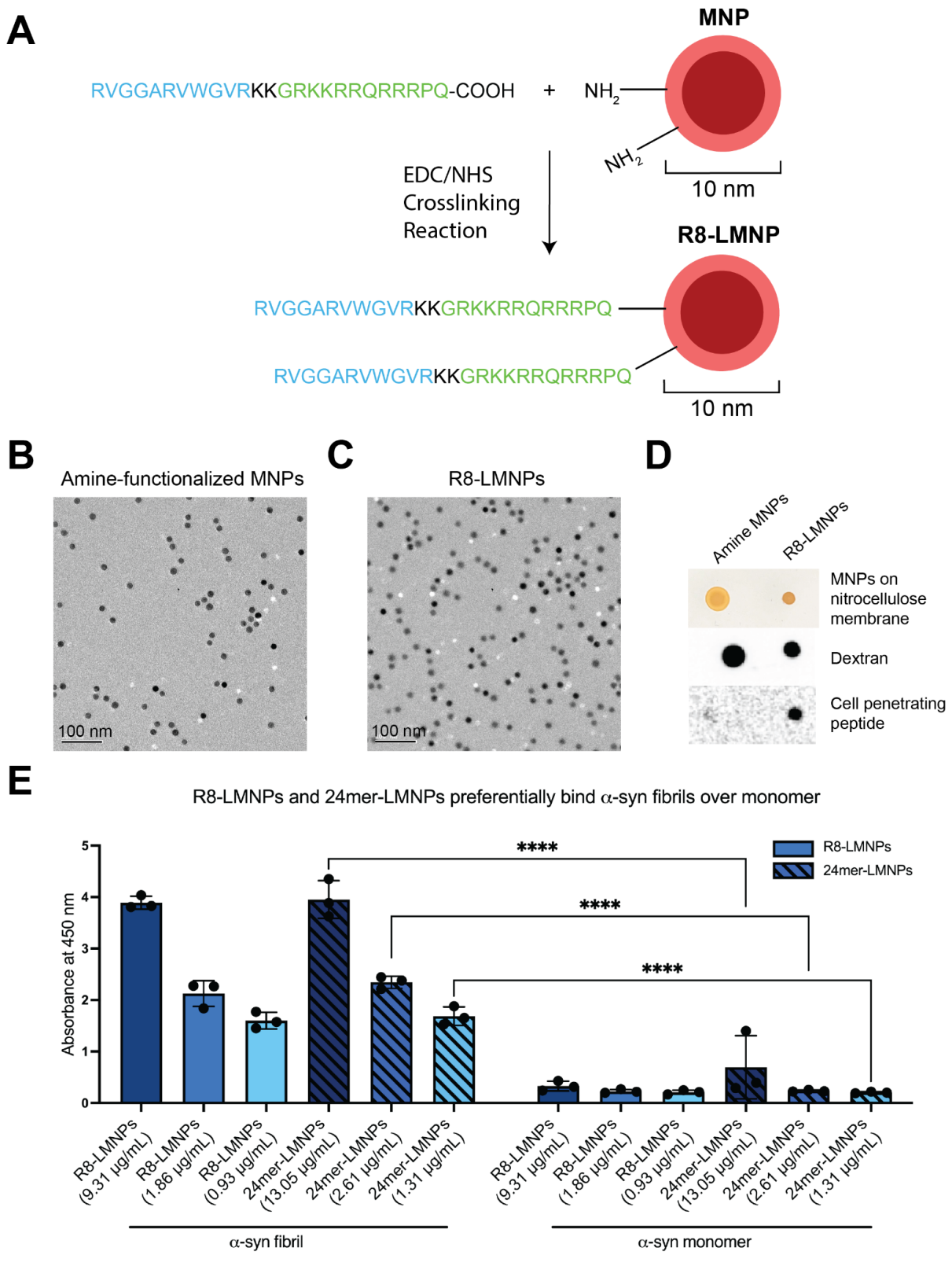


**Supplementary Figure 3. R8-LMNPs bind recombinant α-syn fibrils. (A)** R8-liganded magnetic nanoparticles (R8-LMNPs) are composed of a 10 nm diameter iron oxide core (brown)

coated with dextran (pink), to which we covalently coupled the R8 peptide using EDC/NHS crosslinking chemistry. **(B)** Before conjugation, amine-functionalized nanoparticles are homogenous and well-dispersed. **(C)** After conjugation, R8-LMNPs are still homogenous and well-dispersed. **(D)** 1.5 µL of both amine-functionalized MNPs and R8-LMNPs were blotted onto a nitrocellulose membrane. R8-LMNPs spread less far on the nitrocellulose membrane, indicating a change in functionalization of the nanoparticle. The membrane was probed with an antibody for dextran, which bound both amine-functionalized MNPs and R8-LMNPs, and an antibody for the cell penetrating peptide, which bound only R8-LMNPs. **(E)** ELISA assesses binding of R8-LMNPs and 24mer-LMNPs to α-syn fibril (left) and monomer (right). Both R8-LMNPs (solid bars) and 24mer-LMNPs (striped bars) preferentially bind α-syn fibril over monomer. Statistical analysis was performed using two-way ANOVA (multiple comparisons using Šídák's multiple comparisons test; ns, $p > 0.05$; *, $p < 0.05$; **, $p < 0.01$; ***, $p < 0.001$; ****, $p < 0.0001$) in GraphPad Prism.

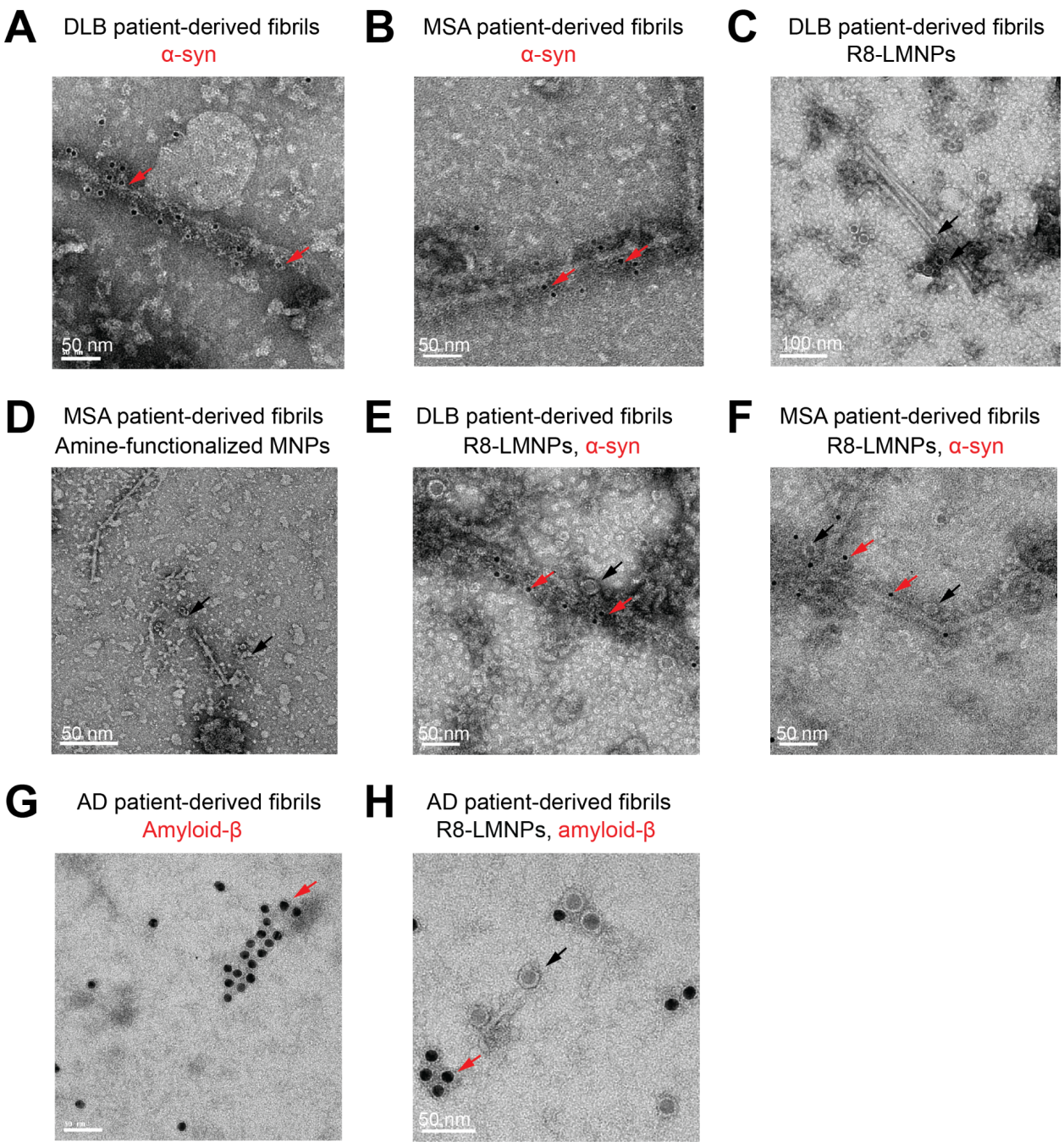


**Supplementary Figure 4. R8-LMNPs bind recombinant, DLB brain-derived, and MSA brain-derived α-syn fibrils. (A-B)** α-syn antibody LB509 (and secondary antibody conjugated to 6 nm gold, red arrows) strongly labeled **(A)** DLB brain-derived fibrils and **(B)** MSA brain-derived fibrils, indicating that they are α-syn fibrils. **(C)** R8-LMNPs labeled 10 nm DLB brain-derived fibrils more modestly labeled than 5 DLB brain-derived nm fibrils shown in Figure 2D.

**(D)** Unconjugated, amine-functionalized nanoparticles (black arrows) did not bind MSA brain-derived fibrils. **(E)** R8-LMNPs (10 nm, black arrows) and α-syn antibody LB509 (6 nm, red arrows) simultaneously bind DLB brain-derived fibrils. **(F)** R8-LMNPs (10 nm, black arrows) and α-syn antibody LB509 (6 nm, red arrows) simultaneously bind MSA brain-derived fibrils. **(G)** Amyloid-β antibody D54D2 (12 nm, red arrows) strongly labeled some AD brain-derived fibrils, indicating those fibrils were composed of amyloid-β. **(H)** R8-LMNPs (10 nm, black arrows) and amyloid-β antibody D54D2 (12 nm, red arrows) simultaneously bind some AD brain-derived fibrils.

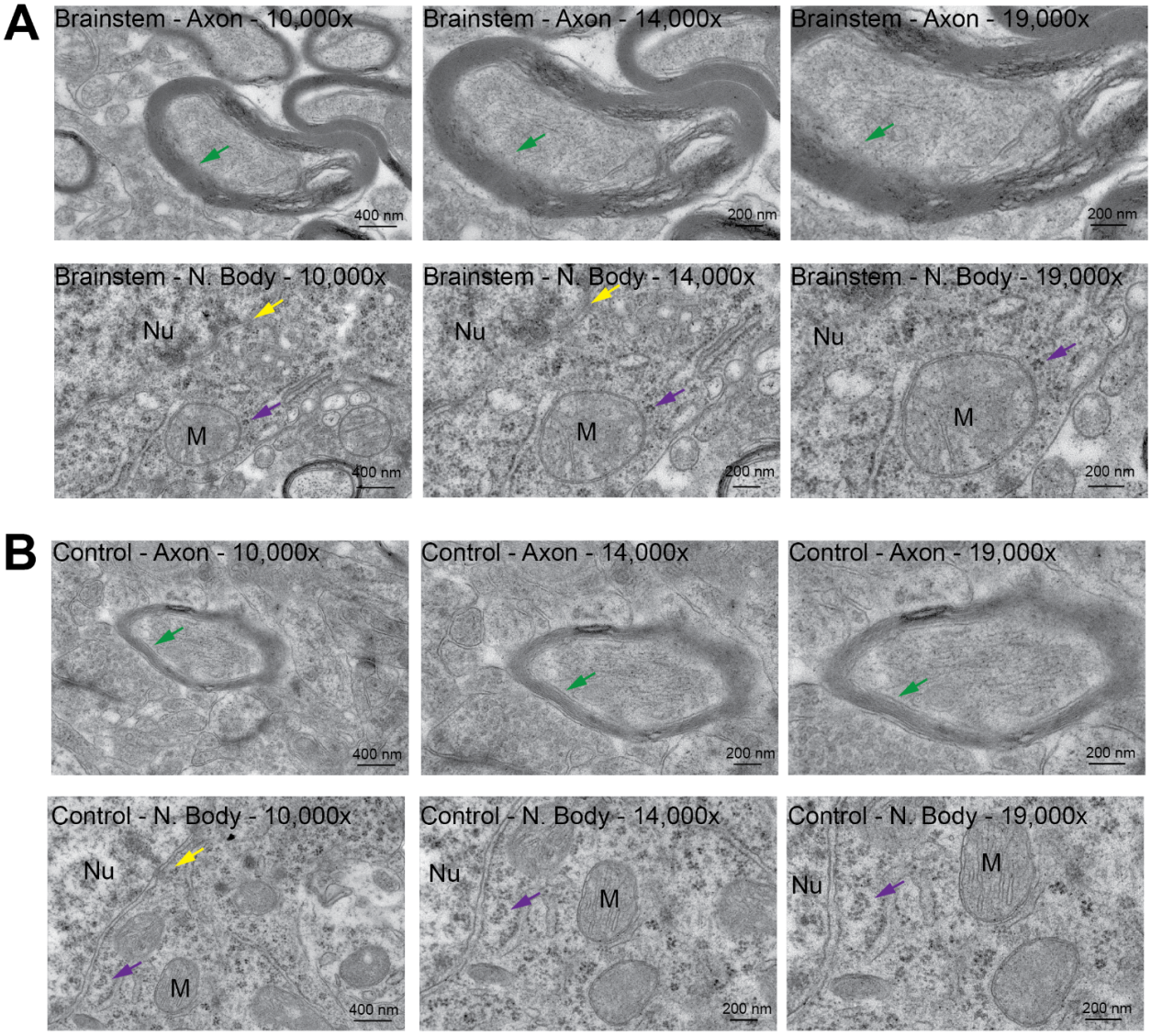
A
Brainstem - Axon - 10,000x
400 nm
Brainstem - Axon - 14,000x
200 nm
Brainstem - Axon - 19,000x
200 nm
Brainstem - N. Body - 10,000x
Nu
M
400 nm
Brainstem - N. Body - 14,000x
Nu
M
200 nm
Brainstem - N. Body - 19,000x
Nu
M
200 nm
B
Control - Axon - 10,000x
400 nm
Control - Axon - 14,000x
200 nm
Control - Axon - 19,000x
200 nm
Control - N. Body - 10,000x
Nu
M
400 nm
Control - N. Body - 14,000x
Nu
M
200 nm
Control - N. Body - 19,000x
Nu
M
200 nm

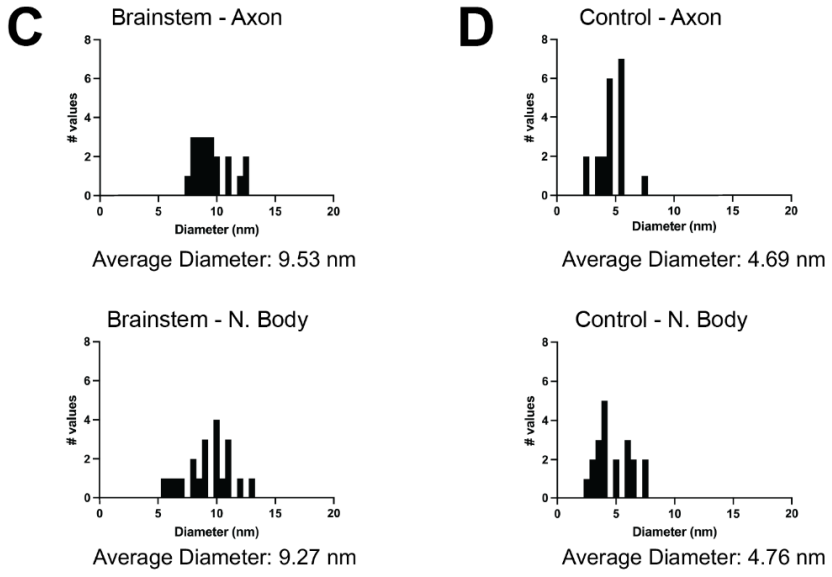
C
Brainstem - Axon
# values
Diameter (nm)
Average Diameter: 9.53 nm
Brainstem - N. Body
# values
Diameter (nm)
Average Diameter: 9.27 nm
D
Control - Axon
# values
Diameter (nm)
Average Diameter: 4.69 nm
Control - N. Body
# values
Diameter (nm)
Average Diameter: 4.76 nm

**Supplementary Figure 5. Large electron-dense spots are visible in the brains of M83 mice treated with R8-LMNPs and not in control mice. (A)** R8-LMNPs (10 mg/kg) were administered to aged M83 mice following intranasal administration of mannitol, and mice were euthanized six hours after administration. **(B)** Mice that did not receive R8-LMNPs were euthanized and their tissue was used as a control. **(A-B)** Images of ultrathin sections of the brainstem were acquired at 10,000x, 14,000x, and 19,000x magnification. Axons are identified by their electron-dense myelin sheath (green arrow). Neuron cell bodies are identified by their large, vacuous nucleus surrounded by a double membrane (yellow arrow) and the presence of abundant ribosomes in their cytoplasm (purple arrow). Mitochondria are labeled with M and nuclei with Nu. **(C-D)** Distribution (n = 20) of the diameter of electron-dense spots in the tissue was measured in (**C**) aged M83 mice that received R8-LMNPs and (**D**) control mice.

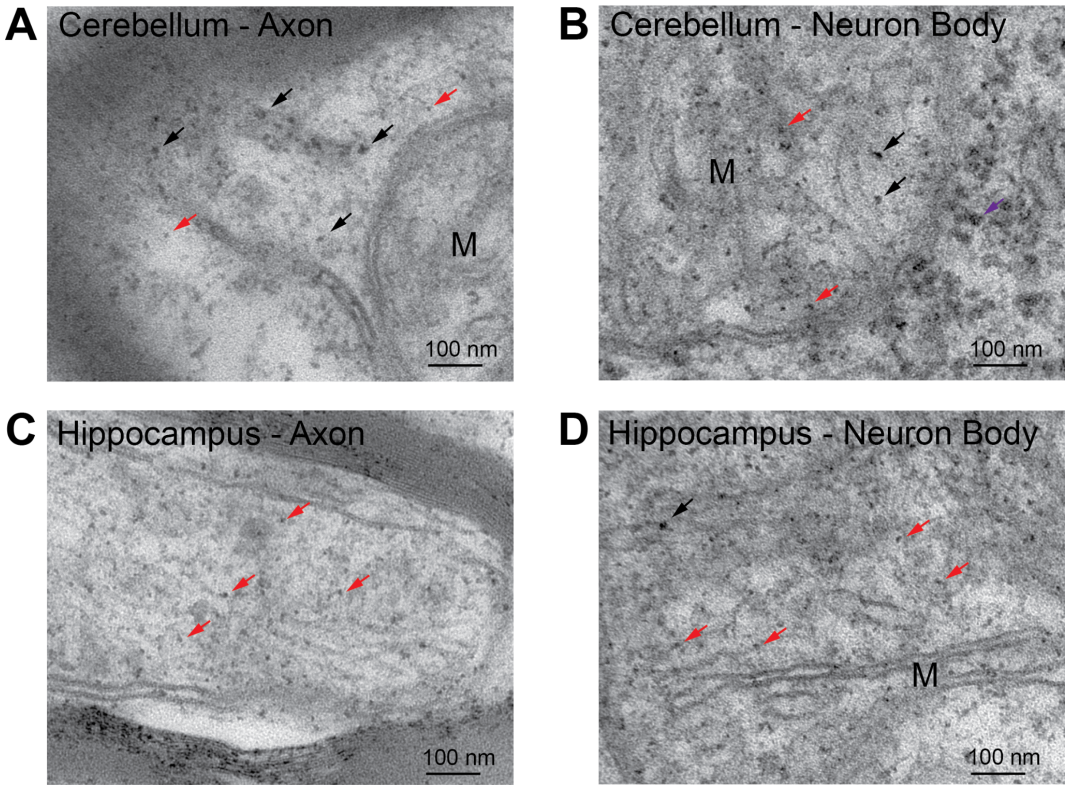


**Supplementary Figure 6. Distribution of the diameter of electron-dense spots varies between brain regions.** R8-LMNPs (10 mg/kg) were administered to aged M83 mice following intranasal administration of mannitol, and mice were euthanized six hours after administration. Images of ultrathin sections of the (**A-B**) cerebellum and (**C-D**) hippocampus were acquired using transmission electron microscopy. Electron-dense spots larger than 10 nm in diameter (black arrows) and smaller than 10 nm in diameter (red arrows) are visible in all three regions around axons (**A, C**) and neuron cell bodies (**B, D**). These electron-dense spots can be distinguished from ribosomes (purple arrows) in the cytoplasm of the cell body because ribosomes are clustered and about 30 nm in size. Mitochondria are labeled with M.

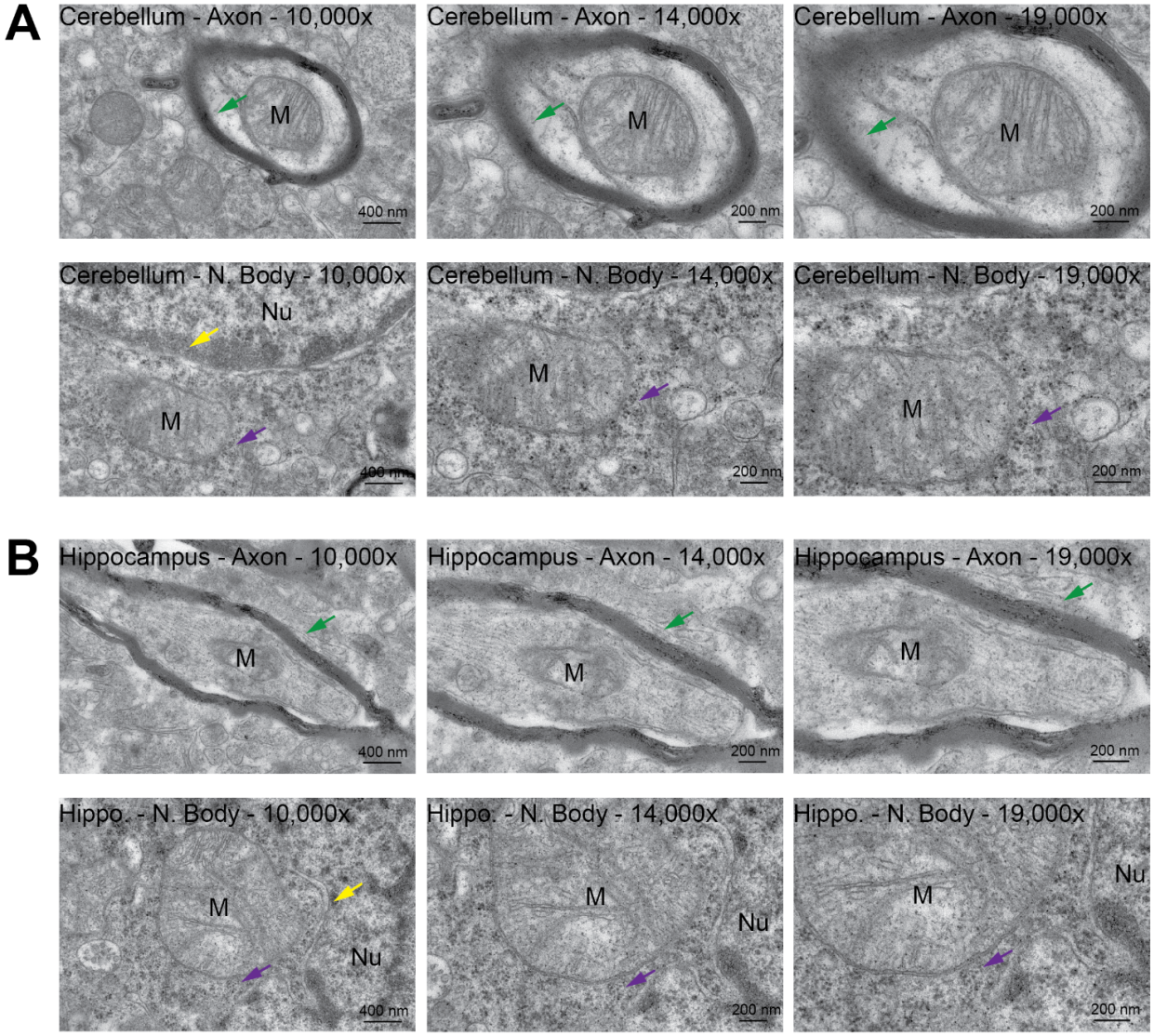
A
Cerebellum - Axon - 10,000x
M
400 nm
Cerebellum - Axon - 14,000x
M
200 nm
Cerebellum - Axon - 19,000x
M
200 nm
Cerebellum - N. Body - 10,000x
Nu
M
400 nm
Cerebellum - N. Body - 14,000x
M
200 nm
Cerebellum - N. Body - 19,000x
M
200 nm
B
Hippocampus - Axon - 10,000x
M
400 nm
Hippocampus - Axon - 14,000x
M
200 nm
Hippocampus - Axon - 19,000x
M
200 nm
Hippo. - N. Body - 10,000x
M
Nu
400 nm
Hippo. - N. Body - 14,000x
M
Nu
200 nm
Hippo. - N. Body - 19,000x
M
Nu
200 nm

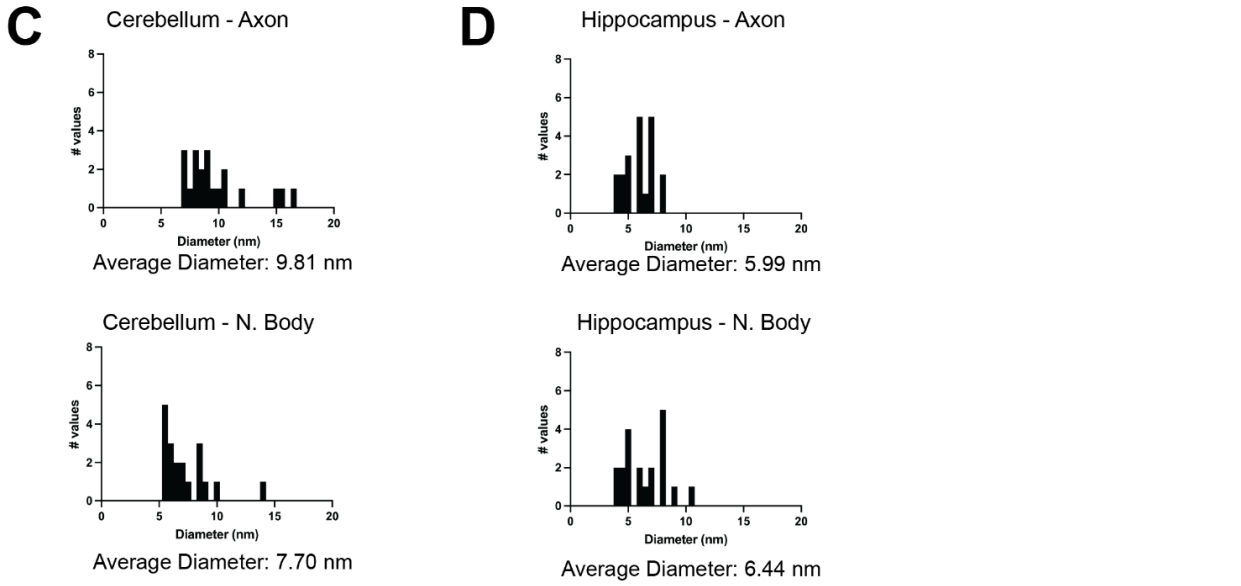
C
Cerebellum - Axon
# values
Diameter (nm)
Average Diameter: 9.81 nm
Cerebellum - N. Body
# values
Diameter (nm)
Average Diameter: 7.70 nm
D
Hippocampus - Axon
# values
Diameter (nm)
Average Diameter: 5.99 nm
Hippocampus - N. Body
# values
Diameter (nm)
Average Diameter: 6.44 nm

**Supplementary Figure 7. Distribution of the diameter of electron-dense spots varies between brain regions.** R8-LMNPs (10 mg/kg) were administered to aged M83 mice following intranasal administration of mannitol, and mice were euthanized six hours after administration. **(A-B)** Images of ultrathin sections of the (**A**) cerebellum and (**B**) hippocampus were acquired at 10,000x, 14,000x, and 19,000x magnification. Axons are identified by their electron-dense myelin sheath (green arrow). Neuron cell bodies are identified by their large, vacuous nucleus surrounded by a double membrane (yellow arrow) and the presence of abundant ribosomes in their cytoplasm (purple arrow). Mitochondria are labeled with M and nuclei with Nu. **(C-D)** Distribution (n = 20) of the diameter of electron-dense spots in the tissue was measured in (**C**) cerebellum and (**D**) hippocampus.

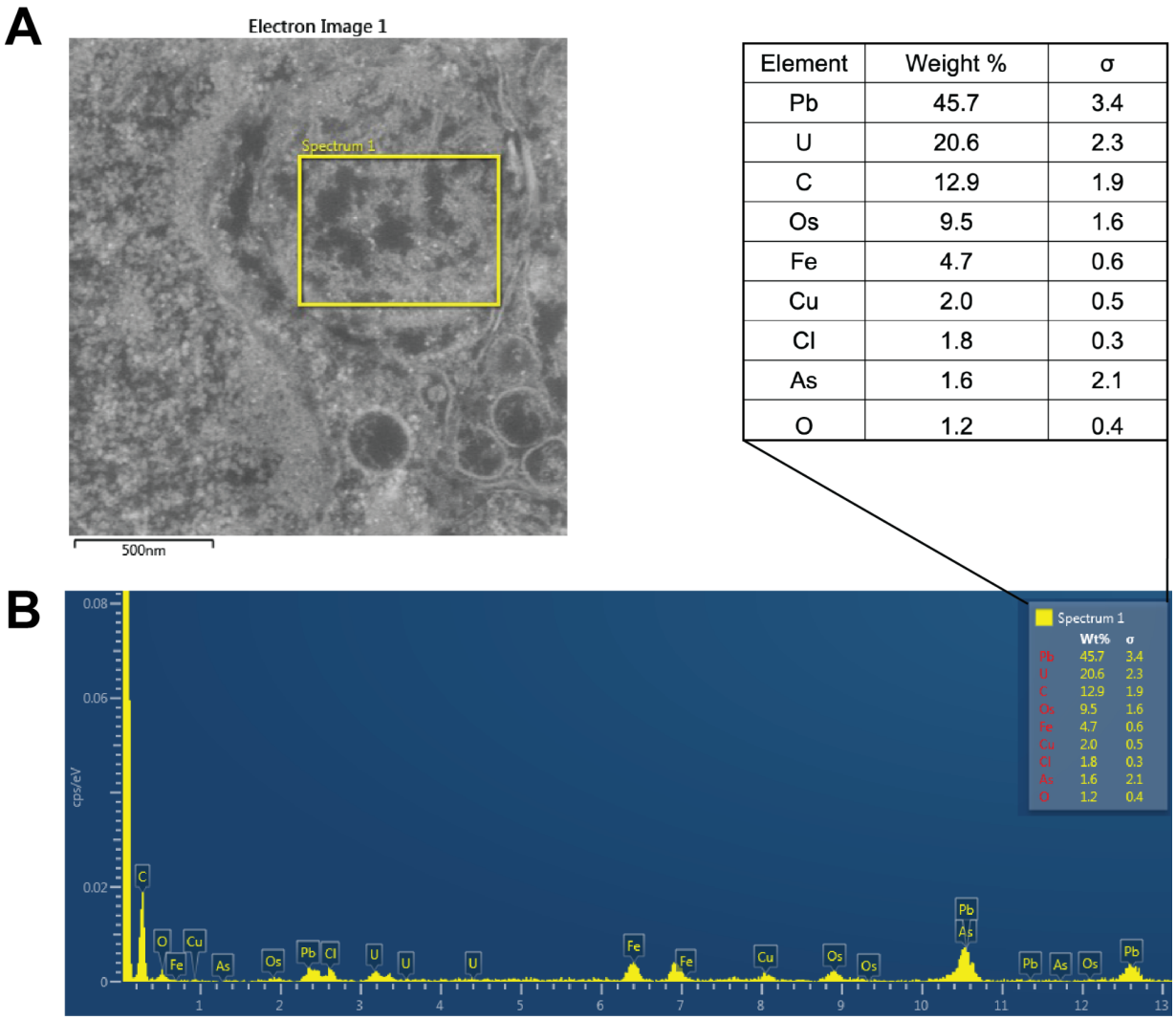


| Element | Weight % | σ |
|---|---|---|
| Pb | 45.7 | 3.4 |
| U | 20.6 | 2.3 |
| C | 12.9 | 1.9 |
| Os | 9.5 | 1.6 |
| Fe | 4.7 | 0.6 |
| Cu | 2.0 | 0.5 |
| Cl | 1.8 | 0.3 |
| As | 1.6 | 2.1 |
| O | 1.2 | 0.4 |

**Supplementary Figure 8. R8-LMNPs cross the blood-brain barrier of M83 mice with mannitol adjuvant.** R8-LMNPs (10 mg/kg) were administered to aged M83 mice, and mice were euthanized 6 hours after administration. **(A)** Region of interest probed by energy dispersive X-ray spectroscopy. **(B)** X-ray spectrum of region of interest shown in (A) and table of detected elements by percent weight. The precision of the percent weight measurement is reported in σ, where 2σ is defined as a precision of ±1%.

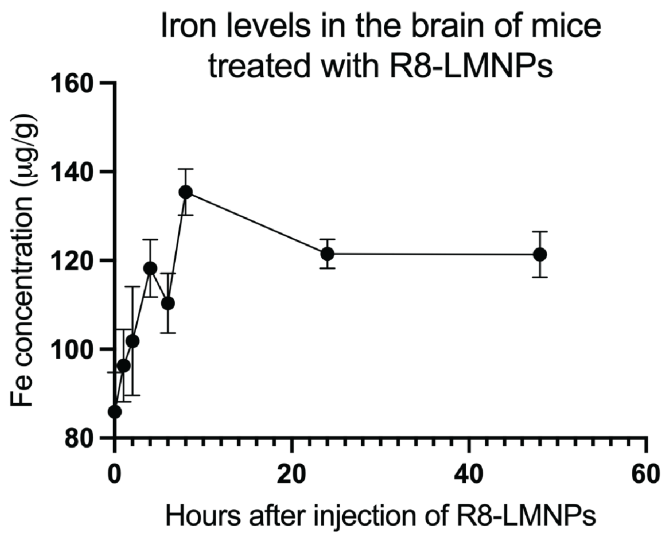


**Supplementary Figure 9. R8-LMNPs remain in brains of M83 mice after 48 hours.** R8-LMNPs (10 mg/kg) were administered to aged M83 mice, and mice were euthanized at various times up to 48 hours after administration (n = 3 mice per time point). From one to eight hours after administration of R8-LMNPs, iron levels increased in the brains of M83 mice. At 24 hours and 48 hours after administration of R8-LMNPs, iron levels plateaued but were still higher than those at baseline.

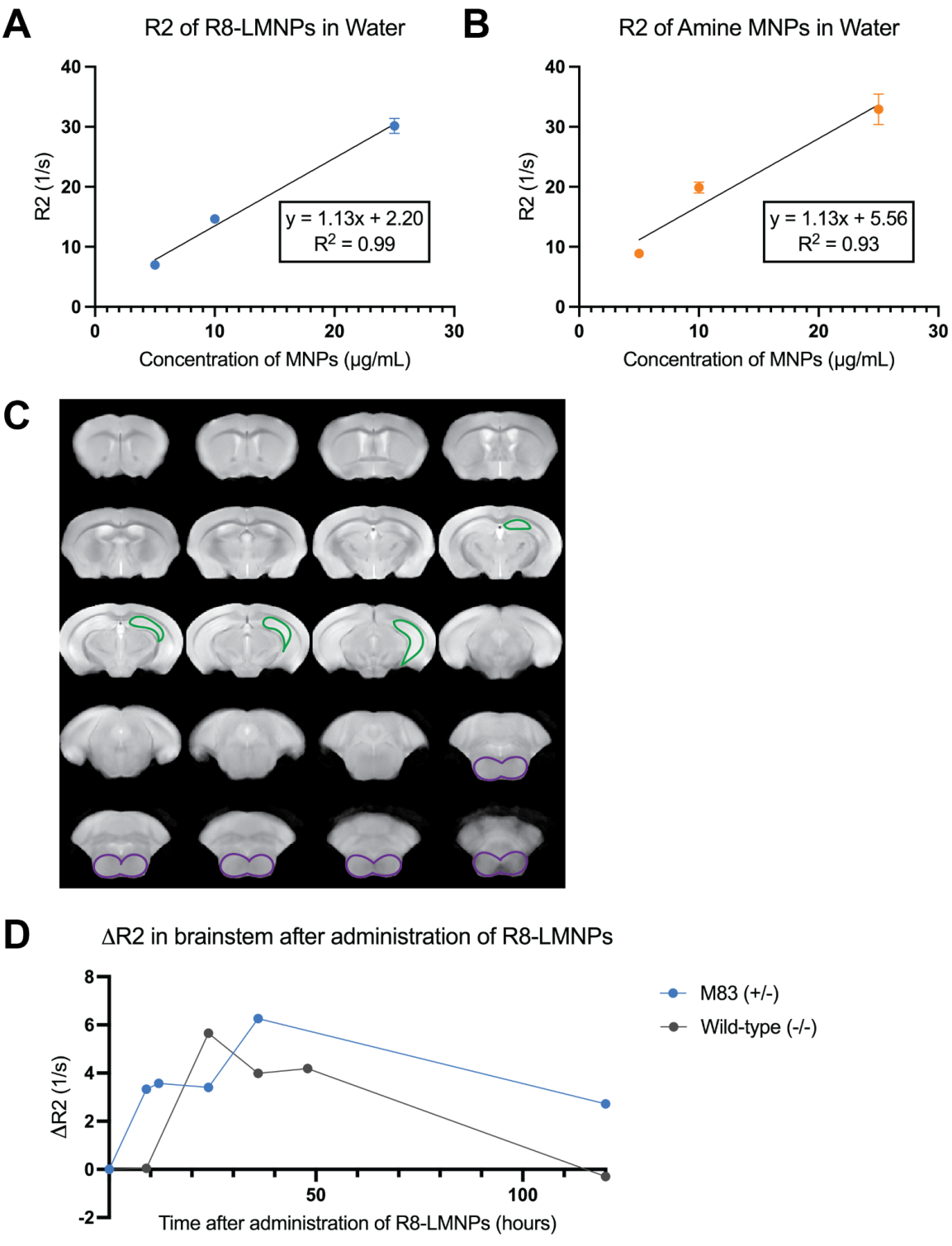


**Supplementary Figure 10. R8-LMNPs can be used as an MRI contrast agent to distinguish M83 mice from age-matched, wild-type controls. (A-B)** R2 relaxation rates of **(A)** R8-LMNPs and **(B)** amine-functionalized MNPs in water. Within the range of 5 to 25 μg/mL, R8-LMNPs and

amine-functionalized MNPs cause a linear increase in R2. **(C)** Grayscale maps display 20 anterior to posterior coronal sections of the brain. The brainstem is highlighted in purple, the hippocampus is highlighted in green. **(D)** Average R2 relaxation rate measured in the brainstem of one aged M83 mouse (blue) and one age-matched wild-type control mouse (gray) that received R8-LMNPs (10 mg/kg) over the course of 120 hours.

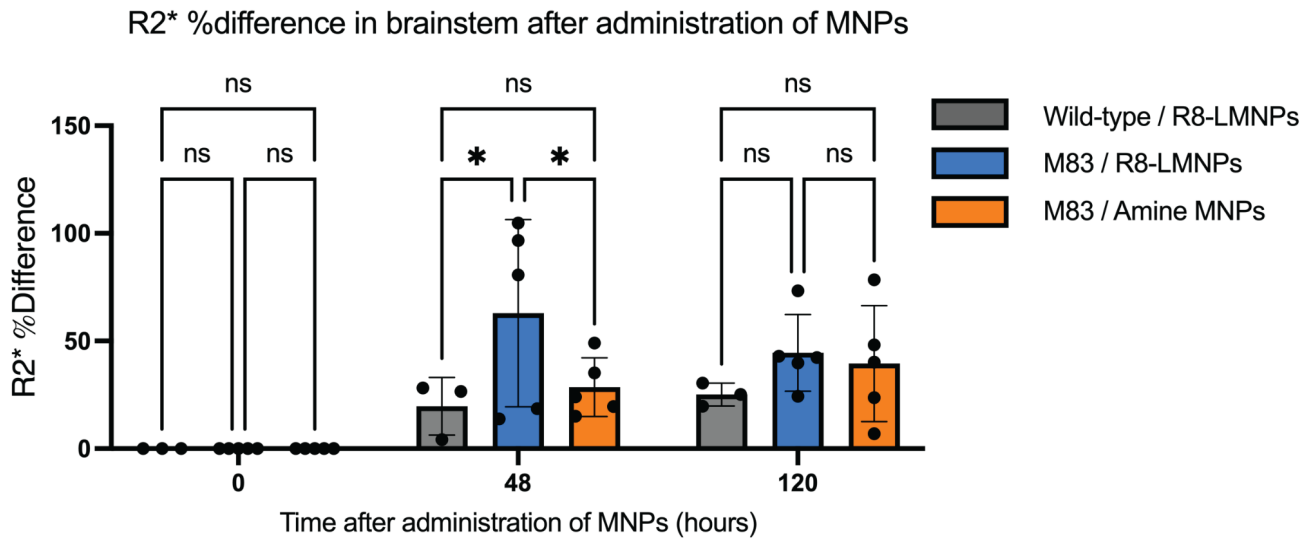


**Supplementary Figure 11. R8-LMNPs can be used as an MRI contrast agent to distinguish M83 mice from age-matched, wild-type controls.** Average change in R2* relaxation rate in the brainstem of M83 mice that received R8-LMNPs (n = 5, blue), wild-type control mice that received R8-LMNPs (n = 3, gray), and M83 mice that received amine-functionalized MNPs (n = 5, orange) either 0, 48, or 120 hours after administration of R8-LMNPs or amine MNPs. Statistical analysis was performed using two-way ANOVA (multiple comparisons using Šídák's multiple comparisons test; ns, $p > 0.05$; *, $p < 0.05$; **, $p < 0.01$; ***, $p < 0.001$; ****, $p < 0.0001$) in GraphPad Prism.

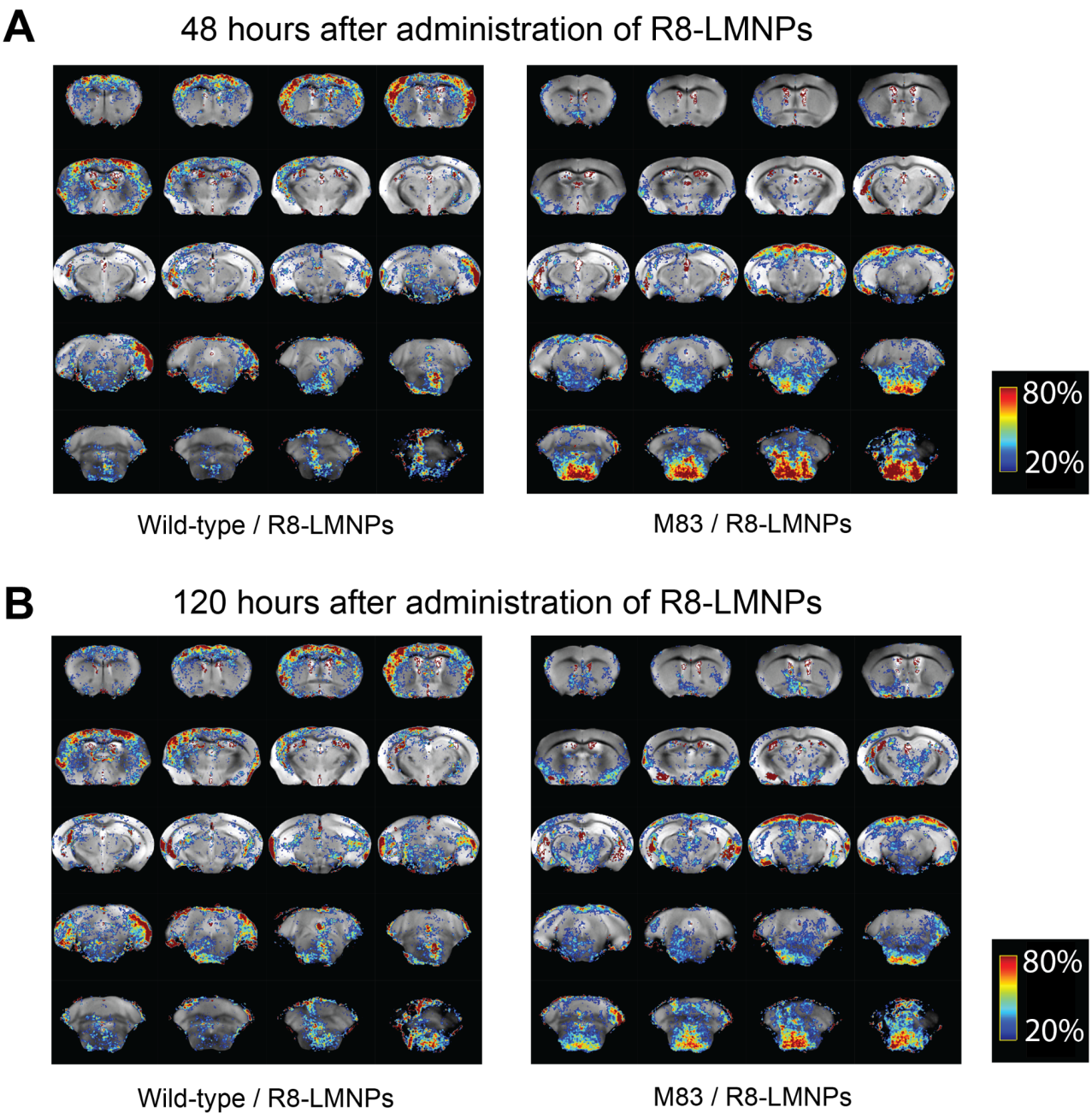


**Supplementary Figure 12. R2* % difference maps of the brains of M83 mice and age-matched wild-type control mice after injection of R8-LMNPs. (A)** 48 hours after injection, and **(B)** 120 hours after injection. R2* % difference maps display 20 anterior to posterior coronal sections of the brain. They are colorized on a scale from 0 to 100 ms, with cooler colors representing smaller % increase in R2* and warmer colors representing larger % increase in R2*. Each map represents the average % increase in R2* of all mice in a group.

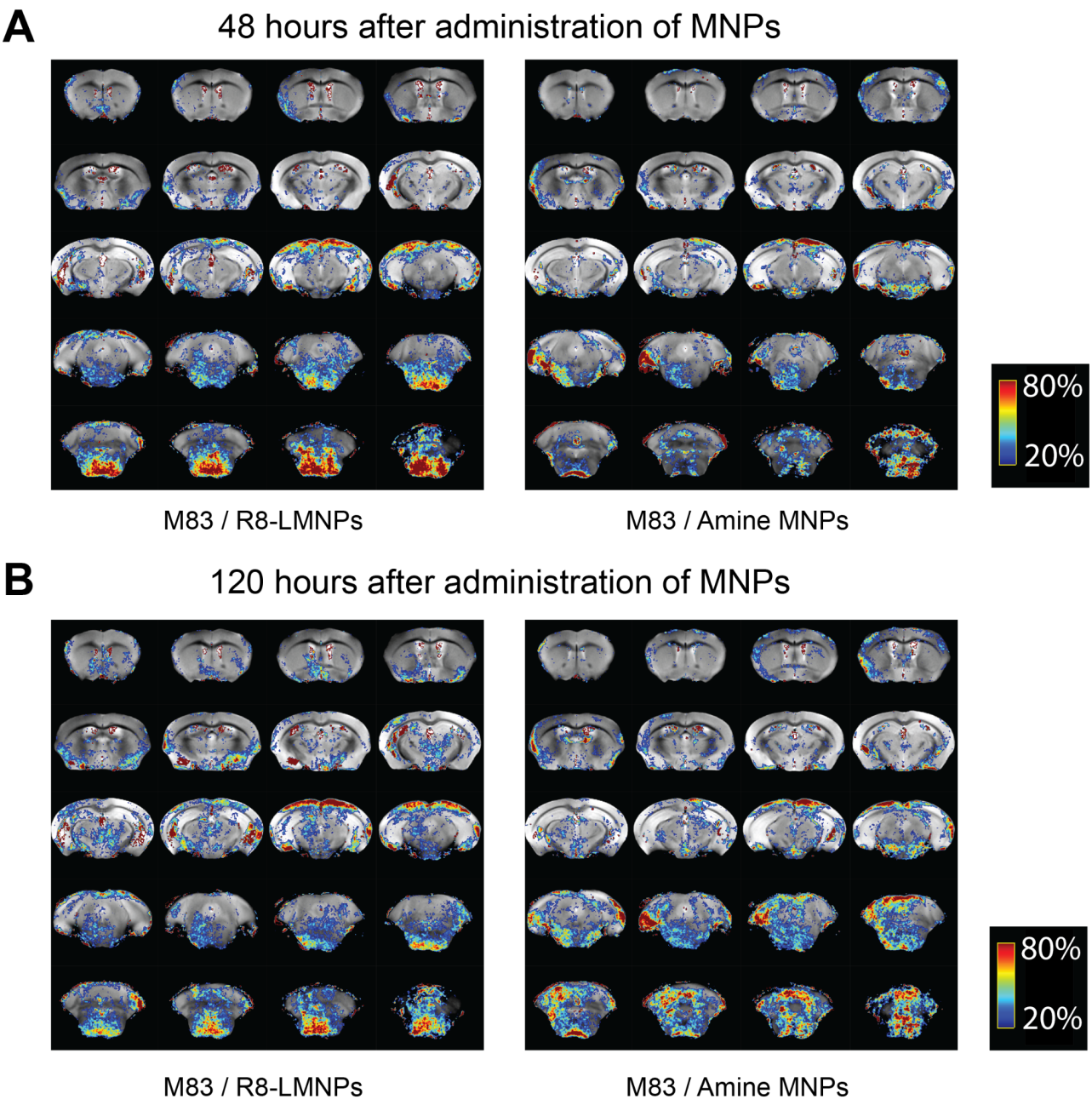


**Supplementary Figure 13. R2* % difference maps of the brains of M83 mice after injection of R8-LMNPs or amine-functionalized MNPs. (A)** 48 hours after injection, and **(B)** 120 hours after injection. R2* % difference maps display 20 anterior to posterior coronal sections of the brain. They are colorized on a scale from 0 to 100 ms, with cooler colors representing smaller % increase in R2* and warmer colors representing larger % increase in R2*. Each map represents the average % increase in R2* of all mice in a group.

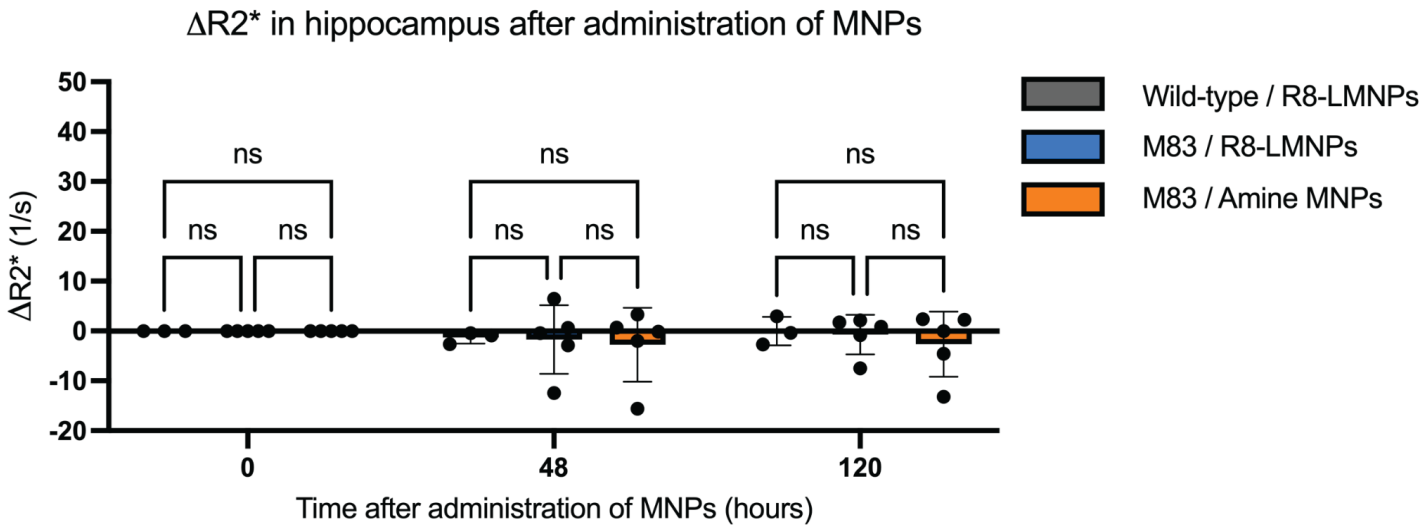


**Supplementary Figure 14. Differences in R2* relaxation rates caused by R8-LMNPs are specific to regions of the brain with α-syn pathology.** Average change in R2* relaxation rate in the hippocampus of M83 mice that received R8-LMNPs (n = 5, blue), wild-type control mice that received R8-LMNPs (n = 3, gray), and M83 mice that received amine-functionalized MNPs (n = 5, orange) either 0, 48, or 120 hours after administration of R8-LMNPs or amine MNPs. Statistical analysis was performed using two-way ANOVA (multiple comparisons using Šídák's multiple comparisons test; ns, $p > 0.05$; *, $p < 0.05$; **, $p < 0.01$; ***, $p < 0.001$; ****, $p < 0.0001$) in GraphPad Prism.

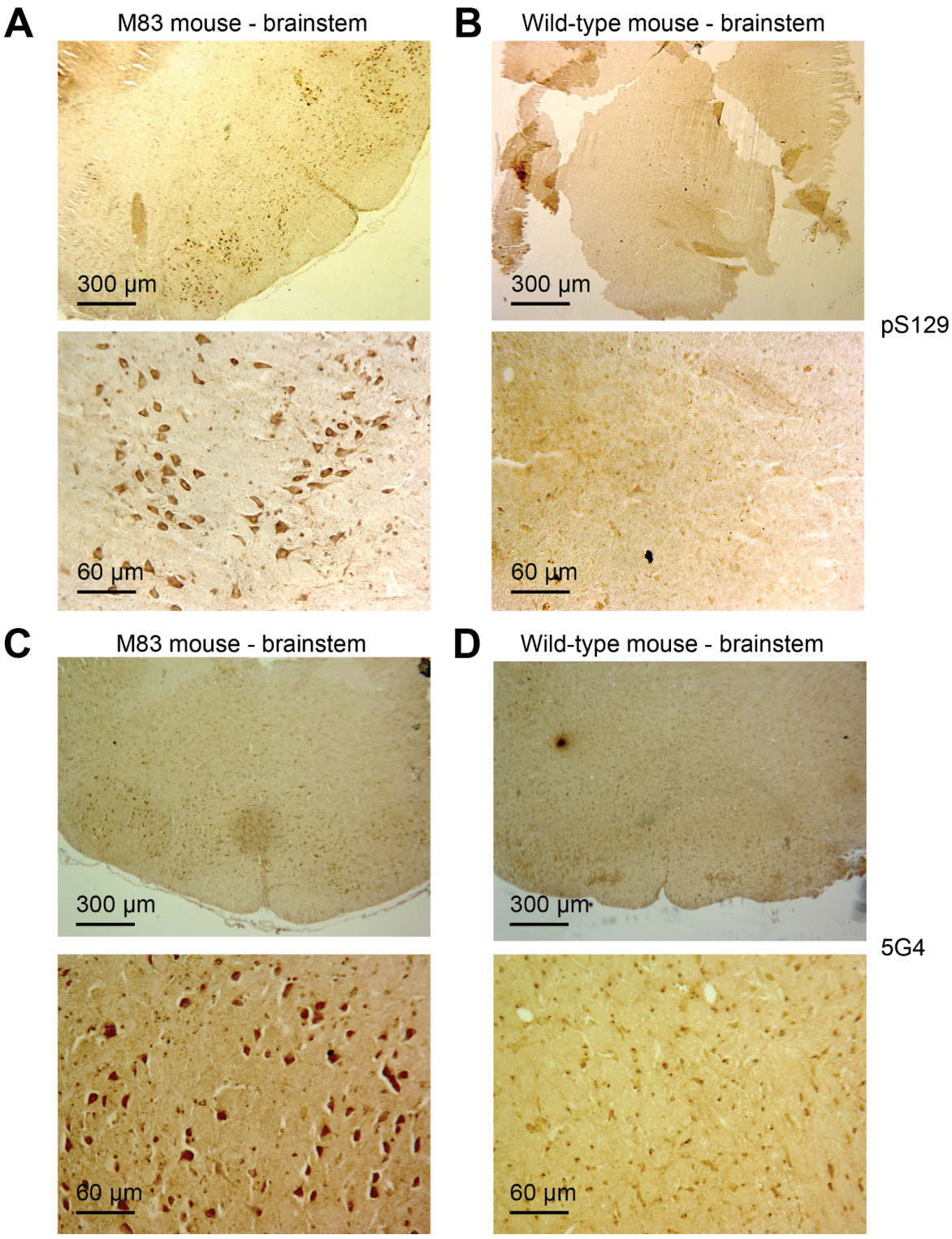


**Supplementary Figure 15. Aged M83 mice have abundant α-syn pathology in the brainstem.** Following MR imaging, 22-month-old, female, heterozygous M83 mice and age-matched, wild-type control mice were euthanized via transcardiac perfusion, and their brain

tissue was collected and fixed. Sections of fixed brain tissue were stained using **(A-B)** a rabbit polyclonal antibody against α-syn phosphorylated at S129 (pS129) and **(C-D)** a monoclonal antibody against misfolded α-syn (5G4). **(A, C)** There is α-syn pathology in the brainstem of M83 mice. **(B, D)** There is no α-syn pathology in the brainstem of wild-type control mice.

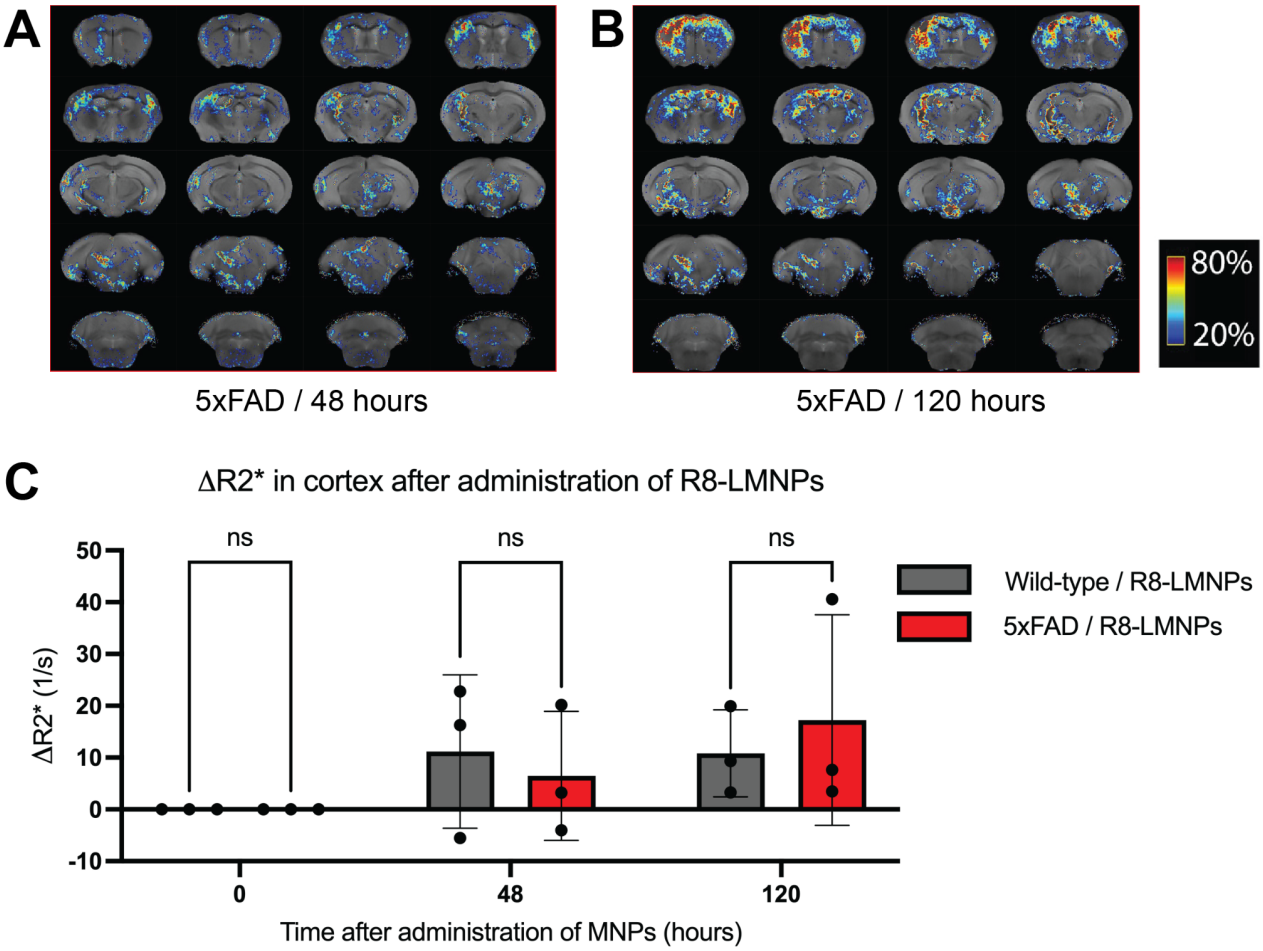


**Supplementary Figure 16. R8-LMNPs do not distinguish 5xFAD mice from wild-type control mice. (A-B)** Average R2* % difference maps of the brains of 5xFAD mice **(A)** 48 or **(B)** 120 hours after injection of R8-LMNPs. R2* % difference maps display 20 anterior to posterior coronal sections of the brain. R2* % difference maps are colorized on a scale from 0 to 100 ms, with cooler colors representing smaller % increase in R2* and warmer colors representing larger % increase in R2*. **(C)** Average change in R2* relaxation rate in the cortex of 5xFAD mice (n = 3, red) and wild-type control mice (n = 3, gray) that received R8-LMNPs (n = 3, gray) either 0, 48, or 120 hours after administration of R8-LMNPs. Statistical analysis was performed using two-way ANOVA (multiple comparisons using Šídák's multiple comparisons test; ns, $p > 0.05$; *, $p < 0.05$; **, $p < 0.01$; ***, $p < 0.001$; ****, $p < 0.0001$) in GraphPad Prism.

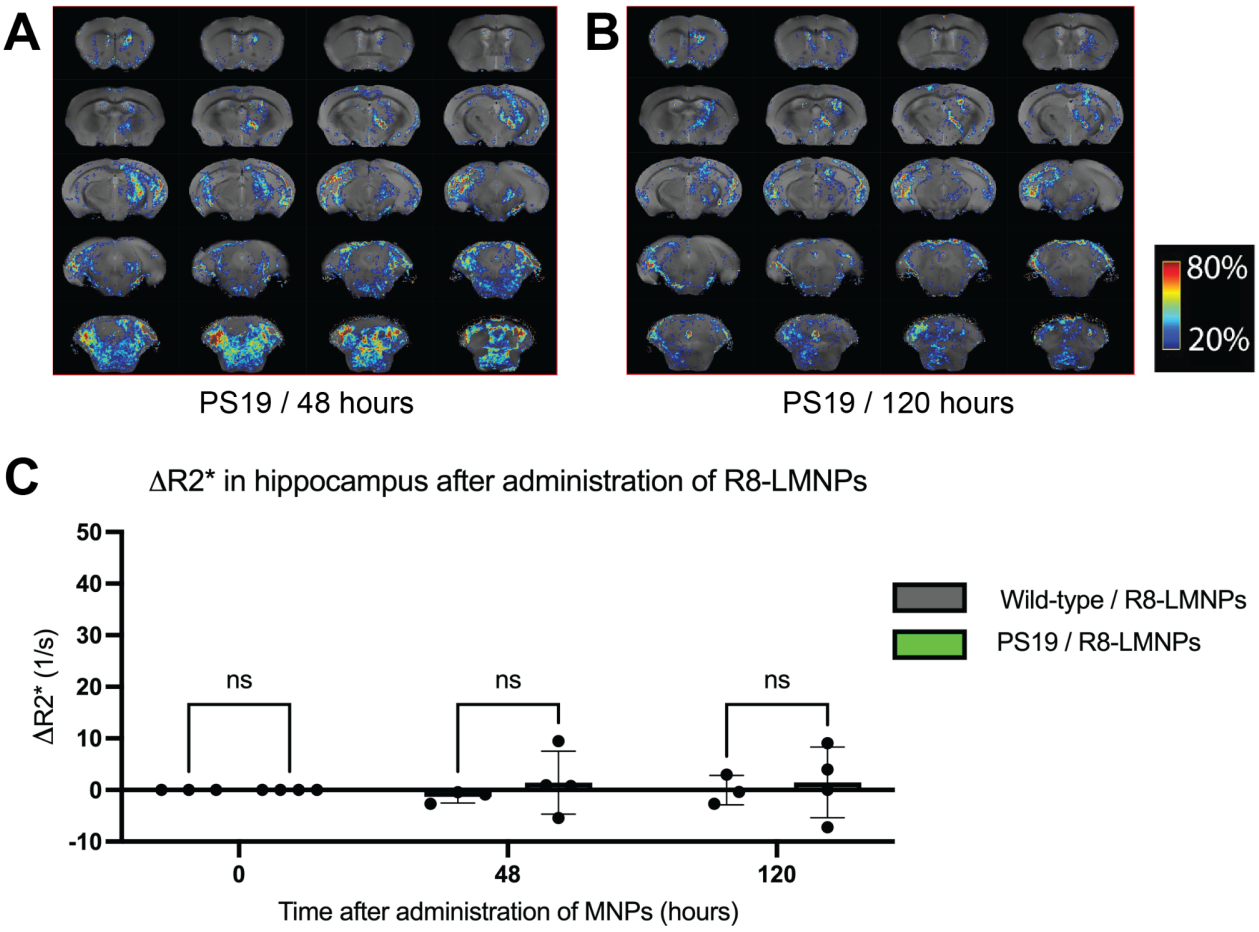


**Supplementary Figure 17. R8-LMNPs do not distinguish PS19 mice from wild-type control mice. (A-B)** Average R2* % difference maps of the brains of AD fibril-seeded PS19 mice **(A)** 48 or **(B)** 120 hours after injection of R8-LMNPs. R2* % difference maps display 20 anterior to posterior coronal sections of the brain. R2* % difference maps are colorized on a scale from 0 to 100 ms, with cooler colors representing smaller % increase in R2* and warmer colors representing larger % increase in R2*. **(C)** Average change in R2* relaxation rate in the hippocampus of PS19 mice (n = 4, green) and wild-type control mice (n = 3, gray) that received R8-LMNPs (n = 3, gray) either 0, 48, or 120 hours after administration of R8-LMNPs. Statistical analysis was performed using two-way ANOVA (multiple comparisons using Šídák's multiple comparisons test; ns, $p > 0.05$; *, $p < 0.05$; **, $p < 0.01$; ***, $p < 0.001$; ****, $p < 0.0001$) in GraphPad Prism.

CHAPTER 3

# Structure-based design of nanobodies that inhibit seeding of Alzheimer's patient–extracted tau fibrils

Romany Abskharon[1,2*], Hope Pan[1,2*], Michael R. Sawaya[1,2], Paul M. Seidler[1,2,3], Eileen J. Olivares[1], Yu Chen[1], Kevin A. Murray[1,2], Jeffrey Zhang[1,2], Carter Lantz[1], Megan Bentzel[1,2], David R. Boyer[1,2], Duilio Cascio[1,2], Binh A. Nguyen[1,2], Ke Hou[1,2], Xinyi Cheng[1,2], Els Pardon[4], Christopher K. Williams[5,6], Alissa L. Nana[7], Harry V. Vinters[5,6], Salvatore Spina[7], Lea T. Grinberg[7,8], William W. Seeley[7,8], Jan Steyaert[4], Charles G. Glabe[9], Rachel R. Ogorzalek Loo[1], Joseph A. Loo[1], David S. Eisenberg[1,2**]

1 Departments of Chemistry and Biochemistry and Biological Chemistry, UCLA-DOE Institute, Molecular Biology Institute, UCLA, Los Angeles, CA 2 Howard Hughes Medical Institute, UCLA, Los Angeles CA; 3 Present Address: Department of Pharmacology and Pharmaceutical Sciences, University of Southern California School of Pharmacy, Los Angeles, CA; 4 VIB-VUB Center for Structural Biology, VIB & Vrije Universiteit Brussel, Brussels, Belgium; 5 Department of Pathology and Laboratory Medicine, David Geffen School of Medicine, UCLA, Los Angeles, CA 90095; 6 Department of Neurology, David Geffen School of Medicine, UCLA, Los Angeles, CA 90095; 7 Department of Neurology, UCSF Weill Institute for Neurosciences, University of California, San Francisco, San Francisco, CA, USA; 8 Department of Pathology, University of California, San Francisco, San Francisco, CA, USA; 9 Department of Molecular Biology and Biochemistry, University of California, Irvine, California

* These authors contributed equally to this work.

** To whom correspondence should be addressed: David S. Eisenberg: University of California-Los Angeles 611 Charles E Young Drive, Boyer 201, Los Angeles, CA 90095; david@mbi.ucla.edu; Tel. (310) 825-3754, Fax. (310) 206-3914

Key words: Synthetic antibodies, amyloid, nanobodies, tau, prion-like spreading, inhibitor, fibril, protein structure, neurodegeneration, structural biology, seeding, zipper interface, blood-brain barrier

**Abbreviations:** AD, Alzheimer's disease; PSP, progressive supranuclear palsy; CDR, Complementarity-determining region; SEC, Size exclusion chromatography; ThT, thioflavin T; YFP, yellow fluorescent protein; PHF, paired helical filament; SF, straight filament and HRP, horseradish peroxidase; BBB, blood-brain barrier.

**Abstract**

Despite much effort, antibody therapies for Alzheimer's disease (AD) have shown limited efficacy. Challenges to the rational design of effective antibodies include the difficulty of achieving specific affinity to critical targets, poor expression, and antibody aggregation caused by buried charges and unstructured loops. To overcome these challenges, we grafted previously determined sequences of fibril-capping amyloid inhibitors onto a camel heavy chain antibody scaffold. These sequences were designed to cap fibrils of tau, known to form the neurofibrillary tangles of AD, thereby preventing fibril elongation. The nanobodies grafted with capping inhibitors blocked tau aggregation in biosensor cells seeded with post-mortem brain extracts from AD and progressive super nuclear palsy (PSP) patients. The tau capping nanobody inhibitors also blocked seeding by recombinant tau oligomers. Another challenge to the design of effective antibodies is their poor blood-brain barrier (BBB) penetration. In this study, we also designed a bispecific nanobody composed of a nanobody that targets a receptor on the BBB and a tau capping nanobody inhibitor, conjoined by a flexible linker. We provide evidence that the bispecific nanobody improved BBB penetration over the tau capping inhibitor alone after intravenous administration in mice. Our results suggest that the design of synthetic antibodies that target sequences that drive protein aggregation may be a promising approach to inhibit the prion-like seeding of tau and other proteins involved in AD and related proteinopathies.

**Significance Statement**

Alzheimer's disease (AD) is associated with aggregation of the protein tau in the brain. Antibodies that bind tau and halt its aggregation are one approach to slowing the progression of AD; however, traditional animal-produced antibodies are often limited by weak target binding, low production, and low brain delivery. We propose a method for designing antibodies in which

we graft tau-specific sequences into a camelid antibody fragment, or "nanobody". Our engineered nanobodies are easily produced and block the propagation of tau aggregation in test tube experiments. Next, by linking our best tau-targeting nanobody behind a brain-targeting nanobody, we created a double nanobody designed to enter the brain. Our results demonstrate an alternative approach to engineering antibodies to target tau aggregation.

**Introduction**

Alzheimer's disease (AD) is the most common neurodegenerative condition, accounting for dementia in dozens of millions of people worldwide (1-3). Tau pathology appears in AD when the protein tau transitions into amyloid fibrils, which can spread from cell to cell in a prion-like manner (4, 5). Many amyloid proteins, including tau, Aβ, and α-synuclein aggregate into “cross-β’’ filaments featuring β-sheets that run the length of the fibrils, stabilized by steric zippers. Steric zippers are paired β-sheets mated by tightly interdigitated side chains (2, 3, 6). Most zipper interfaces exclude water molecules, contributing to filament stability (7).

We previously determined high-resolution structures of the SVQIVY, VQIVYK, and VQIINK amyloid-driving segments of tau using micro-electron and X-ray crystallography (8-12). The hexapeptide segments VQIVYK and VQIINK are believed to drive tau aggregation and seeding (8, 13). Our structures of SVQIVY, VQIINK and VQIVYK reveal aggregation interfaces that we have used to design fibril-capping peptide inhibitors that block tau aggregation and seeding (8, 9, 12).

Recently, cryo-electron microscopy (cryo-EM) has provided structural views of tau polymorphs isolated from patients with tauopathies including AD, chronic traumatic encephalopathy (CTE), Pick’s disease, and corticobasal degeneration (CBD) (14-18). The structures of paired helical

filaments (PHF) and straight filaments (SF) extracted from patients with AD reveal tau molecules in cross-β folds, which are stabilized by steric zippers (7, 14). All show the VQIVYK segment in the core of fibrillar tau. These structural studies of fibrils extracted from postmortem tauopathy brains support the disease relevance of the SVQIVY, VQIINK and VQIVYK tau segments as targets for designed inhibitors.

Immunotherapeutic approaches show promise of being effective in treating Alzheimer's disease at early stages (19, 20). Several studies have recently demonstrated that tau-targeted immunization is a promising therapeutic approach to slow tau accumulation and PHF pathology in transgenic mouse models of tauopathies (21-24). For example, dual administration of antibodies PHF1, which recognizes S396- and S404-phosphorylated tau, and MC1, which recognizes tau in a pathological conformation, reduced tau pathology and neurodegeneration in two different mouse models (25). These promising preclinical studies have led to clinical trials of many anti-tau antibodies (26).

Structure-based design offers advantages over classical methods for generation of *de novo* antibodies. Classical immunization strategies are limited in practice by the ability to produce an effective antigen that elicits, from an inoculated animal, an antibody structure specific for the desired epitope. Classical strategies often resort to antigens with low immunogenicity which redirects the generation of antibodies away from important epitopes (27). In contrast, structure-based design takes advantage of knowledge of the epitope structure to customize antibody specificity and affinity and can be a quicker route to success provided it is possible to overcome potential pitfalls of aggregation propensity, expression difficulties in prokaryotic cells and high cost of protein production.

In choosing a system for structure-based antibody design, camelid heavy chain-only antibodies (VHH), or nanobodies, are an alternative to the traditional immunoglobulin antibody that can overcome the aforementioned pitfalls. Owing to their small size, high stability, and robust structure, they can access hidden epitopes with excellent tissue penetration *in vivo*, are amenable to protein engineering, and can be expressed in a variety of microorganisms (28, 29). In early 2019, the FDA approved the first nanobody for acquired thrombotic thrombocytopenic purpura (aTTP), a rare blood disorder characterized by blood clotting in small blood vessels (30). FDA approval of a nanobody therapeutic sets precedence that encourages the development of nanobodies to treat other pathologies, like neurodegenerative disorders.

Immunotherapies to treat neurological disorders, whether discovered by classical or structure-based strategies, face the challenge of penetrating the blood-brain barrier (BBB) (31). Immunotherapies that cannot passively cross the BBB can be delivered using receptor-mediated transcytosis (RMT), a pathway for transport of macromolecules across the BBB (32). A promising receptor for RMT is insulin-like growth factor-1 receptor (IGF1R) which is expressed on brain endothelial cells. In previous studies, nanobodies have been raised against IGF1R by immunizing a llama with an IGF1R polypeptide (33, 34). The nanobodies were demonstrated to cross the BBB in *in vitro* transwell models and in animal models (34, 35). Conjugation of an IGF1R-binding nanobody to immunotherapies for Alzheimer's disease could potentially surmount the obstacle of their limited BBB penetrability.

Here, we build on an earlier antibody design strategy in which small amyloidogenic motifs of Aβ (6–10 residues) were grafted into the variable region to create antibodies for detection and inhibition of Aβ fibrils and oligomers (36). In our study, we graft capping peptide inhibitors of tau into the variable region of a heavy chain camel antibody. We designed two generations of synthetic camel antibodies that halt prion-like seeding. In addition, we designed a bispecific

nanobody that both serves as a capping inhibitor of tau and targets IGFR1 for delivery to the brain via RMT. Our work evaluates whether therapeutic nanobodies may be constructed by incorporating inhibitors of steric-zipper sequences that drive protein aggregation and seeding.

## Results

### Design of first generation nanobody inhibitors of tau aggregation

Here we extend previous work on peptide-based inhibitors, designed to bind tau at the tips of amyloid fibrils and sterically interfere with fibril growth. These inhibitors were designed to bind to the amyloid-driving sequences VQIINK and VQIVYK of tau, and they are termed W3 and WIW, respectively (8, 11, 12). In addition to these previous capping peptide designs, we include an additional inhibitor design, VDW, a derivative of WIW that is extended by six residues at its C-terminal end to provide additional H-bonding with the complementary sequence downstream of VQIVYK. VDW binding is bolstered by a charge reversal at its C-terminus to promote ion pairing with tau Lys317, and VDW bears a Trp substitution at position 11, which would overlap with extraneous density on the surface of the AD-tau fibril reported to derive from ubiquitin (15). In short, the VDW sequence, SVWIWYEPVDWSE, is designed to bind the tau segment 305-SVQIVYKPVDLSK-317.

To design novel antibodies that target tau aggregation, we grafted the three individual capping inhibitory sequences VDW, W3, and WIW into the complementarity determining region 3 (CDR3) of a previously reported nanobody scaffold (37) (PDB entry ID: 6HEQ) (**Fig. 1A & Supplementary Table 1**). WIW and VDW nanobody fusions were designed to disrupt the VQIVYK steric zipper, while the W3 nanobody inhibitor was designed to target the VQIINK steric zipper. We call these VDW, W3, and WIW nanobodies the first generation of tau nanobody inhibitors.

To increase the conformational flexibility of the grafted nanobody inhibitor sequence, we inserted $(glycine)_3$ at both N- and C-termini of the grafted insert of the CDR3 loop. We expressed the designed nanobodies with a pelB leader sequence for expression in the bacterial periplasm with yields in the milligram range with >95% purity (**Fig. 1B & Supplementary Fig. 1 A-C**). Purification by size exclusion chromatography (SEC) of the designed nanobody reveals a prominent peak of VDW, W3 and WIW nanobodies (**Supplementary Fig. 1A-C**).

**Assessment of nanobody binding to tau**

We employed dot blot analysis to determine whether our nanobody is specific for binding recombinant tau-K18 monomers, or prefibrillar oligomers, or fibrils (**Fig. 1C**). Tau-K18 is a truncated tau construct containing the four microtubule binding domains R1–R4 (residues 244–372) (38). Dot blots confirmed the nanobody bearing the VDW inhibitor sequence recognizes tau-K18 in both the monomer and fibril states, suggesting that the binding epitope of both monomer and fibril is accessible to the designed nanobody.

**Crystal structure of the WIW nanobody inhibitor and docking simulations**

The X-ray crystal structure of WIW nanobody was determined to high (1.4 Å) resolution (**Fig. 1D, Supplementary Table 2)**. WIW nanobody crystallized with one monomer in the asymmetric unit in space group I4 and with unit cell dimensions a=78.29 b=78.29 and c= 38.22 Å. The WIW nanobody shows well resolved electron density and displays an immunoglobulin fold with a β-sandwich formed by two antiparallel β-sheets. The WIW nanobody possess three complementarity-determining regions or CDR loops (CDR1, CDR2 and CDR3) as shown in **Fig. 1D**. When grafted into the CDR3 loop, the WIW inhibitor adopts a beta-strand conformation that is compatible with steric zipper capping (**Fig. 1D**). The crystal structure shows that the designed nanobody structure agrees with the design.

We docked the determined crystal structure of the WIW nanobody to the previously published PHF structure (**Fig. 1E-F**). The CDR3 loop in the nanobody structure adopts a beta-strand secondary structure compatible with binding the steric zipper at the tip of the PHF fibril.

We pursued structural studies to investigate whether the designed WIW-tau interface (approximated in **Fig. 1E, F**) is indeed responsible for the observed inhibition of tau fibril growth by WIW (**Fig. 1 G-H**). Our first strategy was to co-crystallize WIW nanobody with tau epitope 306-VQIVYK-311; however, only crystals of WIW nanobody resulted (**Fig. 1D**). So, we turned our efforts toward computationally docking the nanobody WIW crystal structure (8fq7) on the tau PHF structure (7nrv). The results of our unbiased docking study reproduced some features of our design and suggested strategies for improvement. Three of the 29 docking models produced by ClusPro (39) featured interfaces involving the intended nanobody WIW and tau VQIVYK segments. However, the two segments exhibited antiparallel rather than parallel alignment in two of the models and out-of-register rather than in-register in the third model. We think that these deviations from our design result in part from the limitations arising from the rigid body docking approximation. The deviations could also be incurred by the docking program's drive to supplement the relatively small interface in our design with additional contacts involving regions outside CDR3. Lastly, we note that further engineering of the linker between inhibitor insert and scaffold might improve the interface with tau. E108 in our crystal structure of the WIW nanobody (**Supplementary Fig. 1E**) was not oriented to form a salt bridge with tau residue K311 as designed (**Supplementary Fig. 1D**), presumably constrained by the linker connecting it to the scaffold.

**Designed nanobodies block seeding by tau fibrils and oligomers in HEK293 biosensor cells**

We evaluated the efficacies of the nanobody designs to inhibit seeded aggregation in HEK293 cell lines stably expressing tau-K18 P301S-eYFP, referred to as “tau biosensor cells”. Specifically, we quantified and analyzed the number of puncta (tau-K18 aggregates) seeded by postmortem brain tissue extracts from donors with AD (**Supplementary Table 3**) using Image J software. As shown in **Fig. 1G-I**, seeding by brain tissue extracts from donor 1 (AD1) and donor 2 (AD2) were inhibited by the WIW capping nanobody inhibitor ($p < 0.0005$). The VDW and W3 nanobodies failed to block tau seeding by brain extracts from AD1, but inhibited tau seeding by brain extracts from AD2, suggesting lower potency of the VDW and W3 nanobody designs. We tested all three nanobodies at a concentration of 10 μM. Our evidence suggests that inhibition exhibited by WIW is caused by the designed insert and not the scaffold. If the scaffold had been responsible for the inhibition exhibited by nanobody WIW (**Fig. 1G**), then VDW and W3 would have exhibited the same level of inhibition as WIW since all three share the same scaffold.

To validate the binding of the designed inhibitor to the fibril tips, we used Immuno-EM labeling in conjunction with electron microscopy. As shown in **Fig. 1J**, the VDW nanobody binds to tau-k18 fibril tips, showing the binding to the fibrils agrees with the design. However, the VDW nanobody also binds to the sides of the fibrils. These binding sites along the sides of the fibrils may correspond to points of secondary nucleation of monomeric tau along the primary fibril that may also have an exposed epitope (40). Alternatively, the binding sites of the fibrils may be points of non-specific binding.

Next, we tested the efficacy of our capping nanobody inhibitors on aggregation seeded by recombinant tau-K18 oligomers prepared by ionic liquid 15 (IL15) as described previously (38). We used tau oligomers because they are hypothesized to promote neurotoxicity (41, 42). An EM image of recombinant tau-K18 oligomers (**Supplementary Fig. 1F)** reveals a mixture of 10-20 nm spherical oligomers has the capability to spread from cell-to-cell in a prion-like fashion

(**Supplementary Fig. 1G & H**). Seeding by tau-K18 oligomers was reduced by all nanobody designs. Notably, the WIW nanobody inhibited aggregation seeded by both PHFs and oligomers (**Supplementary Fig. 1G & H**).

**Design and testing of second generation nanobody inhibitors of tau seeding**

It has been reported that nanobodies with isoelectric points (pI) above 9.4 spontaneously penetrate cells, making them suitable for targeting intracellular proteins (43). As a result, we sought other nanobody scaffolds with extremely basic pIs, assuming they are more suitable for targeting intracellular tau protein than scaffolds with acidic pIs. To design the second generation of nanobody inhibitors, we selected a previously described nanobody scaffold with pI = 9.8, termed “scaffold 2” (44). We replaced its CDR3 with select inhibitory sequences; one construct bearing the WIW inhibitor sequence and another bearing the native tau SV sequence (**Fig. 2A & Supplementary Table 4**). We reasoned that the native tau segment could home the nanobody inhibitor to tau, and that the fused nanobody itself could sterically prevent binding of additional tau monomers to the tips of fibrils. The WIW and SV second generation nanobodies were expressed in bacteria (**Supplementary Fig. 2A & B**). To validate the efficacy of this new generation of nanobody designs for inhibiting tau aggregation, we tested the prion-like seeding of four AD patient brain extracts (**Supplementary Table 3**) in the presence or absence of the designed nanobodies using tau biosensor cells. We found that treating the AD brain extracts with the WIW or SV second generation nanobody strongly reduced the seeding by all four AD samples (**Supplementary Fig. 2C-J**).

We further explored our second generation of nanobody design by grafting another four capping inhibitory sequences of W3, M4, R9 and QIINK onto the CDR3 of a nanobody scaffold 2 (**Fig. 2A & Supplementary Table 4**). W3, M4 and R9 second generation nanobody inhibitors were designed to disrupt the A, B and C interfaces in the VQIINK steric zipper, respectively (12). The

QIINK nanobody contains a graft of the wild-type tau sequence into the CDR3 of scaffold 2 (**Fig. 2A & Supplementary Table 4**). Purification of the W3, M4, R9 and QIINK nanobodies produced high purity products after Ni-NTA column purification but with lower yield than in the scaffold 1 expression (**Supplementary Fig. 3A**). Therefore, we did not perform size exclusion chromatography after Ni-NTA purification. Western blot analysis of the capping nanobody inhibitors reveals a 15 kDa band consistent with the size analyzed by SDS PAGE (**Supplementary Fig. 3B**).

We tested the efficacy of our nanobody panel to inhibit seeding by eight AD brain extracts in biosensor cells (**Supplementary Table 3**). EM examination of a partially purified brain extract from AD donor 3 (AD3) showed an abundance of PHFs with helical morphology (**Fig. 2B)**. The concentration of tau in AD brain extracts was estimated to be 1.5-2 μM. To ensure that our capping nanobody inhibitors are specific and target the aggregation prone segments, we used a non-cognate nanobody to serve as a negative control (44). The non-cognate nanobody has the same scaffold and high pI as the designed second generation nanobodies, including CDR1 and CDR2, but a different CDR3 (**Supplementary Table 4**). All synthetic nanobodies strongly reduced seeding by AD3, AD4, and AD5 patient brain samples (**Fig. 2C-E & Supplementary Fig. 3C-E**). We observed some non-specific inhibition by the non-cognate nanobody towards AD3, but the inhibition from all designed nanobodies was significantly greater ($p < 0.0001$) than that of the non-cognate. We initially tested all nanobodies at a concentration of 10 μM.

All synthetic nanobodies strongly reduced seeding by AD6, AD7, AD8, AD9, and AD10 patient brain samples (**Supplementary Fig. 4**). Interestingly, some of the grafted nanobody designs exhibited variation toward seeding inhibition. WIW was the most potent inhibitor of seeding by AD3, AD4 and AD5 brain extracts but was less effective on AD7 and AD8 brain extracts (**Fig. 2C-E & Supplementary Fig. 4**). SV and M4 nanobodies were more effective inhibitors of AD7

and AD8 than WIW (**Fig. 2C-E & Supplementary Fig. 4**). We again used a non-cognate nanobody to serve as a negative control. The non-cognate nanobody showed no effect on seeding by AD6, AD7, AD9, and AD10. We observed non-specific inhibition by the non-cognate nanobody towards AD8. We tested all nanobodies at a concentration of 10 μM.

Next, we tested whether representative second generation nanobody WIW inhibits seeding by AD3 brain extract at various doses. WIW inhibits seeding by AD3 brain extract in a dose-dependent manner from 1-5 μM, and at 10 μM, there is a plateau in WIW's inhibitory effect (**Fig. 2F**). We again used a non-cognate nanobody to serve as a negative control which showed no effect on seeding. In addition, we wanted to ensure that our capping nanobody doesn't simply bind and sequester tau monomer instead of blocking fibril growth. We included a monoclonal antibody that binds residues 6-18 of tau, called 43D, and found that it does not reduce seeding by AD3 brain extract. Because 43D can bind tau monomer with high affinity but still does not reduce seeding, we can assume that sequestering tau monomer is not sufficient for nanobody function.

Finally, to assess the toxicity of our nanobodies, we performed a dose-dependent cell viability assay with representative second-generation nanobody WIW and found that WIW has no measurable toxicity towards Neuro 2A cells (**Fig. 2G**).

**Nanobody inhibitors block seeding by tau-K18 oligomers**

Next, we sought to determine whether our designed nanobody inhibitors could block seeding by tau oligomers. Both fibrils and oligomers can seed aggregation and thus may be targeted with our designed nanobodies. To determine if tau oligomers can be targeted by nanobody inhibitors, we prepared tau-K18 oligomers with IL15 as previously described (**Fig. 3A-C**) (38). The formation of tau-K18 oligomers was confirmed using the M204 antibody, which is specific for tau

oligomers but not monomers (**Fig. 3B**) (43). We observed that seeded aggregation by tau-K18 oligomers was strongly inhibited in the presence of the second generation WIW and SV nanobodies in tau biosensor cells (**Supplementary Fig. 2K & L**). We initially tested all nanobodies at a concentration of 10 μM.

Next, we tested whether representative second generation nanobody WIW inhibits seeding by tau-K18 oligomers at various doses. WIW inhibits seeding by oligomers in a dose-dependent manner from 1-10 μM (**Fig. 3D & E**). We again used a non-cognate nanobody to serve as a negative control. We observed non-specific inhibition by the non-cognate nanobody, but the inhibition from WIW at the same concentration was significantly greater than that of the non-cognate ($p < 0.0001$).

**Synthetic nanobodies block seeding by purified fibrils from human AD and PSP brain tissue**

To validate the efficacy of our nanobody designs for targeting disease-relevant amyloid fibrils, we extracted and purified tau fibrils from brain tissue of AD donor 3 (AD3) using a water extraction protocol as previously described (45). We used immuno-EM combined with electron microscopy to verify that the purified AD fibrils were composed of tau (**Fig. 4A**). Then we tested the efficacy of the nanobody capping inhibitors in preventing seeding by the purified tau fibrils. As shown in **Fig. 4B & C**, the designed nanobody inhibitors block seeding by purified tau fibrils, while the non-cognate nanobody shows no effect on seeding inhibition. Our nanobody designs successfully inhibit seeding of both crude brain extract and purified tau fibrils from AD patients, revealing the potential relevance of our nanobody-based designs to AD.

In addition to AD brain extracts, we expanded our evaluation of designed nanobody capping inhibitors to include post-mortem brain extracts from donors diagnosed with other tauopathies.

We tested the inhibitory power of our synthetic nanobodies on crude brain extracts from two donors with PSP. Electron micrographs of brain extract from PSP donor 1 confirmed that the extract contained fibrils with a twisted filament morphology (**Supplementary Fig. 5A & B**). As shown in **Supplementary Fig. 5C-E**, all synthetic nanobodies blocked seeding by both PSP brain extracts. The non-cognate nanobody showed no effect on seeding by either PSP extract.

**Designing a bispecific WIW nanobody that crosses the blood brain barrier**

To facilitate the delivery of tau inhibitors to wild type mouse brains, we designed a bispecific nanobody composed of IR5, a nanobody that targets the type 1 insulin-like growth factor receptor (IGF1R) and has been shown to cross the BBB, and the WIW nanobody inhibitor, conjoined by a flexible linker (**Fig. 5A**) (46). The size exclusion chromatography peak of the bispecific nanobody reveals a ~30 kDa band consistent with the size analyzed by SDS PAGE (**Fig. 5B & C**). To validate brain penetration, the bispecific nanobody was administered by tail vein injection at a dose of 20 mg/kg to C57BL/6J mice (n=3). As a comparison, the second generation WIW nanobody was administered at an equimolar dose of 10 mg/kg to C57BL/6J mice (n=3). Thirty min after dosing, the mice were euthanized by cardiac perfusion, and brain samples were collected.

Quantitative liquid chromatography-tandem mass spectrometry (LC-MS/MS) determined the bispecific WIW nanobody concentrations in three mouse brains to be 4.3-8.1 µg per g, while concentrations of second generation WIW in three mice were measured as 0 µg per g (**Fig. 5D**). Concentrations were assessed by comparing signal levels in the samples to those derived from the nanobody-spiked brain tissues of nanobody-naïve mice (**Supplementary Fig. 6-8**). The brain sample extraction protocol has been described previously (47).

## Discussion

Much effort has been applied to design antibodies to target specific, disease-relevant epitopes (27, 48). Limiting the success of this approach are the challenges of predicting CDR loop sequences that confer specific binding to their antigens as well as adequate antibody expression and stability (49, 50). To produce a panel of antibodies capable of halting pathogenic tau aggregation and prion-like seeding, we employed a grafting approach, inserting previously developed inhibitory peptides into CDR3 of a previously reported nanobody scaffold. These inhibitors were designed to target steric zipper interfaces (aggregation-driving structural motifs) that we identified in tau fibrils (8-12). We chose nanobodies as vehicles for enhancing inhibitor delivery and efficacy because: 1) nanobodies can be easily engineered and expressed in both eukaryotic and prokaryotic systems with robust protein quality (51); 2) nanobodies possess high structural stability for *in vitro* and *in vivo* applications ; 3) nanobodies display low immunogenicity risk profile which is beneficial for potential therapeutic applications (52). 4) nanobodies have a smaller size makes them useful as therapeutics for brain delivery and tissue penetration (28, 53).

We met an important requirement for design specificity by showing the WIW inhibitor segment maintains an epitope-complementary structure after grafting it into a nanobody (**Fig. 1D**). In general, antibodies contain three CDR flexible loops and CDR3 contributes most of the binding specificity for antigenic determinants. We chose to graft WIW into CDR3. After determining the atomic structure of the WIW nanobody inhibitor, we observed that CDR3 adopts a beta strand secondary structure instead of a flexible loop. It appears pre-organized to bind to the tip of the protofilament and prevent fibril elongation (**Fig. 1E & F**).

An important goal of our designed nanobody is to block the seeded spread of pathogenic tau aggregates, so we assayed our panel of designs (WIW, VDW, W3, M4 etc.) using seeds from the brains of a panel of twelve different patients in HEK293 biosensor cells. Experimental evidence suggests that a prion-like seeding mechanism is the main route for propagation and spreading tau pathology in the brain and tau seeding inhibitors may delay or prevent the progress of these maladies (54, 55). We designed two generations of synthetic nanobodies, which differ in nanobody scaffold used. For generation 2, we chose scaffold 2, which exhibits a higher pI (pI = 9.8) than scaffold 1 of generation 1, making generation 2 better candidates for crossing the BBB. The second generation nanobody inhibitors decrease seeding by AD patient brain extracts in biosensor cells **(Fig. 2, Supplementary Fig. 2, Supplementary Fig. 3, & Supplementary Fig. 4).** In addition, the second generation nanobody inhibitors decrease seeding by purified tau fibrils from AD and PSP patients **(Fig. 4 & Supplementary Fig. 5),** demonstrating that aggregation-prone interfaces of both AD and PSP tau are accessible and targeted by our designed nanobody inhibitors.

Although the molecular mechanism that leads to AD is still poorly understood, small oligomers are thought to spread tau pathology and induce neuronal toxicity in the brain (53, 56-58). To further test the efficacy of WIW and SV nanobodies against seeding by tau oligomers, we used IL15-induced tau-K18 oligomers to seed tau in biosensor cells. The WIW and SV designed nanobodies potently inhibit seeding by tau oligomers (**Fig. 3 & Supplementary Fig. 2**).

Much atomic-level structural information has supported the view that specific amyloid fibril polymorphs are linked to distinct diseases. Indeed, amyloid protein conformations may define distinct diseases and constitute a basis for classification of amyloid diseases (59). The structures of AD tau and PSP tau fibrils are quite different. In AD, tau adopts two folds: paired helical filaments and straight filaments, which both consist of an ordered core of pairs of

protofilaments comprising residues 306–378. Therefore, in AD, VQIVYK is in the ordered core and VQIINK is in the fuzzy coat. In progressive supranuclear palsy (PSP), tau adopted a single protofilament with an ordered core extended from residues 272–381 (59). Therefore, in PSP, both VQIVYK and VQIINK are in the ordered core. Our nanobody panels directed toward VQIVYK and VQIINK inhibit tau seeding by purified tau fibrils from ten donors with AD and two donors with PSP, as well as seeding by recombinant tau K18 oligomers, for which the atomic-level structure is not known. This finding suggests that the inhibitor segment seated in the nanobody could be flexible enough to recognize multiple conformations of tau.

In cases of patient AD3, AD8, and the recombinant K18 oligomers **(Fig. 2, Supplementary Fig. 4, Fig. 3)**, we observed some non-specific inhibition by the non-cognate nanobody. It is possible that the non-specific inhibition comes from some non-specific binding of tau from the nanobody scaffold. Based on the results of the unbiased docking experiment **(Supplementary Fig. 1D-E),** we are aware of a few possible configurations of non-specific binding. However, based on the finding that sequestering monomeric tau with an anti-tau antibody is not sufficient for inhibition **(Fig. 2F)**, only non-specific binding in aggregation prone regions such as the fibril core or VQIINK could contribute to the non-specific inhibition in biosensor cells. In future generations of nanobody design, we will select a scaffold with less non-specific binding and non-specific inhibition.

Finally, we designed a bispecific nanobody that both serves as a capping inhibitor of tau and targets IGF1R for delivery to the brain via RMT. We administered the bispecific nanobody to three wild-type mice and measured its concentration to be 4.3-8.1 μg per g of brain tissue using LC-MS/MS. We administered second generation WIW to three wild-type mice and did not detect WIW in brain tissue.  Our findings are consistent with the hypothesis that fusion of the WIW capping inhibitor with an IGFR1-binding nanobody improved BBB penetration after intravenous

administration in mice. Brain delivery is a major limitation of antibody-based therapeutics, so our findings may represent significant progress towards overcoming this limitation.

Because neurofibrillary tangles are formed intracellularly, our nanobodies would need to penetrate the cell membrane or be expressed in the neuronal cytoplasm to halt tau aggregation. We designed our nanobodies with a high pI (above 9.4) because it has been reported that nanobodies with a high pI spontaneously penetrate cells (43). In the future, we plan to investigate whether our nanobodies penetrate cells spontaneously or require additional modification.

In summary, we used a design approach to produce a panel of nanobody inhibitors that halt prion-like seeding by tau amyloid. By targeting the steric zipper interfaces, we designed a panel of inhibitors able to block cell-to-cell seeding by recombinant tau-oligomers, purified AD brain fibrils, and purified PSP brain fibrils. In addition, we designed a bispecific nanobody that targets IGFR1 and enter the brain via RMT. We provided evidence that the bispecific nanobody improved BBB penetration over the tau capping inhibitor alone after intravenous administration in mice. Taken together, these results demonstrate that we can use structure-based design to engineer antibodies to target tau aggregation and overcome the limitations of traditional antibody production.

## Material and methods

### Tau protein expression

Human wild-type tau-K18 (residues 244-372) was expressed in a pNG2 vector and purified as previously described (8, 38).

### Design, cloning, expression, and purification of antibody inhibitors

WIW (Scaffold 1), VDW (Scaffold 1), W3 (Scaffold 1), WIW (Scaffold 2) and SV (Scaffold 2) antibody genes were synthesized by Genscript and cloned into pMES4 vector encoded with an N-terminal pelB signal peptide for periplasmic expression, and a 6X His-tag at the C-terminal end. W3, M4, R9 and QIINK (Scaffold 2) antibody genes were synthesized by Twist Bioscience and cloned into pMES4 vector using PstI- BstEII restriction site. Bispecific WIW nanobody was synthesized by Genscript and cloned into pMES4 vector encoded with an N-terminal pelB signal peptide for periplasmic expression, and a 6X His-tag at the C-terminal end. One residue at position 145 was changed from a valine to a glutamic acid to improve protein expression yield. This residue is non-solvent facing and is outside of the three complementarity determining regions and should not affect protein function. Protein expression and purification were performed according to our previous protocol (38, 44).

### Crystallization

The WIW nanobody inhibitor was concentrated to 10 mg/mL and crystallization trials were performed by mixing equal volumes of the protein and reservoir solution. Crystals appeared from cocktails containing 0.15M ammonium sulfate 0.1M MES pH5.5 25%w/v PEG 4000 (C10: ProPlex, molecular dimensions) after 7 days at 16 °C. All crystals were cryoprotected with reservoir solution containing 35% (W/V) glycerol, and flash-frozen in liquid nitrogen.

**X-ray data collection and structure solution**

X-ray data for WIW nanobody inhibitor was collected at beamlines 24-ID-C at the Advanced Photon Source. Data was processed in XDS and XSCALE (60). Molecular replacement was performed with the program PHASER (61), using prion nanobody 484 (Protein Data Bank entry: 6HEQ) as a search model (37). Refinement and structure building was performed in PHENIX (62) and Coot (63).

**Docking**

To generate figures of the nanobody inhibitor bound to the tau PHF fibril, the crystal structure of the WIW nanobody was aligned to the relevant region of the PHF using Pymol. The beta-strand inhibitor sequence in the nanobody CDR3 region (PDB code: 8FQ7) was aligned to the top fibril layer of the VQIVYK segment of the tau PHF (PDB code: 5O3L) using the Align function of Pymol.

**Preparation of tau-k18 fibrils**

Recombinant tau-k18 was diluted to 25 μM and mixed 1x PBS, pH 7.4, 20 mM DTT, 10mM ThT, and 5% ionic liquid (HR2-214-15, HamptonResearch). Protein was liquated to 3 replicate wells of a 96-well–plate (Thermo Scientific Nunc), and plate was incubated at 37 °C for 24 h with shaking and a plastic bead to enhance agitation. The amyloid fibril formation was monitored by measuring ThT fluorescence at 440/480 nm excitation and emission wavelengths and examined using negative stain transmission EM.

**Preparation and purification of tau oligomers**

Recombinant tau-K18 at a concentration of 12 μM was incubated in 1X PBS (pH 7.4) with 10 mM DTT and 2% ionic liquid (HR2-214-15, Hampton Research) with shaking for 16-18 hours at 37 °C in a 96 well plate (Thermo Scientific Nunc) with a plastic bead to enhance agitation. The

solution was subsequently centrifuged for 5 min at 14,000 rpm to remove any large aggregates, and the supernatant was concentrated using an ultra-centrifugal spin filter with a 10 kDa cutoff (Amicon). Concentrated samples were injected on a HiLoad 16/600 Superdex 75 pg.

**Dot blot**

Tau-K18 monomer or fibrils protein was blotted to a nitrocellulose membrane (Invitrogen). The membrane was blocked in TBST (Tris-buffered saline, pH 7.6, and 0.1% Tween 20) supplemented with 5% milk and incubated with the VDW nanobody (10 µg/ml) in TBST supplemented with 2% milk for 2 hours. The membrane was then incubated with HisProbe-HRP (Thermo Scientific, Cat No.: 15165), at dilution 1:5000 in TBST for 1 hour.

In the case of human tau-K18 oligomer or monomer fractions (10 µL) purified from SEC were blotted on a nitrocellulose membrane. The membrane was then blocked using 5% milk in TBST for one hour at RT and followed by three time washing with TBST buffer. The membrane was incubated with monoclonal M204 (1:1000) in TBST supplemented with 2% milk for 1 hr at RT and followed by Goat anti-rabbit HRP (abcam, ab6721) as a secondary antibody. All membranes were developed using PierceTM ECL Plus substrate (Thermo Scientific, Cat No.: 32132).

**Immunogold electron microscopy of nanobody binding to tau-K18 fibrils**

For immunogold EM, 5 µL of tau-k18 fibrils were applied onto 400 mesh carbon-coated formvar support films mounted on cooper grids for 3 min followed by fast blotting. EM grids were blocked with 0.1% gelatin in PBS for 10 min and followed by VDW nanobody at dilution 1:100 into 0.1% gelatin-PBS and incubated with EM grids for 60 min. Then, the EM grids were washed 5x with gelatin-PBS and fast dried between washes. Grids were applied to the primary antibody (anti-His tag monoclonal antibody (HIS.H8), Invitrogen, Cat # MA1-21315 at 1:1000 dilution in 1% gelatin-PBS) and incubated for 30 minutes. Grids followed by incubation at dilution 1:8 with colloidal gold AffiniPure goat anti-Mouse IgG (Jackson Immuno Research Laboratories, Code

ID: 115-195-166) for 30 minutes. The EM grids were washed 5x with water and stained with 4 µL of 2% uranyl acetate for 2 min and followed by washing with an additional 4 µL of 2% uranyl acetate and allowed to dry for 10 min. The grids were imaged using a T12 (FEI) election microscope.

**Preparation of brain crude tau seeds**

Post-mortem tissue for neuropathlogically confirmed tauopathy cases from brain regions indicated in **Supplementary Table 3** and figure legends were fresh-frozen and extracted without freeze-thaw. Tissue was cut into a 0.2-0.3 g section on a block of dry ice, and then manually homogenized in a 15 ml disposable tube in 1 ml of 50 mM Tris, pH 7.4 with 150 mM NaCl containing 1X HALT protease inhibitor. Samples were then aliquoted to PCR tubes and sonicated in a cuphorn bath for 150 min under 30% power at 4 °C in a recirculating ice water bath, according to reference (64).

**Tau biosensor cell maintenance and seeding**

HEK293 cell lines stably expressing tau-K18 P301S-eYFP, referred to as “tau biosensor cells” were engineered by Marc Diamond’s lab at UTSW (65) and used without further characterization or authentication. Cells were maintained in DMEM (Life Technologies, cat. 11965092) supplemented with 10% (vol/vol) FBS (Life Technologies, cat. A3160401), 1% penicillin/streptomycin (Life Technologies, cat. 15140122), and 1% Glutamax (Life Technologies, cat. 35050061) at 37 °C, 5% CO2 in a humidified incubator. Fibrils and patient- derived seeds were incubated at 4 °C for 16 hours with nanobody inhibitor to yield a final inhibitor concentration of 10 µM (on the biosensor cells). A non-cognate nanobody and an antibody binding to residues 6-18 (BioLegend Cat. No. 816601) were used as negative controls. For seeding, inhibitor-treated seeds were sonicated in a cuphorn water bath for 3 minutes, and then mixed with 1 volume of Lipofectamine 2000 (Life Technologies) prepared by diluting 2 µL of

Lipofectamine in 18 µL of OptiMEM. After twenty minutes, 10 µL of seeds were added to 90 µL of tau biosensor cells. After six days, the number of seeded aggregates was determined by imaging the entire well of a 96-well plate in triplicate using a Celigo Image Cytometer (Nexcelom) in the YFP channel. Aggregates were counted using ImageJ (66) by subtracting the background fluorescence from unseeded cells and then counting the number of peaks with fluorescence above background using the built-in Particle Analyzer. The number of aggregates was normalized to the confluence of each well, and dose- response plots were generated by calculating the average and standard deviations from triplicate measurements. For high quality images, cells were photographed on a ZEISS Axio Observer D1 fluorescence microscope using the YFP fluorescence channel.

**Fibril extraction of AD and PSP brain tissues**

The extraction of fibrils from human tissue was performed according to previous protocol (48).

**Negative-stain transmission electron microscopy**

EM samples were prepared by applying 5 µL of Tau-K18 oligomers or AD and PSP filaments to glow-discharged grid CF150-Cu 150 mesh carbon films mounted on copper grids (Electron Microscopy Sciences) and incubating on the grid for 3 min. The samples were then blotted off and the grids were stained with 12 µL of 2% uranyl acetate for 2 min. The grids were blotted off and allowed to dry for 10 min. Grid was imaged using a T12 (FEI) electron microscope.

**Immnogold electron microscopy of extracted tau fibrils**

Nanogold particle binding was performed as described (67). 4 µL of sarkosyl insoluble tau fibril extracted from AD patients were used with primary antibody Tau46 (BioLegend cat#806604, 1:100 dilution in 1% gelatin-PBS) and secondary goat anti-mouse antibody (Jackson

ImmunoResearch Laboratories Inc cat# 115-195-146, 1:8 dilution in 1% gelatin-PBS). TEM images were acquired with a FEI Tecnai T12 transmission electron microscope at 120kV.

**Cell viability assay**

Neuro-2a cells (ATCC catalog # CCL-131) were cultured in MEM media (Life Technologies catalog # 11095-080) with 10% FBS (Life Technologies catalog # 10437010) and 1% penicillin–streptomycin (Life Technologies catalog # 15140122) in a 5% $CO_2$ incubator at 37 °C. N2a cells were plated onto clear 96-well plates (Costar catalog # 3596) at 5,000 cells/well in 90 µL culture media. After 24 h, the nanobody was added at various concentrations. After incubation for an additional 24 h, 20 µL thiazolyl blue tetrazolium bromide MTT dye (Sigma; 5 mg/mL stock in DPBS) was added to each well and then incubated for 3.5 h at 37 °C. Removal from the incubator and replacement of well media with 100 µL of 100% DMSO halted the assay. Absorbance was measured at 570 nm using a SpectraMax M5 reader. A background reading at 700 nm was subtracted from the 570 nm reading. Well readings were normalized to vehicle-alone–treated cells (designated as 100% viable) and cells treated with 100% DMSO (designated as 0% viable).

**Animal experiments**

All animal experiments were approved by the UCLA Animal Research Committee and performed under oversight of the Division of Laboratory Animal Medicine (DLAM). C57BL/6J mice (Jackson Laboratories: JAX:000664) were housed on a 12-hr light/dark schedule.

**Sample preparation for LC-MS/MS analysis**

Mice were injected intravenously with the bispecific nanobody (IR5-WIW) at a concentration of 20 mg/kg (n = 3) or the second generation WIW nanobody at a concentration of 10 mg/kg (n = 3) and sacrificed by perfusion 30 min post-injection. Brains were collected by standard

dissection and immediately frozen. For each brain, 100 mg was dissected and homogenized in 1 mL of 1x SDS buffer (2% SDS, pH 6.8) with a Fisherbrand 850 Homogenizer for 15 seconds. Next, each 1 mL of homogenate was concentrated using a Labconco CentriVap Benchtop Vacuum Concentrator to 500 µL. Each brain homogenate (90 µL) was mixed with 30 µL of loading dye including β-mercaptoethanol and urea. Next, 40 µL of the brain homogenate/loading dye mixture was run in three wells of a NuPAGE™ 4 to 12%, Bis-Tris, 1.0 mm, 10-well gel. Coomassie blue-stained bands were then excised for LC-MS/MS sample preparation. For brain samples with IR5-WIW, the gel was cut in the range of 20-30 kDa. For brain samples with WIW, the gel was cut in the range of 10-15 kDa. Additional details about the tryptic digestion, tandem mass spectrometry, and quantification by parallel reaction monitoring are provided in the supplementary material. Proteomic datasets submitted to the ProteomeXchange Consortium through the MassIVE repository are identified as PXD043069.

**Acknowledgments**

This work is based upon research conducted at the Northeastern Collaborative Access Team (NECAT) beamlines, which are funded by the National Institute of General Medical Sciences from the National Institutes of Health (P30 GM124165). The Pilatus 6M detector on 24-ID-C beam line is funded by a NIH-ORIP HEI grant (S10 RR029205). This research used resources of the Advanced Photon Source, a U.S. Department of Energy (DOE) Office of Science User Facility operated for the DOE Office of Science by Argonne National Laboratory under Contract No. DE-AC02-06CH11357. We thank the staff of the NECAT beamlines for their expert support. We also acknowledge 1R01AG070895 (DSE), R01 AG048120 (DSE) and RF1AG056507 (CG) from the National Institute on Aging, 1F32 NS095661 from the National Institute of Neurological Disorders and Stroke (PMS), R35GM145286 from the National Institute of General Medical Sciences (JAL), A2016588F from the BrightFocus Foundation (PMS), and HHMI for support.

H.P. is supported by the UCLA–Caltech Medical Scientist Training Program (GM08042) and the UCLA Chemistry–Biology Interface Training Grant (US Public Health Service National Research Service Award 5T32GM008496). E.O. acknowledges support by the National Institute of General Medical Sciences of the National Institutes of Health under Award Number T32GM145388. C.L. acknowledges support from the Ruth L. Kirschstein National Research Service Award program (GM007185).

## Conflict of interest

DSE is SAB chair and an equity holder of ADRx, Inc.

## Author contributions

R.A., H.P., and D.S.E. designed research; R.A., H.P., M.R.S., P.M.S., E.O, Y.C., K.A.M., J.Z., C.L., M.B., D.R.B., D.C., B.A.N, K.H., and X.C. performed research; R.A., H.P., M.R.S., P.M.S., E.O., Y.C., J.Z., C.L., D.R.B., E.P., J.S., C.G.C, R.R.O.L., J.A.L., and D.S.E. analyzed data; C.K.W., A.L.N., H.V.V., S.S., L.T.G., and W.W.S. contributed patient post-mortem brain tissue; R.A., H.P., M.R.S., and D.S.E., wrote the paper.

## Data availability

Plasmid for bacterial expression of nanobodies was submitted to Addgene with the ID number XXXXXX (identifier will be provided upon acceptance for publication). Coordinate was submitted to the Protein Data Bank (PDB) with code 8FQ7 for the WIW nanobody inhibitor. Proteomic datasets submitted to the ProteomeXchange Consortium through the MassIVE repository are identified as PXD043069. All other study data are included in the article and/or SI Appendix.

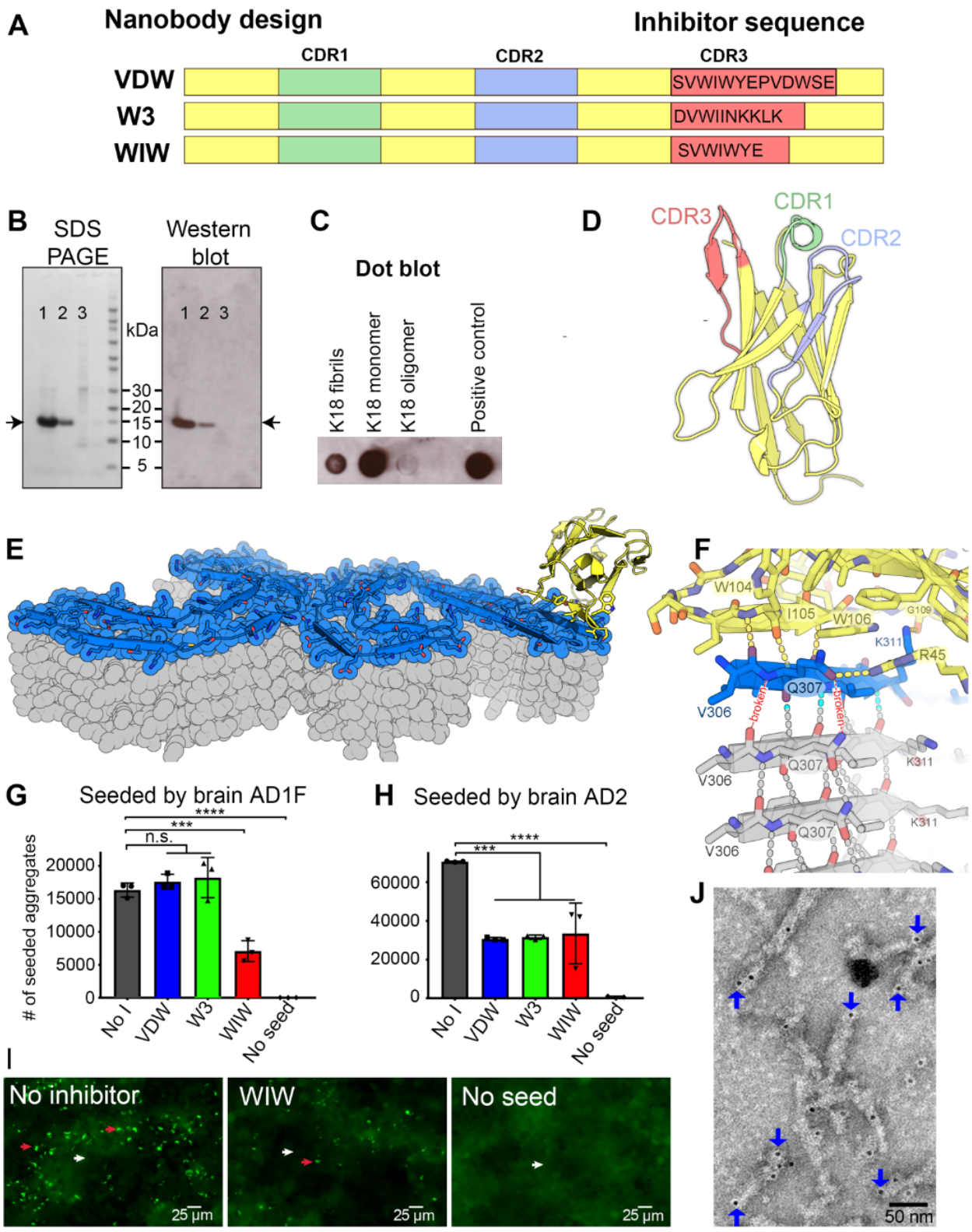
A
Nanobody design
Inhibitor sequence
CDR1
CDR2
CDR3
VDW
SVWIWYEPVDWSE
W3
DVWIINKKLK
WIW
SVWIWYE
B
SDS PAGE
Western blot
1 2 3
kDa
30
20
15
10
5
C
Dot blot
K18 fibrils
K18 monomer
K18 oligomer
Positive control
D
CDR3
CDR1
CDR2
E
F
W104
I105
W106
G109
K311
R45
Q307
V306
broken
G
Seeded by brain AD1F
# of seeded aggregates
n.s.
No I
VDW
W3
WIW
No seed
H
Seeded by brain AD2
I
No inhibitor
WIW
No seed
25 µm
J
50 nm

**Figure 1. Design and testing of first generation nanobody inhibitors of tau seeding. (A)** Schematic representation of nanobody designs. The tau inhibitor sequences are grafted into the CDR3 of heavy chain of VDW, W3 and WIW nanobodies. **(B)** SDS/PAGE and Western blot analysis of VDW nanobody purification using anti-His tag antibody, lanes 1 & 2 = Nanobody elution fractions, lane 3 = Flow-through. The SDS/PAGE gel was stained with Coomassie blue. **(C)** Dot blot showing immunoreactivity of VDW nanobody towards fibrils and monomer of tau-K18. The positive control protein is unrelated to tau and has a His tag. **(D)** X-ray crystal structure of the WIW nanobody inhibitor showing its CDRs. CDR1 in green, CDR2 in blue and CDR3 in red. **(E)** Model of the WIW nanobody inhibitor (yellow) capping the end of PHF filament with the top layer shown in blue. **(F)** Detailed model of the hydrogen-bonded interaction (yellow dotted lines) of the designed inhibitor and PHF fibrils. The side chain interaction is shown in yellow dots whereas the broken hydrogen bonds are shown in red dots. **(G-H)** Quantification of the effects of VDW, W3 and WIW nanobodies on inhibition of seeding by brain extracts from AD brain tissues (AD1 F, frontal lobe and AD2), measured in HEK293 biosensor cells expressing YFP-tagged tau-K18. The inhibitor concentration of all nanobodies was 10 μM on the biosensor cells. The experiment was performed in technical triplicate. Statistical analysis was performed using one-way ANOVA followed by a Tukey's multiple comparison test (ns, $p > 0.05$; *, $p \leq 0.05$; **, $p \leq 0.01$; ***, $p \leq 0.001$; ****, $p \leq 0.0001$) in GraphPad Prism. **(I)** Representative images of seeding and inhibition in HEK293 biosensor cells expressing YFP-tagged tau-K18. Cells seeded with brain extracts from AD Donor 2 (AD2) without pre-treatment with nanobodies (left panel), and following overnight incubation with WIW nanobody (as indicated). Representative cells that contain aggregates are marked by red arrows, and cells without by white arrows. **(J)** Representative EM of immune-gold labeling with antibodies of VDW nanobody, and tau-k18 fibrils. Fibril binding at the tip is marked by blue arrows.

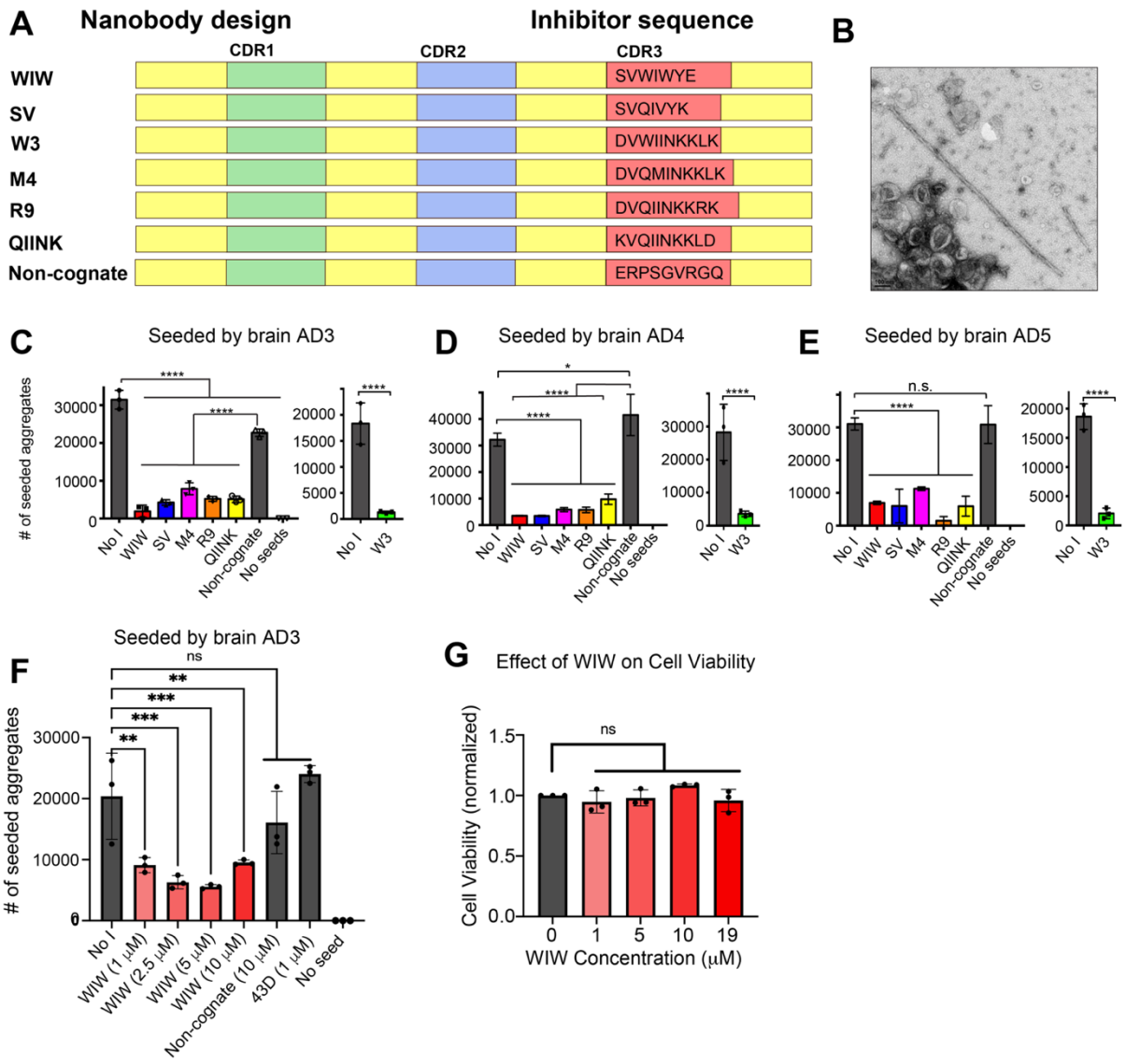


**Figure 2. Design and testing of second generation capping nanobodies that inhibit the seeding of tau aggregation by extracts from autopsied brains of AD patients. (A)** Schematic representation of nanobody designs, showing the tau inhibitor sequences grafted into the CDR3 of heavy chain of the WIW, SV, W3, M4, R9 and QIINK nanobodies. **(B)** EM of fibrils from AD patient brain extract (AD3). Scale bar 100 nm. Brain extracted-fibrils show two twisted protofilaments. **(C-E)** Quantification of the inhibitory effect of WIW, SV, W3, M4, R9, QIINK and non-cognate nanobodies on inhibition of seeding by AD patient brain extracts. The inhibitor concentration of all nanobodies was 10 μM on the biosensor cells. The experiment was

performed in technical triplicate. Statistical analysis was performed using one-way ANOVA followed by a Tukey's multiple comparison test (ns, $p > 0.05$; *, $p \leq 0.05$; **, $p \leq 0.01$; ***, $p \leq 0.001$; ****, $p \leq 0.0001$) in GraphPad Prism. **(C)** AD3. **(D)** AD4. **(E)** AD5. “No I” indicates no inhibitor. (**F**) Representative second-generation nanobody WIW inhibits seeding by brain extract AD3 at doses ranging from 1-10 μM. The experiment was performed in technical triplicate. Statistical analysis was performed using one-way ANOVA followed by a Tukey's multiple comparison test (ns, $p > 0.05$; *, $p \leq 0.05$; **, $p \leq 0.01$; ***, $p \leq 0.001$; ****, $p \leq 0.0001$) in GraphPad Prism. (**G**) Representative second-generation nanobody WIW demonstrates no toxicity towards Neuro 2A cells. The experiment was performed in technical triplicate. Statistical analysis was performed using one-way ANOVA followed by a Tukey's multiple comparison test (ns, $p > 0.05$; *, $p \leq 0.05$; **, $p \leq 0.01$; ***, $p \leq 0.001$; ****, $p \leq 0.0001$) in GraphPad Prism.

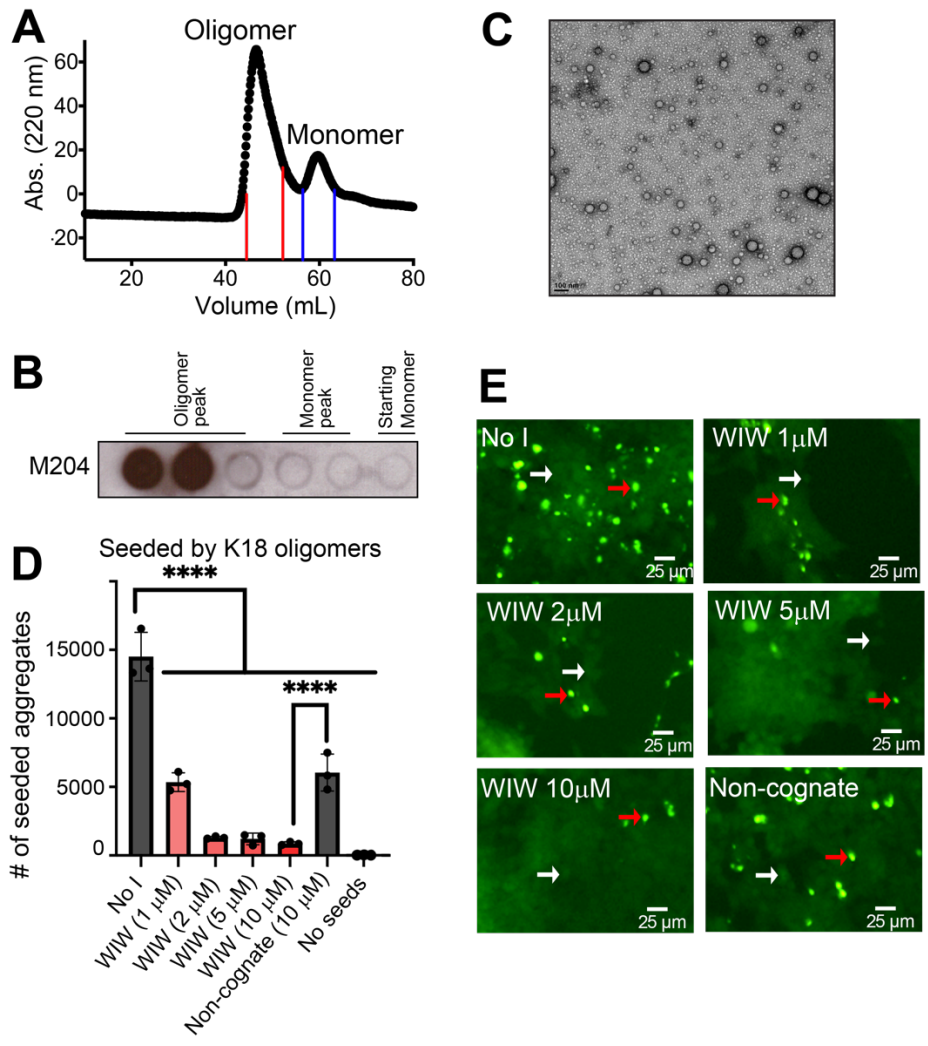


**Figure 3. Inhibition of seeding by tau-K18 oligomers using the second generation of WIW capping nanobodies. (A)** Purification of tau-K18 oligomers after SEC using a S75 10/300 column as previously described (43). Fractions marked between the solid lines were pooled for use. **(B)** Dot blot of tau-K18 oligomer (left set of three) and monomer (middle set of two) fractions eluted from SEC column and starting tau-K18 monomer used to form oligomers (right sample). M204 is anti-oligomer monoclonal antibody that binds tau-K18 oligomer but not

monomer. **(C)** Electron micrographs of tau-K18 oligomers show spherical particles with a diameter of 10-20 nm. Scale bar 100 nm. **(D)** Representative second-generation nanobody WIW inhibits seeding by tau K18 oligomers at doses ranging from 1 to 10 μM. The experiment was performed in technical triplicate. Statistical analysis was performed using one-way ANOVA followed by a Tukey's multiple comparison test (ns, $P > 0.05$; *$P \leq 0.05$; **$P \leq 0.01$; ***$P \leq 0.001$; ****$P \leq 0.0001$) in GraphPad Prism. **(E)** Representative images of seeding and inhibition by WIW and SV nanobodies. Representative cells containing aggregates are marked by red arrows, and cells without by white arrows.

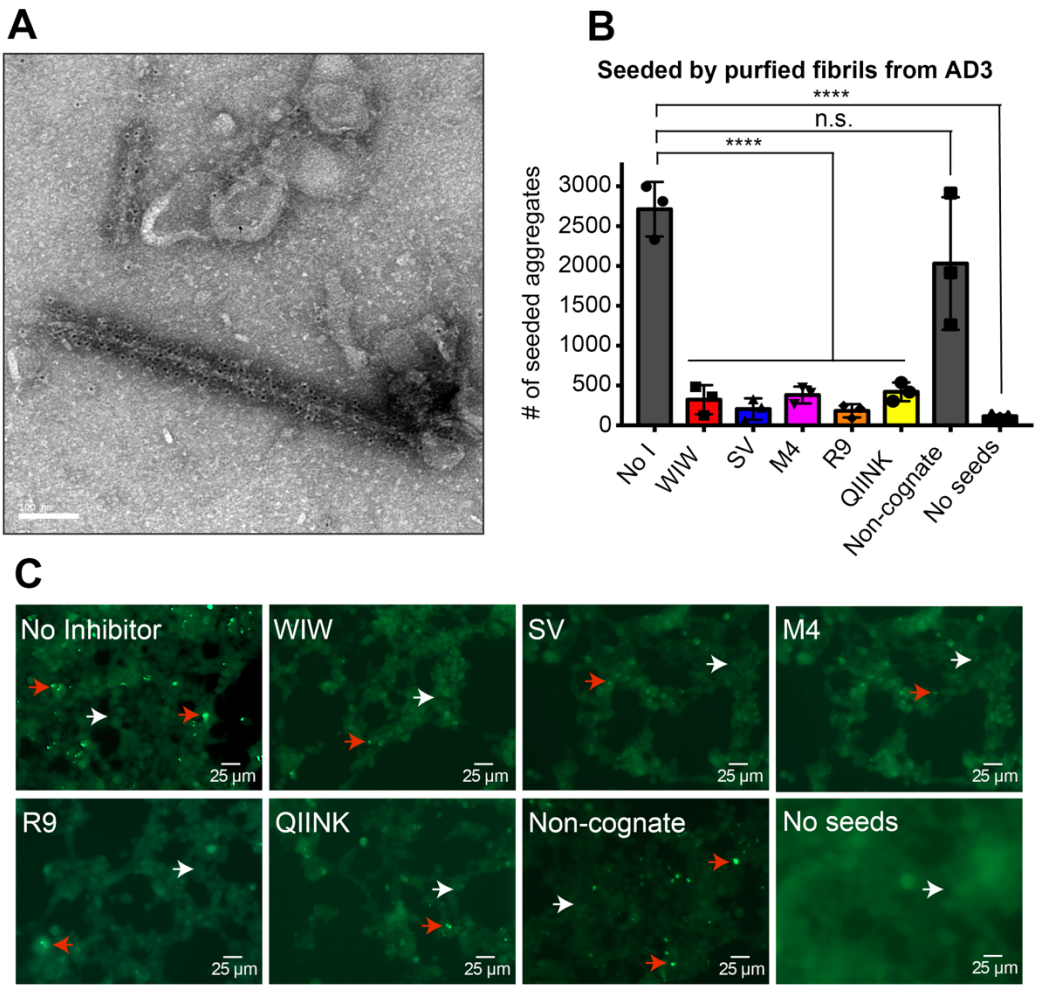


**Figure 4. Designed capping nanobodies inhibit the seeding of purified tau fibrils from human brain donor with AD pathology. (A)** Electron micrograph of purified fibrils from brain donor AD3 immunogold labeled by an anti-tau antibody. **(B)** Quantification of the inhibitory effect of WIW, SV, M4, R9, QIINK and non-cognate nanobodies on inhibition of seeding by purified AD brain fibrils (AD3). The inhibitor concentration of all nanobodies was 10 µM on the biosensor cells. The experiment was performed in technical triplicate. Statistical analysis was performed using one-way ANOVA followed by a Tukey's multiple comparison test (ns, $p > 0.05$; *, $p \leq 0.05$; **, $p \leq 0.01$; ***, $p \leq 0.001$; ****, $p \leq 0.0001$) in GraphPad Prism. **(C)** Representative images of seeding and inhibition of AD3 fibrils in HEK293 biosensor cells expressing YFP-tagged tau-K18.

Representative cells containing aggregates are marked by red arrows, and cells without by white arrows. The abbreviation of no inhibitor is “No I”.

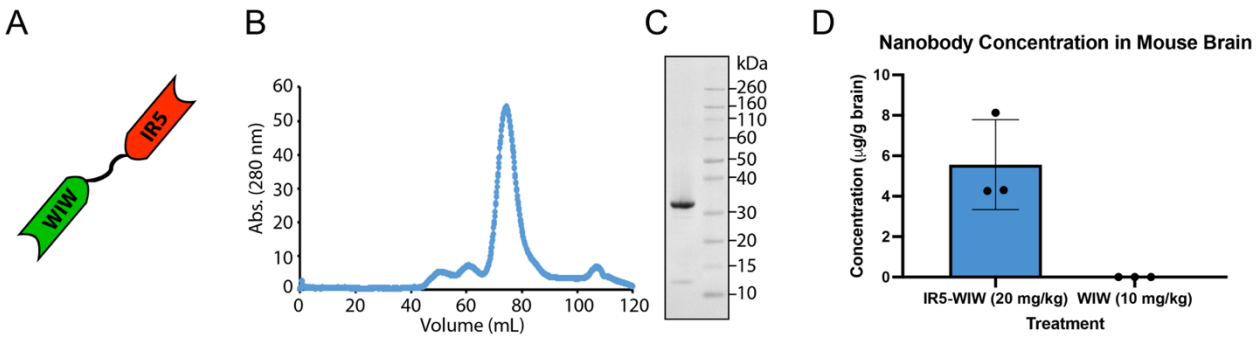


**Figure 5. Designed bispecific nanobody that crosses the blood brain barrier. (A)** The bispecific nanobody constructed by conjoining the WIW nanobody and IR5 Nanobody (46) with a flexible linker of sequence (Gly4Ser)3. **(B)** S75 SEC of bispecific WIW nanobody showing a prominent species for the collected middle peak fractions. **(C)** SDS-PAGE analysis of prominent bispecific WIW reveals one band with ~30 kDa. **(D)** Concentration of the bispecific nanobody and second generation WIW nanobody in wild type mouse brain (n = 3 mice for each nanobody). Nanobodies were quantified using LC-MS/MS.

**References**


1. Wilcock GK & Esiri MM (1982) Plaques, tangles and dementia. A quantitative study. *J Neurol Sci* 56(2-3):343-356.

2. Selkoe DJ (1991) The molecular pathology of Alzheimer's disease. *Neuron* 6(4):487-498.

3. Hardy JA & Higgins GA (1992) Alzheimer's disease: the amyloid cascade hypothesis. *Science* 256(5054):184-185.

4. Ayers JI, Giasson BI, & Borchelt DR (2018) Prion-like Spreading in Tauopathies. *Biol Psychiatry* 83(4):337-346.

5. Goedert M, Eisenberg DS, & Crowther RA (2017) Propagation of Tau Aggregates and Neurodegeneration. *Annu Rev Neurosci* 40:189-210.

6. Selkoe DJ & Hardy J (2016) The amyloid hypothesis of Alzheimer's disease at 25 years. *EMBO Mol Med* 8(6):595-608.

7. Eisenberg DS & Sawaya MR (2017) Neurodegeneration: Taming tangled tau. *Nature* 547(7662):170-171.

8. Seidler PM*, et al.* (2018) Structure-based inhibitors of tau aggregation. *Nat Chem* 10(2):170-176.

9. Sievers SA*, et al.* (2011) Structure-based design of non-natural amino-acid inhibitors of amyloid fibril formation. *Nature* 475(7354):96-100.

10. Zheng J*, et al.* (2011) Macrocyclic beta-sheet peptides that inhibit the aggregation of a tau-protein-derived hexapeptide. *J Am Chem Soc* 133(9):3144-3157.

11. Sawaya MR*, et al.* (2007) Atomic structures of amyloid cross-beta spines reveal varied steric zippers. *Nature* 447(7143):453-457.

12. Seidler PM*, et al.* (2019) Structure-based inhibitors halt prion-like seeding by Alzheimer's disease-and tauopathy-derived brain tissue samples. *J Biol Chem* 294(44):16451-16464.

13. von Bergen M*, et al.* (2000) Assembly of tau protein into Alzheimer paired helical filaments depends on a local sequence motif ((306)VQIVYK(311)) forming beta structure. *Proc Natl Acad Sci U S A* 97(10):5129-5134.

14. Fitzpatrick AWP*, et al.* (2017) Cryo-EM structures of tau filaments from Alzheimer's disease. *Nature* 547(7662):185-190.

15. Arakhamia T*, et al.* (2020) Posttranslational Modifications Mediate the Structural Diversity of Tauopathy Strains. *Cell* 180(4):633-644 e612.

16. Falcon B*, et al.* (2019) Novel tau filament fold in chronic traumatic encephalopathy encloses hydrophobic molecules. *Nature* 568(7752):420-423.

17. Falcon B*, et al.* (2018) Structures of filaments from Pick's disease reveal a novel tau protein fold. *Nature* 561(7721):137-140.

18. Zhang W*, et al.* (2020) Novel tau filament fold in corticobasal degeneration. *Nature* 580(7802):283-287.

19. Sigurdsson EM (2018) Tau Immunotherapies for Alzheimer's Disease and Related Tauopathies: Progress and Potential Pitfalls. *J Alzheimers Dis* 66(2):855-856.

20. Steinbrook R (2021) The Accelerated Approval of Aducanumab for Treatment of Patients With Alzheimer Disease. *JAMA Intern Med* 181(10):1281.

21. Bi M, Ittner A, Ke YD, Gotz J, & Ittner LM (2011) Tau-targeted immunization impedes progression of neurofibrillary histopathology in aged P301L tau transgenic mice. *PLoS One* 6(12):e26860.

22. Asuni AA, Boutajangout A, Quartermain D, & Sigurdsson EM (2007) Immunotherapy targeting pathological tau conformers in a tangle mouse model reduces brain pathology with associated functional improvements. *J Neurosci* 27(34):9115-9129.

23. Boutajangout A, Quartermain D, & Sigurdsson EM (2010) Immunotherapy targeting pathological tau prevents cognitive decline in a new tangle mouse model. *J Neurosci* 30(49):16559-16566.

24. Roberts M*, et al.* (2020) Pre-clinical characterisation of E2814, a high-affinity antibody targeting the microtubule-binding repeat domain of tau for passive immunotherapy in Alzheimer's disease. *Acta Neuropathol Commun* 8(1):13.

25. Chai X*, et al.* (2011) Passive immunization with anti-Tau antibodies in two transgenic models: reduction of Tau pathology and delay of disease progression. *J Biol Chem* 286(39):34457-34467.

26. Mullard A (2021) Failure of first anti-tau antibody in Alzheimer disease highlights risks of history repeating. *Nat Rev Drug Discov* 20(1):3-5.

27. Sormanni P, Aprile FA, & Vendruscolo M (2015) Rational design of antibodies targeting specific epitopes within intrinsically disordered proteins. *Proc Natl Acad Sci U S A* 112(32):9902-9907.

28. Muyldermans S (2013) Nanobodies: natural single-domain antibodies. *Annu Rev Biochem* 82:775-797.

29. Hamers-Casterman C*, et al.* (1993) Naturally occurring antibodies devoid of light chains. *Nature* 363(6428):446-448.

30. Morrison C (2019) Nanobody approval gives domain antibodies a boost. *Nat Rev Drug Discov* 18(7):485-487.

31. Terstappen GC, Meyer AH, Bell RD, & Zhang W (2021) Strategies for delivering therapeutics across the blood-brain barrier. *Nat Rev Drug Discov* 20(5):362-383.

32. Zhang W*, et al.* (2020) Differential expression of receptors mediating receptor-mediated transcytosis (RMT) in brain microvessels, brain parenchyma and peripheral tissues of the mouse and the human. *Fluids Barriers CNS* 17(1):47.

33. Alata W*, et al.* (2022) Targeting insulin-like growth factor-1 receptor (IGF1R) for brain delivery of biologics. *FASEB J* 36(3):e22208.

34. Stanimirovic DB, Sandhu JK, & Costain WJ (2018) Emerging Technologies for Delivery of Biotherapeutics and Gene Therapy Across the Blood-Brain Barrier. *BioDrugs* 32(6):547-559.

35. Ribecco-Lutkiewicz M*, et al.* (2018) A novel human induced pluripotent stem cell blood-brain barrier model: Applicability to study antibody-triggered receptor-mediated transcytosis. *Sci Rep* 8(1):1873.

36. Perchiacca JM, Ladiwala AR, Bhattacharya M, & Tessier PM (2012) Structure-based design of conformation- and sequence-specific antibodies against amyloid beta. *Proc Natl Acad Sci U S A* 109(1):84-89.

37. Abskharon R*, et al.* (2019) Structural evidence for the critical role of the prion protein hydrophobic region in forming an infectious prion. *PLoS Pathog* 15(12):e1008139.

38. Abskharon R*, et al.* (2020) Crystal structure of a conformational antibody that binds tau oligomers and inhibits pathological seeding by extracts from donors with Alzheimer's disease. *J Biol Chem* 295(31):10662-10676.

39. Desta IT, Porter KA, Xia B, Kozakov D, & Vajda S (2020) Performance and Its Limits in Rigid Body Protein-Protein Docking. *Structure* 28(9):1071-1081 e1073.

40. Rodriguez Camargo DC*, et al.* (2021) Proliferation of Tau 304-380 Fragment Aggregates through Autocatalytic Secondary Nucleation. *ACS Chem Neurosci* 12(23):4406-4415.

41. Lasagna-Reeves CA*, et al.* (2011) Tau oligomers impair memory and induce synaptic and mitochondrial dysfunction in wild-type mice. *Mol Neurodegener* 6:39.

42. Lasagna-Reeves CA*, et al.* (2012) Alzheimer brain-derived tau oligomers propagate pathology from endogenous tau. *Sci Rep* 2:700.

43. Li T*, et al.* (2012) Cell-penetrating anti-GFAP VHH and corresponding fluorescent fusion protein VHH-GFP spontaneously cross the blood-brain barrier and specifically recognize astrocytes: application to brain imaging. *FASEB J* 26(10):3969-3979.

44. Abskharon RN*, et al.* (2014) Probing the N-terminal beta-sheet conversion in the crystal structure of the human prion protein bound to a nanobody. *J Am Chem Soc* 136(3):937-944.

45. Schmidt M*, et al.* (2019) Cryo-EM structure of a transthyretin-derived amyloid fibril from a patient with hereditary ATTR amyloidosis. *Nat Commun* 10(1):5008.

46. Sheff J*, et al.* (2021) Defining the epitope of a blood-brain barrier crossing single domain antibody specific for the type 1 insulin-like growth factor receptor. *Sci Rep* 11(1):4284.

47. Wessel D & Flugge UI (1984) A method for the quantitative recovery of protein in dilute solution in the presence of detergents and lipids. *Anal Biochem* 138(1):141-143.

48. Hua CK*, et al.* (2017) Computationally-driven identification of antibody epitopes. *Elife* 6.

49. Pantazes RJ & Maranas CD (2010) OptCDR: a general computational method for the design of antibody complementarity determining regions for targeted epitope binding. *Protein Eng Des Sel* 23(11):849-858.

50. Tiller KE & Tessier PM (2015) Advances in Antibody Design. *Annu Rev Biomed Eng* 17:191-216.

51. de Marco A (2020) Recombinant expression of nanobodies and nanobody-derived immunoreagents. *Protein Expr Purif* 172:105645.

52. Ackaert C*, et al.* (2021) Immunogenicity Risk Profile of Nanobodies. *Front Immunol* 12:632687.

53. Wrapp D*, et al.* (2020) Structural Basis for Potent Neutralization of Betacoronaviruses by Single-Domain Camelid Antibodies. *Cell*.

54. Mudher A*, et al.* (2017) What is the evidence that tau pathology spreads through prion-like propagation? *Acta Neuropathol Commun* 5(1):99.

55. Clavaguera F*, et al.* (2009) Transmission and spreading of tauopathy in transgenic mouse brain. *Nat Cell Biol* 11(7):909-913.

56. Brier MR*, et al.* (2016) Tau and Abeta imaging, CSF measures, and cognition in Alzheimer's disease. *Sci Transl Med* 8(338):338ra366.

57. Jackson SJ*, et al.* (2016) Short Fibrils Constitute the Major Species of Seed-Competent Tau in the Brains of Mice Transgenic for Human P301S Tau. *J Neurosci* 36(3):762-772.

58. Cardenas-Aguayo Mdel C, Gomez-Virgilio L, DeRosa S, & Meraz-Rios MA (2014) The role of tau oligomers in the onset of Alzheimer's disease neuropathology. *ACS Chem Neurosci* 5(12):1178-1191.

59. Shi Y*, et al.* (2021) Structure-based classification of tauopathies. *Nature* 598(7880):359-363.

60. Kabsch W (2010) Xds. *Acta Crystallogr D Biol Crystallogr* 66(Pt 2):125-132.

61. McCoy AJ*, et al.* (2007) Phaser crystallographic software. *J Appl Crystallogr* 40(Pt 4):658-674.

62. Adams PD*, et al.* (2010) PHENIX: a comprehensive Python-based system for macromolecular structure solution. *Acta Crystallogr D Biol Crystallogr* 66(Pt 2):213-221.

63. Emsley P, Lohkamp B, Scott WG, & Cowtan K (2010) Features and development of Coot. *Acta Crystallogr D Biol Crystallogr* 66(Pt 4):486-501.

64. Kaufman SK, Del Tredici K, Thomas TL, Braak H, & Diamond MI (2018) Tau seeding activity begins in the transentorhinal/entorhinal regions and anticipates phospho-tau pathology in Alzheimer's disease and PART. *Acta Neuropathol* 136(1):57-67.

65. Sanders DW*, et al.* (2014) Distinct tau prion strains propagate in cells and mice and define different tauopathies. *Neuron* 82(6):1271-1288.

66. Schneider CA, Rasband WS, & Eliceiri KW (2012) NIH Image to ImageJ: 25 years of image analysis. *Nat Methods* 9(7):671-675.

67. Murray KA*, et al.* (2022) De novo designed protein inhibitors of amyloid aggregation and seeding. *Proc Natl Acad Sci U S A* 119(34):e2206240119.

**SI APPENDIX**

**Supplementary Table 1. Sequences of first generation nanobodies.**

| Name | Sequence |
|---|---|
| **W3** | QVQLQESGGGLVQPGGSLRLSCAASGRTFSSYNMGWFRQAPGKGREFVASITSS GDKSDYTDSVKGRFTISRDNAKNTMYLQMNNLKPEDTATYYCARGGG**DVWIINKK LK**GGGTQVTVSS |
| **WIW** | QVQLQESGGGLVQPGGSLRLSCAASGRTFSSYNMGWFRQAPGKGREFVASITSS GDKSDYTDSVKGRFTISRDNAKNTMYLQMNNLKPEDTATYYCARGGG**SVWIWYE** GGGTQVTVSS |
| **VDW** | QVQLQESGGGLVQPGGSLRLSCAASGRTFSSYNMGWFRQAPGKGREFVASITSS GDKSDYTDSVKGRFTISRDNAKNTMYLQMNNLKPEDTATYYCARG**SVWIWYEPV DWSE**GTQVTVSS |

**CDR3 is bolded.**

**Supplementary Table 2. Data collection and refinement statistics.**

| Data collection | WIW nanobody inhibitor |
|---|---|
| Wavelength | |
| Resolution range | 55.36 -1.40 (1.45 - 1.40) |
| Space group | I 4 |
| Unit cell | 78.29 78.29 38.22 90 90 90 |
| Total reflections | 63606 (6249) |
| Unique reflections | 22608 (2226) |
| Multiplicity | 2.8 (2.8) |
| Completeness (%) | 98.48 (98.50) |
| Mean I/sigma(I) | 5.3 (1.9) |
| Wilson B-factor | 17.04 |
| R-merge | 0.131 (0.440) |
| R-meas | 0.161 (0.543) |
| CC1/2 | 96.4 (81.0) |
| Reflections used in refinement | 22608 (2236) |
| Reflections used for R-free | 2268 (231) |
| R-work | 0.188 (0.287) |
| R-free | 0.216 (0.289) |
| Number of non-hydrogen atoms | 1085 |
| macromolecules | 970 |
| ligands | 6 |
| solvent | 109 |
| Protein residues | 124 |

| | |
|---|---|
| RMS(bonds) | 0.013 |
| RMS(angles) | 1.75 |
| Ramachandran favored (%) | 90.2 |
| Ramachandran allowed (%) | 9.8 |
| Ramachandran outliers (%) | 0.0 |
| Rotamer outliers (%) | 0 |
| Clashscore | 0 |
| Average B-factor | 23.0 |
| macromolecules | 22.1 |
| ligands | 35.1 |
| solvent | 31.0 |

**Supplementary Table 3. Tauopathies brain patient samples used for seeding experiments.**

| Number | Patient ID | Gender | Age at death | Clinical | Brain extract region | Etiology | Braak Stage |
|---|---|---|---|---|---|---|---|
| **1** | AD1 F | F | 78 | AD | right frontal | **AD** | **VI** |
| **2** | AD1 O | F | 78 | AD | right occipital | **AD** | **VI** |
| **3** | AD1 HIP | F | 78 | AD | left hippocampus | **AD** | **VI** |
| **4** | AD2 | M | 71 | AD | left frontal | **AD** | **VI** |
| **5** | AD3 | M | 68 | AD | left middle frontal gyrus, posterior | **AD** | **VI** |
| **6** | AD4 | F | 58 | CBS/AD | left inferior temporal gyrus | **AD** | **VI** |
| **7** | AD5 | F | 69 | AD | left inferior temporal gyrus | **AD** | **VI** |
| **8** | AD6 | F | 65 | AD | left inferior temporal gyrus | **AD** | **VI** |
| **9** | AD7 | M | 70 | AD | left inferior temporal gyrus | **AD** | **VI** |
| **10** | AD8 | M | 72 | AD | temporal gyrus | **AD** | **VI** |

| | | | | | | | |
|---|---|---|---|---|---|---|---|
| **11** | AD9 | M | 66 | AD | left inferior temporal gyrus, posterior | **AD** | **VI** |
| **12** | AD10 | F | 64 | AD | left inferior temporal gyrus, posterior | **AD** | **VI** |
| **13** | PSP1 | F | 71 | PSPS | right lateral orbitofrontal cortex | **PSP** | |
| **14** | PSP2 | M | 70 | nfvPPA | left angular gyrus | **PSP** | **II** |

**Supplementary Table 4. Sequences of second generation nanobodies.**

| Name | Sequence |
|---|---|
| **W3** | QVQLQESGGGLVQPGGSLRLSCAASGFTVSNSRMYWVRQAPGKGLEWVSSIR PSGEVIYATDSVKGRFIISRDNAKNTLHLQMNSLKPEDTARYYCARGGG**DVWIINK KLK**GGGTQVTVSS |
| **M4** | QVQLQESGGGLVQPGGSLRLSCAASGFTVSNSRMYWVRQAPGKGLEWVSSIR PSGEVIYATDSVKGRFIISRDNAKNTLHLQMNSLKPEDTARYYCARGGG**DVQMIN KKLK**GGGTQVTVSS |
| **R9** | QVQLQESGGGLVQPGGSLRLSCAASGFTVSNSRMYWVRQAPGKGLEWVSSIR PSGEVIYATDSVKGRFIISRDNAKNTLHLQMNSLKPEDTARYYCARGGG**DVQIINK KRK**GGGTQVTVSS |
| **QIINK** | QVQLQESGGGLVQPGGSLRLSCAASGFTVSNSRMYWVRQAPGKGLEWVSSIR PSGEVIYATDSVKGRFIISRDNAKNTLHLQMNSLKPEDTARYYCARGGG**KVQIINK KLD**GGGTQVTVSS |
| **WIW** | QVQLQVSGGGLVQPGGSLRLSCAASGFTVSNSRMYWVRQAPGKGLEWVSSIR PSGEVIYATDSVKGRFIISRDNAKNTLHLQMNSLKPEDTARYYCARGGG**SVWIWY E**GGGTQVTVSS |
| **SV** | QVQLQVSGGGLVQPGGSLRLSCAASGFTVSNSRMYWVRQAPGKGLEWVSSIR PSGEVIYATDSVKGRFIISRDNAKNTLHLQMNSLKPEDTARYYCARGGG**SVQIVY K**GGGTQVTVSS |
| **Non-cognate** | QVQLQVSGGGLVQPGGSLRLSCAASGFTVSNSRMYWVRQAPGKGLEWVSSIR PSGEVIYATDSVKGRFIISRDNAKNTLHLQMNSLKPEDTARYYCAR**ERPSGVRGQ** GTQVTVSS |
| **IR5-WIW** | QVQLQESGGGLVQAGGSLRLSCAASGRTIDNYAMAWSRQAPGKDREFVATIDW GDGGARYANSVKGRFTISRDNAKGTMYLQMNNLEPEDTAVYSCAMARQSRVNL |

| | |
|---|---|
| | DVARYDYWGQGTQVTVSSGSSSSGSSSSGSSSSQVQLQESGGGLVQPGGSLR<br>LSCAASGFTVSNSRMYWVRQAPGKGLEWVSSIRPSGEVIYATDSVKGRFIISRDN<br>AKNTLHLQMNSLKPEDTARYYCARGGG**SVWIWYE**GQGTQVTVSS |

**CDR3 is bolded.**

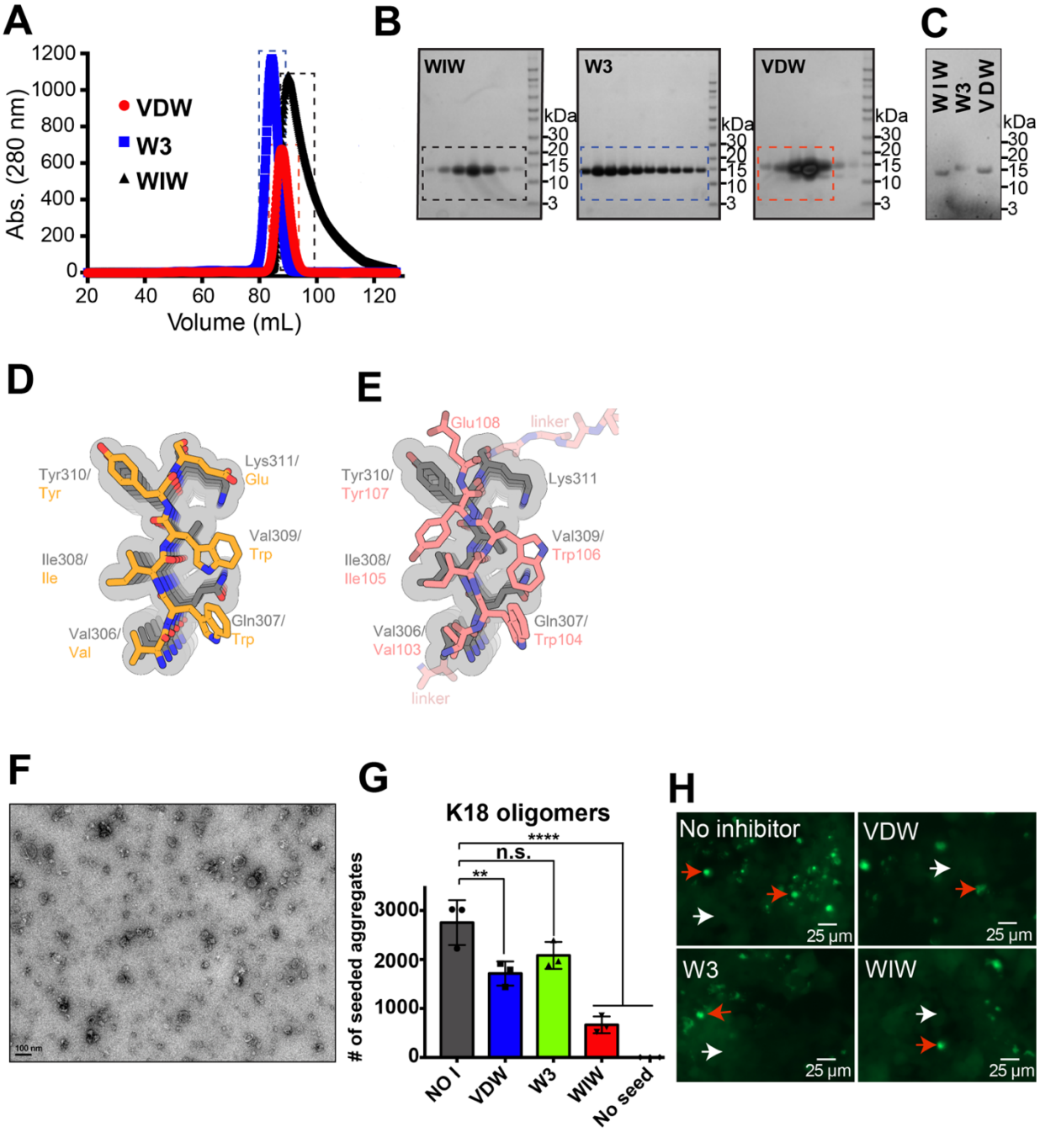


**Supplementary Figure 1. Design, expression and purification of the first generation of anti-tau seeding nanobody inhibitors. (A)** SEC purification of VDW, W3 and WIW nanobodies show a prominent species. **(B)** SDS/PAGE analysis of VDW, W3 and WIW nanobodies show ~ 15 kDa prominent peak after SEC purification using a HiLoad 16/600 Superdex 75 pg column.

The SDS/PAGE gel was stained with Coomassie blue. Nanobody fractions in the dashed lines were pooled for use. **(C)** Western blot analysis of VDW, W3 and WIW nanobodies probed with HisProbe-HRP antibody. **(D)** The original VWIWYE inhibitor peptide (orange) was intended to adopt a beta-sheet conformation and make backbone hydrogen bonds to tau segment 306-VQIVYK-311 of PHF (gray) (7nrv) (12). Here, the tau-inhibitor design is viewed along the direction of the fibril axis. Val, Ile, and Tyr side chains of the inhibitor were designed to lend stability through hydrophobic stacks with V306, I308, and Y310. A glutamate side chain was designed to lend electrostatic complementarity by stacking on Lys311 to, and two tryptophan residues were designed to block addition of tau molecules to the fibril tip. **(E)** Manual docking of the WIW nanobody crystal structure on tau shows how closely experiment matched the design. Remarkably, the nanobody crystal structure (pink) revealed that the inhibitor sequence VWIWYE inserted in the CDR3 loop did indeed adopt a beta strand conformation roughly compatible with our design concept. The inhibitor insert 103-VQIVYE-108 is shown here manually docked on the tau PHF structure (gray). Although the resemblance is evident, we note important deviations. For example, E108 adopts a conformation that prohibits electrostatic complementation with tau Lys311. Further engineering of the linker might allow this ion bridge to form. **(F)** Negative stain electron micrograph of recombinant tau-K18 oligomers. Scale bar 100 nm. **(G)** Quantification of the inhibitory effect of VDW, W3 and WIW nanobodies on inhibition of seeding by recombinant tau-K18 oligomers, measured in HEK293 biosensor cells. The inhibitor concentration of all nanobodies was 10 μM on the biosensor cells. The experiment was performed in technical triplicate. Statistical analysis was performed using one-way ANOVA followed by a Tukey's multiple comparison test (ns, $p > 0.05$; *, $p \leq 0.05$; **, $p \leq 0.01$; ***, $p \leq 0.001$; ****, $p \leq 0.0001$) in GraphPad Prism. **(H)** Representative images of seeding and inhibition by VDW, W3 and WIW nanobodies. Representative cells that contain aggregates are marked by red arrows, and cells without by white arrows.

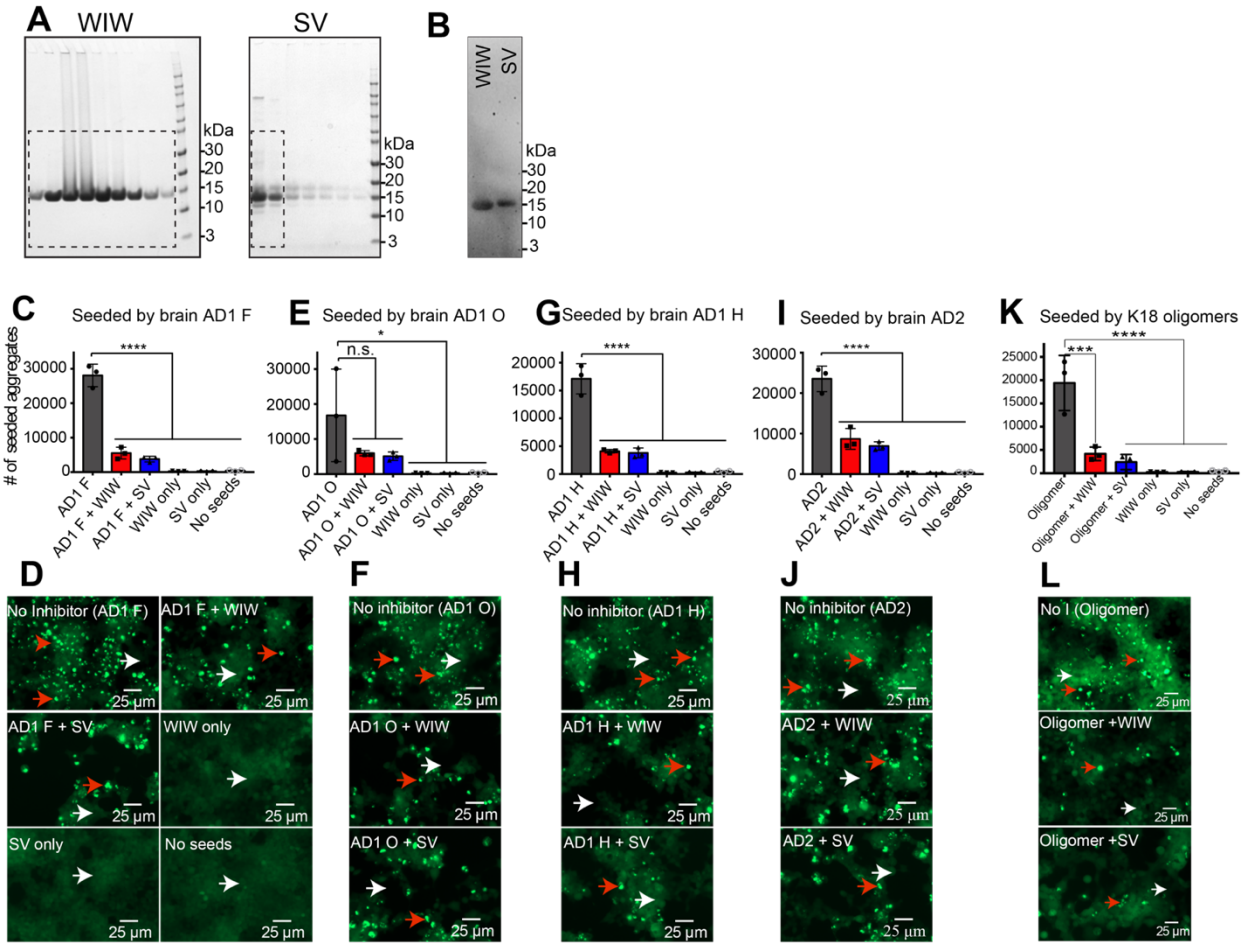


**Supplementary Figure 2. Inhibition of seeding by AD-derived brain extracts and K18 oligomers using the second generation of WIW and SV capping nanobody inhibitors. (A)** SDS/PAGE analysis of WIW and SV nanobodies show ~ 15 kDa after Ni-NTA purification. The SDS/PAGE gel was stained with Coomassie blue. Nanobody fractions in the dashed lines were pooled for use. **(B)** Western blot analysis of WIW and SV nanobodies probed with HisProbe-HRP antibody. **(C-J)** Quantification and representative images of the inhibitory effect of WIW and SV nanobody inhibitors on inhibition of seeding by brain extracts from AD brain tissue measured in HEK293 biosensor cells expressing YFP-tagged tau-K18. As control experiment, individual WIW and SV nanobodies show no seeding in biosensor cells. The inhibitor

concentration of all nanobodies was 10 μM on the biosensor cells. The experiment was performed in technical triplicate. Statistical analysis was performed using one-way ANOVA followed by a Tukey's multiple comparison test (ns, $p > 0.05$; *, $p \leq 0.05$; **, $p \leq 0.01$; ***, $p \leq 0.001$; ****, $p \leq 0.0001$) in GraphPad Prism. Representative cells containing aggregates are marked by red arrows, and cells without by white arrows. **(C & D)** AD1 F (Frontal lobe). **(E & F)** AD1 O (Occipital lobe). **(G & H)** AD1 H (Hippocampus). **(I & J)** AD2. **(K & L)** Quantification and representative images of the inhibitory effect of WIW and SV nanobody inhibitors on inhibition of seeding by K18 oligomers measured in HEK293 biosensor cells expressing YFP-tagged tau-K18.

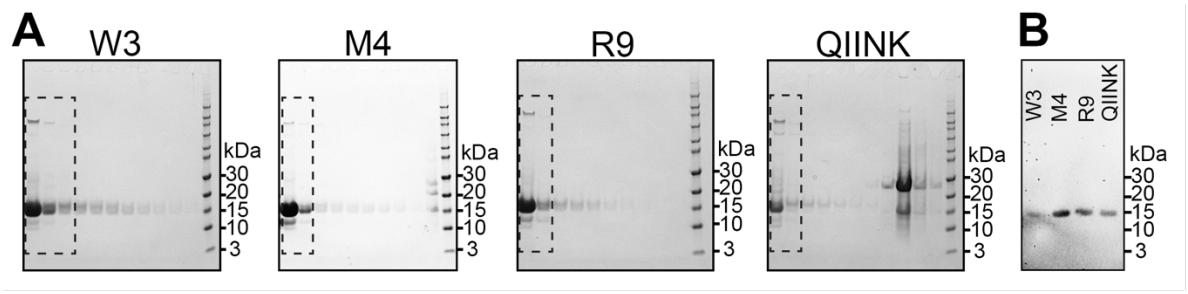
A
W3
M4
R9
QIINK
kDa
30
20
15
10
3
B
W3
M4
R9
QIINK
kDa
30
20
15
10
3

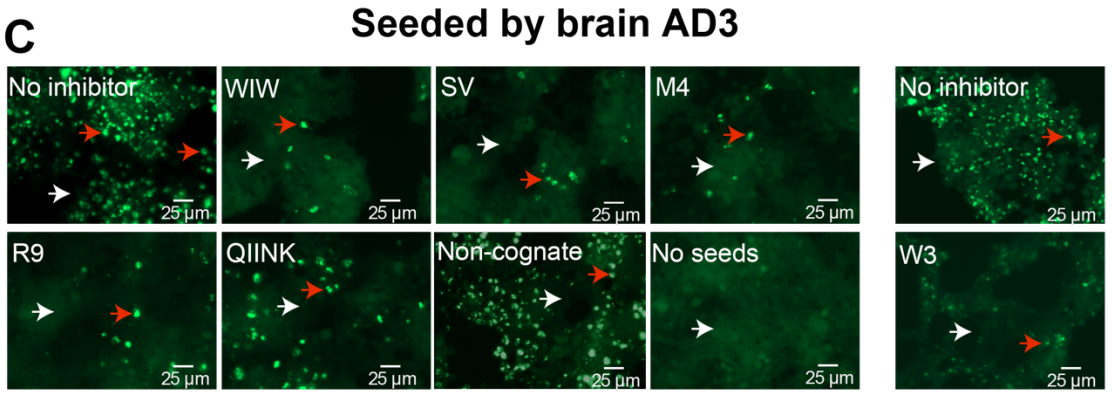
C
Seeded by brain AD3
No inhibitor
WIW
SV
M4
No inhibitor
R9
QIINK
Non-cognate
No seeds
W3
25 µm

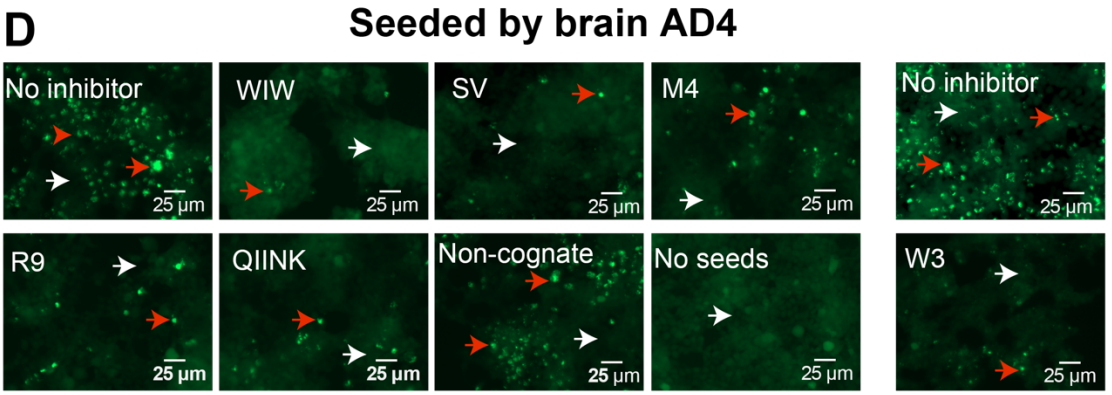
D
Seeded by brain AD4
No inhibitor
WIW
SV
M4
No inhibitor
R9
QIINK
Non-cognate
No seeds
W3
25 µm

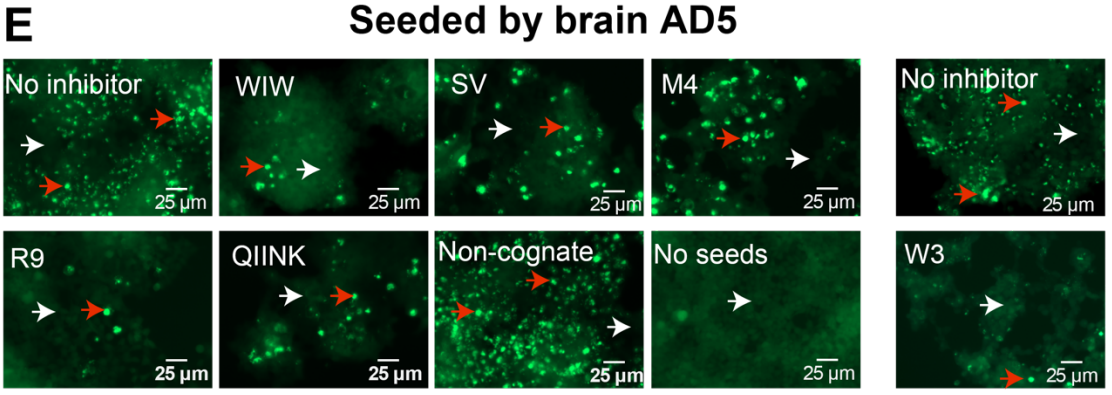
E
Seeded by brain AD5
No inhibitor
WIW
SV
M4
No inhibitor
R9
QIINK
Non-cognate
No seeds
W3
25 µm

**Supplementary Figure 3. Inhibition of seeding by AD-derived brain extracts using the second generation of WIW, W3, SV, M4, R9, and QIINK capping nanobody inhibitors. (A)** Purification of the W3, M4, R9 and QIINK nanobodies after Ni-NTA column. Nanobody fractions in the dashed lines were pooled for use. **(B)** Western blot analysis of the purified W3, M4, R9 and QIINK nanobodies probed with anti-His tag antibody. **(C)** Representative images of seeding by AD3 and inhibition in HEK293 biosensor cells expressing YFP-tagged tau-K18. **(D)** Representative images of seeding and inhibition by AD4 and inhibition in HEK293 biosensor cells expressing YFP-tagged tau-K18. **(E)** Representative images of seeding and inhibition by AD5 and inhibition in HEK293 biosensor cells. Representative cells containing aggregates are marked by red arrows, and cells without by white arrows.

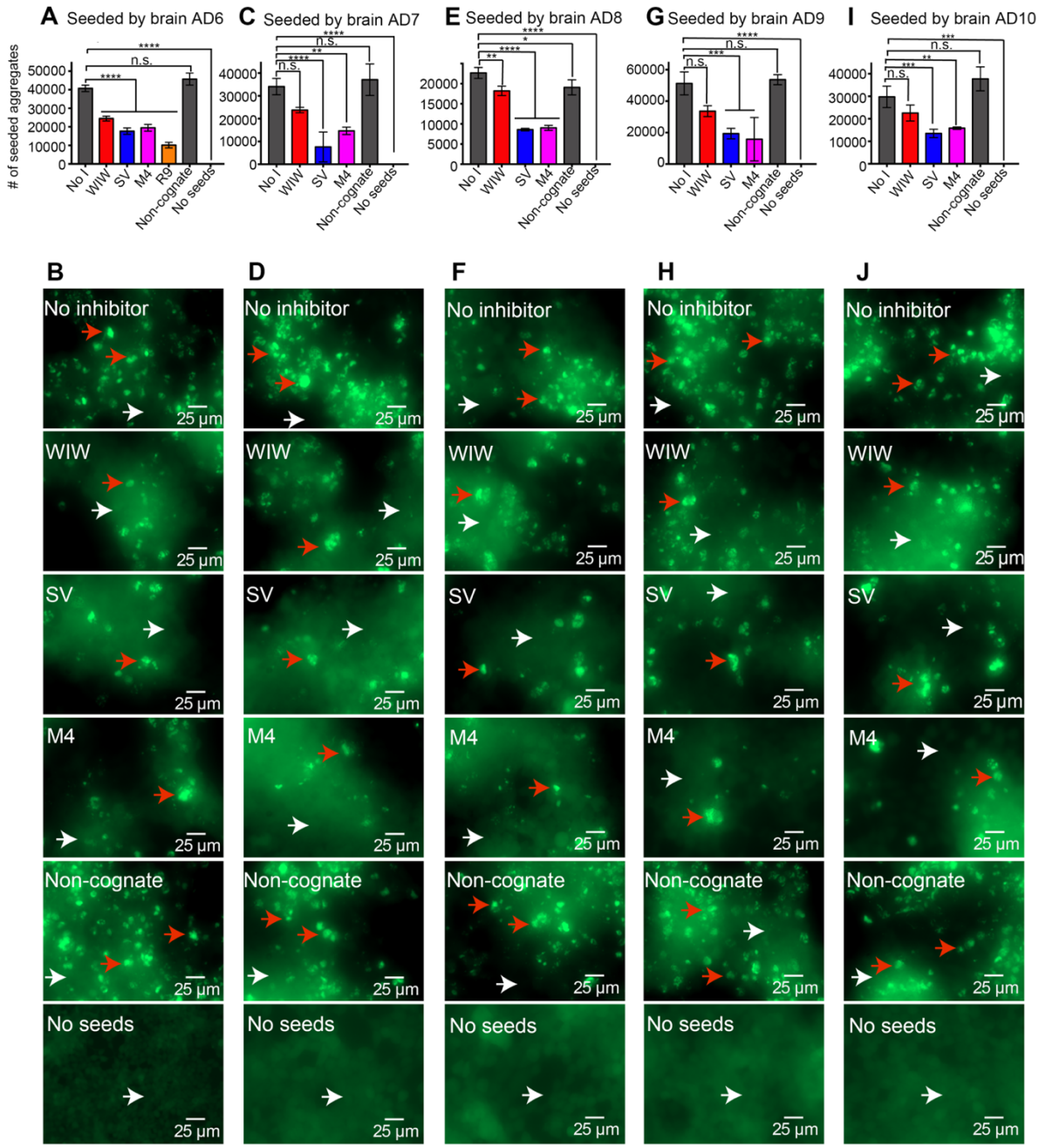


**Supplementary Figure 4. Capping nanobodies inhibit the seeding of tau aggregation by autopsied brain extracts from human AD brain patients. (A-J)** Quantification and representative images of the inhibitory effect of designed nanobody inhibitors on inhibition of seeding by brain extracts from AD brain tissue measured in HEK293 biosensor cells expressing YFP-tagged tau-K18. The inhibitor concentration of all nanobodies was 10 µM on the biosensor

cells. The experiment was performed in technical triplicate. Statistical analysis was performed using one-way ANOVA followed by a Tukey's multiple comparison test (ns, $p > 0.05$; *, $p \leq 0.05$; **, $p \leq 0.01$; ***, $p \leq 0.001$; ****, $p \leq 0.0001$) in GraphPad Prism. Representative cells containing aggregates are marked by red arrows, and cells without by white arrows. **(A & B)** AD6. **(C & D)** AD7. **(E & F)** AD8. **(G & H)** AD9. **(I & J)** AD10.

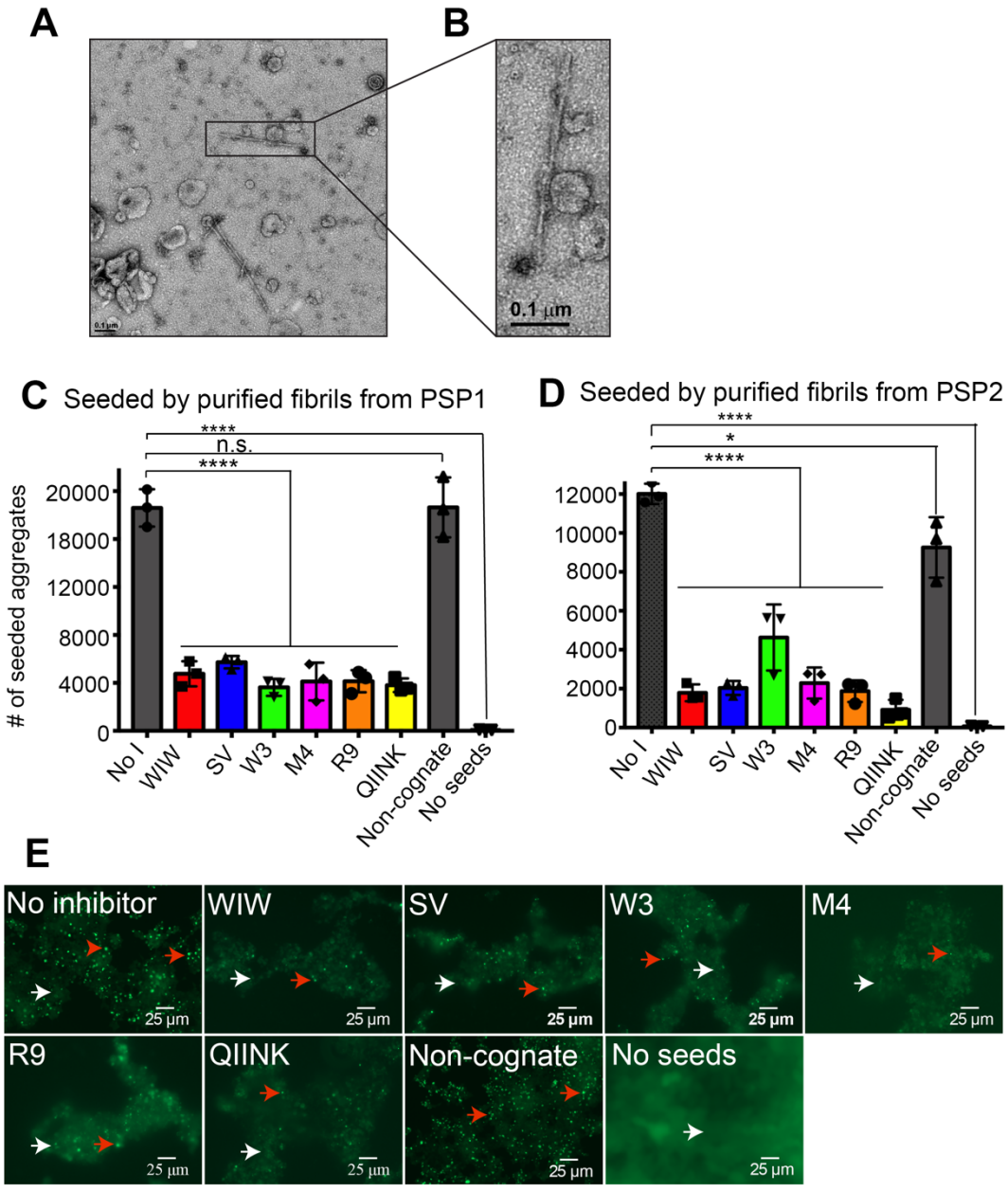


**Supplementary Figure 5. Capping nanobodies inhibit the seeding of human brain extracts from two donors with progressive supranuclear palsy (PSP). (A)** EM image of PSP fibrils from brain donor extracts with PSP pathology (PSP1). **(B)** Zoom view of PSP fibrils shows a twisted filaments morphology. **(C-D)** Quantification of the inhibitory effect of WIW, SV, W3, M4, R9, QIINK and non-cognate nanobodies on inhibition of seeding by brain extracts from two donors with PSP pathology. The inhibitor concentration of all nanobodies was 10 µM on the

biosensor cells. The experiment was performed in technical triplicate. Statistical analysis was performed using one-way ANOVA followed by a Tukey's multiple comparison test (ns, $p > 0.05$; *, $p \leq 0.05$; **, $p \leq 0.01$; ***, $p \leq 0.001$; ****, $p \leq 0.0001$) in GraphPad Prism. **(C)** PSP1. **(D)** PSP2. **(E)** Representative images of seeding and inhibition by PSP1 in HEK293 biosensor cells expressing YFP-tagged tau-K18. Representative cells containing aggregates are marked by red arrows, and cells without by white arrows.

A

QVQLQESGGGLVQAGGSLRLSCAASGRTIDNYAMAWSRQAPGKDREFVATIDWGDGGARYANSVK
GRFTISRDNAKGTMYLQMNNLEPEDTAVYSCAMARQSRVNLDVARYDYWGQGTQVTVSSGSSSSG
SSSSGSSSSQVQLQESGGGLVQPGGSLRLSCAASGFTVSNSRMYWVRQAPGKGLEWVSSIRPSG
EVIYATDSVKGRFIISRDNAKNTLHLQMNSLKPEDTARYYCARGGGSVWIWYEGQGTQVTVSS

B

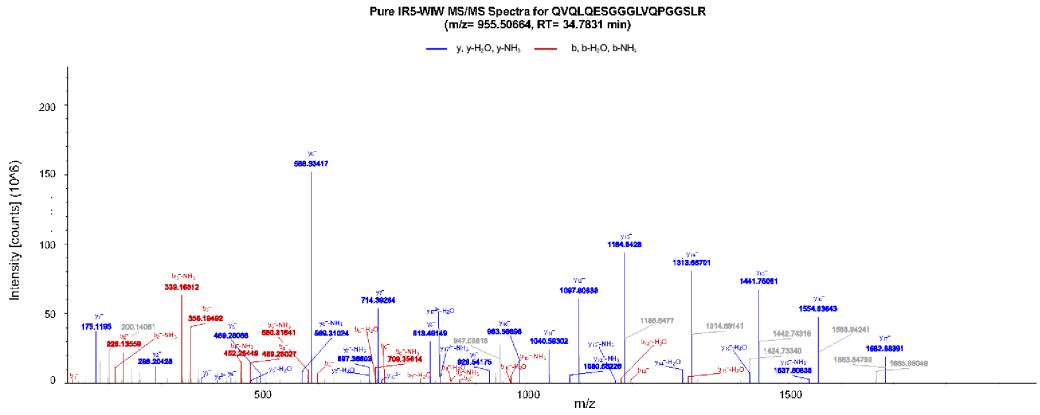


C

Standard Samples for IR5-WIW

| Concentration (ug/g) | Peak Area | Retention Time (min) | Mass Error (ppm) |
|---|---|---|---|
| 0 | 0.00E+00 | 0 | 0 |
| 1 | 3.43E+04 | 34.56 | +3.2 |
| 10 | 6.01E+05 | 34.62 | -3.9 |
| 20 | 1.48E+06 | 33.97 | +1.0 |
| 50 | 4.04E+06 | 34.12 | -0.9 |

D

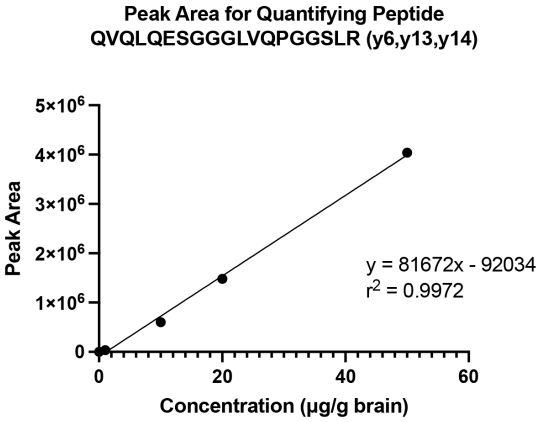


E

Unknown Samples for IR5-WIW

| Mouse | Peak Area | Retention Time (min) | Mass Error (ppm) | Concentration (ug/g) | %Efficiency |
|---|---|---|---|---|---|
| 1 | 5.73E+05 | 33.78 | -1.4 | 8.13 | 1.36 |
| 2 | 2.57E+05 | 33.81 | -1.3 | 4.27 | 0.71 |
| 3 | 2.59E+05 | 33.83 | -1.5 | 4.29 | 0.72 |

**Supplementary Figure 6. Detection of bispecific WIW nanobody in mouse brain. (A)** Sequence of bispecific WIW. The WIW and IR5 nanobody domain sequences are colored green and red, respectively. The WIW nanobody and IR5 Nanobody fragments are connected by a flexible linker with sequence (Gly4Ser)3, which is colored black. **B)** Data-dependent MS2 spectra of QVQLQESGGGLVQPGGSLR from pure IR5-WIW nanobody sample. **C)** Standard samples were prepared by spiking naïve brain tissue with nanobody at concentrations of 0, 1, 10, 20, and 50 µg/g brain. Table of peak areas for peptide QVQLQESGGGLVQPGGSLR measured in standard samples. **D)** Quantification curve for measured peak areas in standard samples. **E)** Concentration of nanobody in unknown samples calculated using the quantification curve in **D**.

A

QVQLQVSGGGLVQPGGSLRLSCAASGFTVSNSRMYWVRQAPGKGLEWVSSIRPSG
EVIYATDSVKGRFIISRDNAKNTLHLQMNSLKPEDTARYYCARGGGSVWIWYEGQGTQVTVSS

B

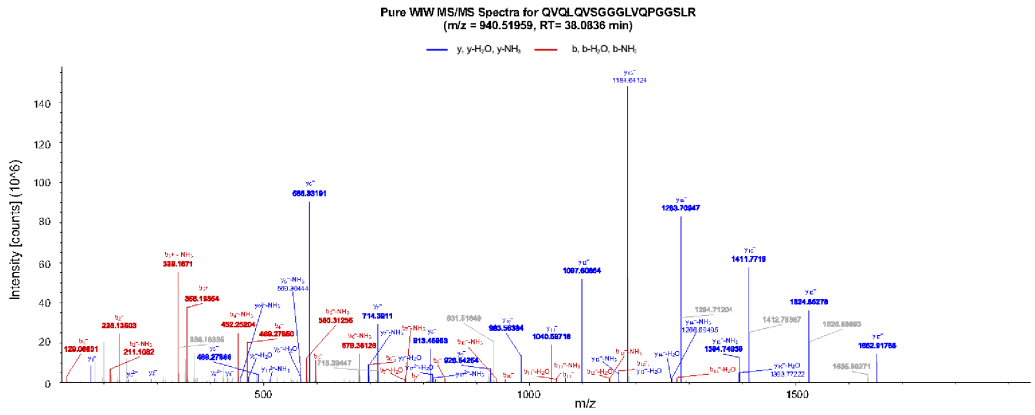


C

Standard Samples for WIW

| Concentration (ug/g) | Peak Area | Retention Time (min) | Mass Error (ppm) |
|---|---|---|---|
| 0 | 1.80E+03 | 38.10 | +2.8 |
| 1 | 9.32E+03 | 38.05 | +1.8 |
| 10 | 7.40E+06 | 38.02 | -1.0 |
| 30 | 2.98E+07 | 38.11 | +0.4 |
| 100 | 9.70E+07 | 38.10 | +8.9 |

D

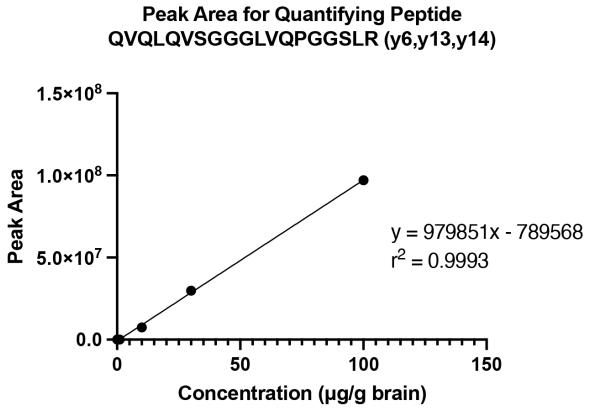


E

Unknown Samples for WIW

| Mouse | Peak Area | Retention Time (min) | Mass Error (ppm) | Concentration (ug/g) | %Efficiency |
|---|---|---|---|---|---|
| 4 | 0.00E+00 | 0 | 0 | 0 | 0 |
| 5 | 0.00E+00 | 0 | 0 | 0 | 0 |
| 6 | 0.00E+00 | 0 | 0 | 0 | 0 |

**Supplementary Figure 7. Detection of second generation WIW nanobody in mouse brain.** **(A)** Sequence of WIW. **B)** Data-dependent MS2 spectra of QVQLQVSGGGLVQPGGSLR from pure WIW nanobody sample. **C)** Standard samples were prepared by spiking naïve brain tissue with nanobody at concentrations of 0, 1, 10, 30, and 100 µg/g brain. Table of peak areas for peptide QVQLQVSGGGLVQPGGSLR measured in standard samples. **D)** Quantification curve for measured peak areas in standard samples. **E)** Concentration of nanobody in unknown samples calculated using the quantification curve in **D**.

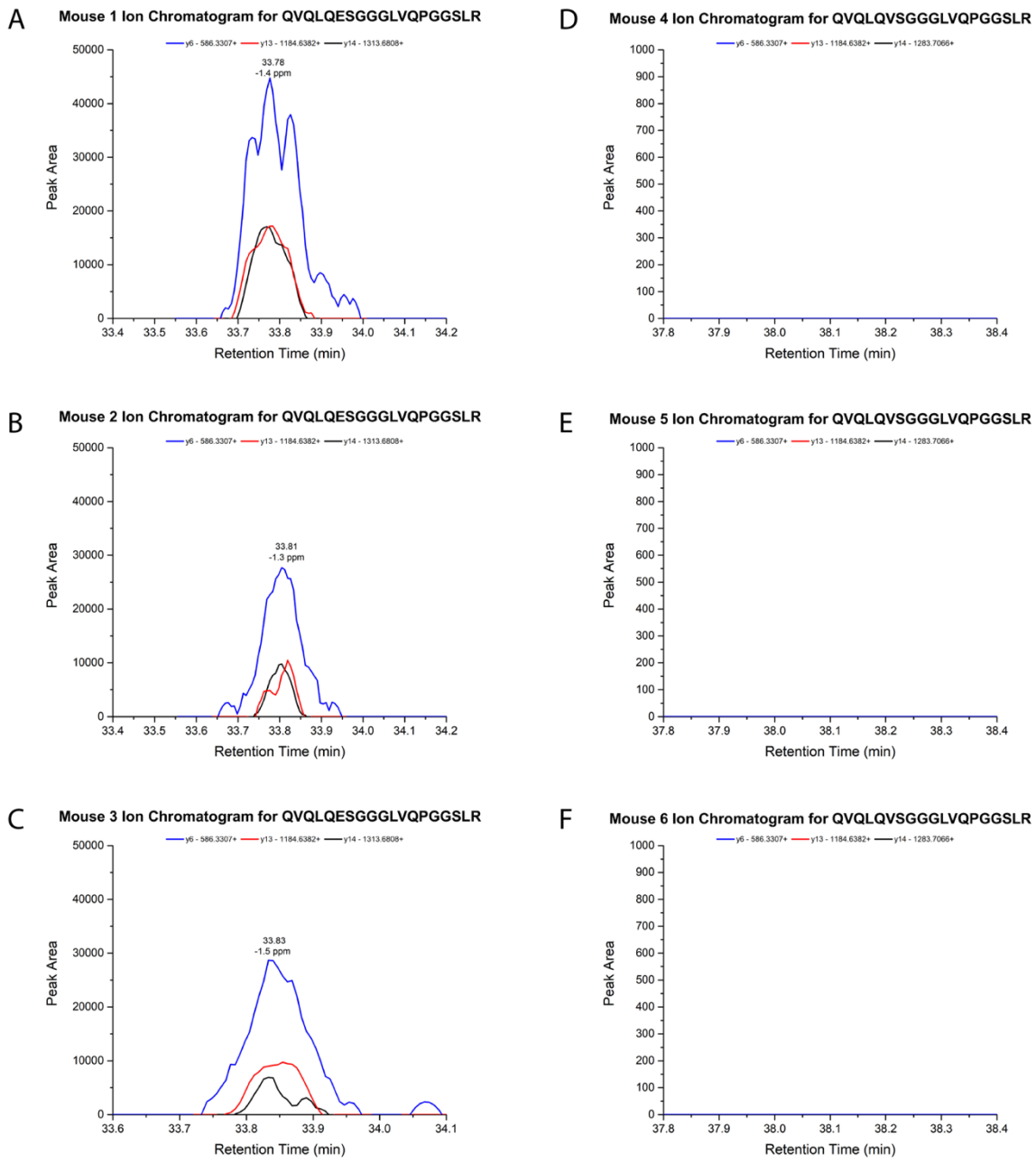


**Supplementary Figure 8. Ion chromatograms for detection of IR5-WIW and WIW nanobody peptides in mouse brain. (A-C)** Ion chromatogram for IR5-WIW nanobody peptide (QVQLQESGGGLVQPGGSLR) for Mouse 1-3. Peaks are labeled with retention times (min) and mass error (ppm). **(D-F)** Ion chromatogram for IR5-WIW nanobody peptide (QVQLQVSGGGLVQPGGSLR) for Mouse 4-6. Peaks are labeled with retention times (min) and mass error (ppm).

## SUPPLEMENTARY MATERIALS AND METHODS

### Trypsin Digestion for LC-MS/MS Analysis

Gel bands were washed by incubating in 50% acetonitrile/50%100 mM ammonium bicarbonate for 15 min, multiple times. Gel-embedded proteins were reduced with 10 mM TCEP (Sigma) for about one hour with shaking at 56 $^{o}$C, and then alkylated with 100 mM iodoacetamide (Sigma) in 100 mM ammonium bicarbonate at room temperature for 30 min in the dark. The excised bands were re-washed with 50% acetonitrile/50% 100 mM ammonium bicarbonate, as described above. Following washing, the gel bands were incubated in 100% acetonitrile for 10 min (room temperature); solvent was withdrawn and the gels were air-dried for 20 min. Next, the gel-embedded proteins were digested with 600 ng of modified trypsin in 60 µL of 100 mM ammonium bicarbonate at 37 $^{o}$C overnight. Peptides were extracted in 47.5% water/47.5% acetonitrile/5% formic acid.

Along with the live mouse samples, a series of standards were prepared in which IR5-WIW (concentrations of 0, 1, 10, 20 and 50 µg/g brain tissue) or WIW (concentrations of 0, 1, 10 and 30 µg/g brain tissue) were added to 100 mg nanobody-naïve mouse brain tissue. These samples were processed as described above, with the exception that 120 µL of non-concentrated brain homogenate was mixed with 40 µL of loading dye with β-mercaptoethanol and urea, and 40 µL of the brain homogenate/loading dye mixture was run in four wells of a NuPAGE™ 4 to 12%, Bis-Tris, 1.0 mm, 10-well gel. The final total protein concentration of all samples and standards was normalized using a Thermo Scientific Nanodrop 2000 to ensure no differences between CentriVap concentrated samples and non-concentrated samples.

In addition to the gel bands, pure nanobodies in solution (IR5-WIW and WIW) were each reduced with 10 mM TCEP (Sigma) for 1 hr with shaking at 56 $^{o}$C followed by alkylation with 40

mM iodoacetamide (Sigma) for 30 min at room temperature in the dark. Alkylation was quenched with 10 mM DTT (Sigma). Samples were each digested with 200 ng modified trypsin in 100 mM ammonium bicarbonate at 37 $^{o}$C overnight.

**LC-MS/MS and Parallel Reaction Monitoring (PRM) Analyses**

Dried peptides were reconstituted in 0.5% formic acid and desalted with C18 StageTips (68). The resulting peptides were dissolved in 1% acetonitrile with 0.1% formic acid. Digested peptides were separated on an EASY-Spray column (25 cm x 75 µM internal diameter, PepMAP RSLC C18, 2 µM, Thermo Scientific) connected to an UltiMate™ 3000 RSLCnano HPLC (Thermo Scientific) and eluted using a gradient of 3%-35% acetonitrile in 0.1% formic acid for 0-44 min and 95%-3% acetonitrile in 0.1% formic acid for 45-60 min at a flow rate of 300 nL/min.

Tandem mass spectra were collected for survey studies in a data-dependent matter with an Orbitrap Exploris 480 mass spectrometer (Thermo Scientific) interfaced to a nano-ESI source (Thermo Scientific). The RAW data was searched against nanobody sequences by ProteomeDiscoverer™ version 2.4 using Sequest HT. The precursor mass tolerance was ±10 ppm and fragment mass tolerances were ±0.02 *m/z*. Methionine oxidation was considered as a variable modification and cysteine carbamidomethylation was applied as a static modification. High confidence peptides were identified, some of which were employed in parallel monitoring reaction analyses.

Peptides QVQLQESGGGLVQPGGSLR (Charge = +2, *m/z*=955.5122, unique to IR5-WIW) and QVQLQVSGGGLVQPGGSLR (Charge = +2, m/z=940.52117, unique to WIW) were ultimately selected for quantification. Tandem mass spectra were collected from standard concentrations spiked into brain homogenates and from mouse brain samples using a targeted tandem MS (tMS2 otcid) method with the Orbitrap Exploris 480 mass spectrometer. PRM data were

analyzed using Skyline (v22.2.0.527) (69). Peptide settings allowed no missed cleavages for trypsin digestion ([KR|P]) and required a minimum of 8 and maximum of 25 amino acids, while excluding the 25 *N*-terminal amino acids. The MS/MS transition settings employed 0.02 *m/z*, and a method match tolerance of 0.02 *m/z*. The acquisition method under Full-Scan parameters was set to PRM with Orbitrap mass analyzer and with a resolving power of 60,000 at *m/z* 400. Ion chromatograms displayed in the Supplementary Methods were smoothed by a Savitzky-Golay transformation. Standard curves were plotted using the summed $y_6$, $y_{13}$, and $y_{14}$ (singly-charged) peak areas; *i.e., m/z* 586.3307, *m/z* 1184.6382, and *m/z* 1313.6808, respectively, for IR5-WIW and *m/z* 586.3307, *m/z* 1184.6382, and *m/z* 1283.7066, respectively, for WIW. Proteomic datasets submitted to the ProteomeXchange Consortium through the MassIVE repository are identified as PXD043069.

A consideration in calculating protein amounts based on the abundances of peptides with *N*-terminal Gln is that variable amounts of cyclization to pyro-glutamine could impact accuracy. Here, the calculations assumed a constant amount of glutamine cyclization for all samples and standards.

68. Ishihama Y, Rappsilber J, & Mann M (2006) Modular stop and go extraction tips with stacked disks for parallel and multidimensional Peptide fractionation in proteomics. J Proteome Res 5(4):988-994.

69. Pino LK, et al. (2020) The Skyline ecosystem: Informatics for quantitative mass spectrometry proteomics. Mass Spectrom Rev 39(3):229-244.

CHAPTER 4

# Structure-based discovery of small molecules that disaggregate tau fibrils in a mouse model of tauopathy

Hope Pan[1]*, Xinyi Cheng[1]*, Jeffrey Zhang[1]*, Ke Hou[1], Kapil Manglani[2,3], Cansheng Zhu[2,3], Marisa Mekkittikul[2,3], Tyler Halladay[1], Hilda Mirbaha[4], Gazmend Elezi[5], Romany Abskharon[1], Alexander Bombino[2,3], Christopher K. Williams[4,6], Harry V. Vinters[4,6], Julian P. Whitelegge[5], Gregory M. Cole[3,4], Sally A. Frautschy[3,4], David S. Eisenberg[1]**

[1]Department of Chemistry and Biochemistry, Department of Biological Chemistry, UCLA-DOE Institute, Molecular Biology Institute, UCLA, Los Angeles CA, 90095; [2]Geriatric Research Education and Clinical Center, Greater Los Angeles Veterans Affairs Healthcare System, West Los Angeles VA Medical Center, Los Angeles, CA, 90073; [4]Department of Pathology and Laboratory Medicine, David Geffen School of Medicine, UCLA, Los Angeles, CA 90095; [5]Pasarow Mass Spectrometry Laboratory, David Geffen School of Medicine, UCLA, Los Angeles, CA 90095; [6]Department of Neurology, David Geffen School of Medicine at UCLA, Los Angeles, CA, 90095

*These authors contributed equally

**To whom correspondence should be addressed: David S. Eisenberg: University of California-Los Angeles 611 Charles E Young Drive, Boyer 201, Los Angeles, CA 90095; david@mbi.ucla.edu; Tel. (310) 825-3754, Fax. (310) 206-3914

**Abstract**

Aggregation of the microtubule-binding protein tau is the histopathological hallmark of Alzheimer's disease (AD) and other neurodegenerative diseases, which are collectively known as tauopathies. Studies in AD patients have shown that tau aggregation is correlated with neuron loss, brain atrophy, and cognitive decline, so reversing tau aggregation is a potential therapeutic avenue for AD. In a previous study, we discovered CNS-11, a small molecule that disaggregates AD patient brain-derived tau fibrils *in vitro*. In this study, we discover two additional chemical analogs of CNS-11 that disaggregate AD patient brain-derived tau fibrils and prevent seeding in a tau aggregation cell culture model. We also demonstrate that eight weeks of treatment with either CNS-11 or its two analogs significantly reduces levels of insoluble tau in a mouse model of tauopathy. This study demonstrates the potential of using structure-based methods to discover small molecules that can disaggregate tau for AD and related tauopathies. (150 words)

**Introduction**

Alzheimer's disease (AD) is a slow and progressive form of dementia. AD is associated with accumulation of the proteins amyloid-β (Aβ) and tau as extracellular amyloid plaques and intracellular neurofibrillary tangles (NFTs), respectively. Amyloid plaques and NFTs have been hypothesized to cause neuron death, so targeting their formation has been one approach for designing therapeutics. For example, FDA approved drugs aducanumab and lecanemab are monoclonal antibodies that target Aβ and the formation of amyloid plaques(*1*, *2*). However, laboratory(*3*–*7*) and clinical(*8*–*11*) studies in AD patients have demonstrated that increased NFTs formed from tau, not plaques formed from Aβ, are correlated with neuron loss, brain

atrophy, and cognitive decline. Therefore, drugs targeting tau instead of Aβ could have greater potential in halting the progression of AD.

NFTs form when tau undergoes a conformational change from soluble monomer to insoluble amyloid fibril. In AD patients, tau deposition and NFT formation progresses in an orderly fashion, beginning in the entorhinal cortex, spreading to synaptically connected regions such as the hippocampus, and eventually moving to the neocortex(*12*, *13*). This pattern suggests that tau pathology spreads by “seeding”, or conversion of soluble tau to its insoluble form by existing tau fibrils. Multiple laboratory studies have demonstrated seeding among cultured cells(*14*–*17*) and in mice(*18*–*23*). When small quantities of preformed fibrils are transfected into tau-expressing cells, large amounts of soluble tau are rapidly recruited (“seeded”) into insoluble aggregates resembling NFTs(*16*). When transgenic mice expressing human tau are injected intracranially with preformed fibrils, tau inclusions develop in the injected hippocampus and eventually spread to the contralateral hippocampus(*20*, *21*). Drugs that could disaggregate insoluble tau fibrils and prevent them from seeding the formation of additional fibrils would have the potential to halt the progression of AD.

The small molecule EGCG, abundant in green tea, has long been known to disaggregate amyloid fibrils(*24*–*26*). However, EGCG has poor bioavailability, failing to penetrate the brain, and is readily modified in the body(*27*). In a recent study, to understand how EGCG can disaggregate stable fibrils, we used cryo-electron microscopy to determine the atomic structure of AD brain-extracted tau bound to EGCG(*28*). Using the EGCG binding position as a pharmacophore, we computationally screened thousands of drug-like compounds that have characteristics favoring BBB permeability (following the Lipinski rule of five, low polar surface area, etc.). With experimental validation, we discovered lead compound CNS-11, which

prevents seeding in a tau aggregation cell culture model and disaggregates AD patient brain-derived tau fibrils *in vitro*(*28*).

In this study, we screen four of chemical analogs of CNS-11 for their ability to disaggregate AD patient brain-derived tau fibrils *in vitro*. Additionally, to determine whether CNS-11 and its analogs can disaggregate tau *in vivo*, we assess their ability to reduce insoluble tau in a mouse model of tauopathy. Our work evaluates the potential of using structure-based methods to discover small molecules that can disaggregate tau for AD and related tauopathies.

## Results

### Discovery of CNS-11 as a tau disaggregator

In a recent study, we used cryo-electron microscopy to determine the atomic structure of AD brain-extracted tau bound to EGCG(*28*). Using the EGCG binding position as a pharmacophore, we computationally screened thousands of drug-like compounds that have characteristics favoring BBB permeability (following the Lipinski rule of five, low polar surface area, etc.) (**Figure 1A**). We experimentally screened 46 compounds in a tau aggregation cell culture model and identified 11 compounds that inhibit the seeding efficiency of AD brain extracts by at least 50% (**Figure 1B**). We selected four compounds for further characterization by quantitative electron microscopy (**Figure 1C-D**) and found that CNS-11 disaggregates AD patient brain-derived tau fibrils *in vitro* with an efficiency approaching EGCG (**Figure 1E**). In another recent study, we administered the lead compound, CNS-11, by tail vein injection to C57BL/6J mice and found that it crosses the blood-brain barrier(*29*).

### CNS-11 reduces levels of insoluble tau in PS19 mice without causing obvious toxicity

To determine whether CNS-11 can disaggregate tau fibrils *in vivo*, we sought to characterize its efficacy in a mouse model of tauopathy. The PS19 line of transgenic mice express human tau with the P301S mutation and develop hyperphosphorylated tau inclusions after six months of age(*30*). Young PS19 mice can be seeded by intracranial injection of tau fibrils to rapidly induce tau pathology and to ensure consistency in tau spreading among mice(*20*). We stereotaxically seeded 10 two-month-old PS19 mice with tau-K18+ pre-formed fibrils in the right hippocampus and the right frontal cortex, as previously described(*31*). In addition, we stereotaxically injected PBS in 4 wild-type, age-matched B6C3F1/J mice to serve as controls. Beginning four weeks after surgery, we administered CNS-11 at a dose of 1 mg per kg of body weight (mg/kg) by tail vein injection to n = 5 PS19 mice, and vehicle (1xPBS with 10% DMSO) to n = 5 PS19 mice, once a week for eight weeks (**Figure 2A**).

After eight weeks of treatment, we euthanized the mice by cardiac perfusion and collected their brain tissue for post-mortem analysis. We homogenized the right hippocampus in RIPA buffer, separated the homogenate into RIPA-soluble and RIPA-insoluble fractions, and performed Western blot analysis of the RIPA-soluble and RIPA-insoluble fractions. Seeded PS19 mice had significantly higher levels of soluble tau and insoluble tau compared to wild-type mice (**Figure 2B-D, Supplementary Figure 1**). Treatment of PS19 mice with CNS-11 did not significantly change levels of tau in the soluble fraction (**Figure 2B-C, Supplementary Figure 1**) but significantly reduced levels of tau in the insoluble fraction (**Figure 2B&D, Supplementary Figure 1**).

Additionally, we collected plasma and major organs, including heart, lung, kidney, liver, and spleen. We measured plasma AST levels to assess liver function. Treatment with CNS-11 did not significantly change plasma AST levels, indicating that it does not affect liver function (**Figure 2E**). We performed hematoxylin and eosin (H&E) staining on sections of the major

organs. We plan to observe the tissue sections for any morphological changes, necrosis, or other signs of toxicity (**Figure 2F**).

**Chemical analogs of CNS-11 also disaggregate tau fibrils from AD patients and prevent seeding in HEK293 biosensor cells**

In another recent study, we screened CNS-11 and ten chemical analogs for their ability to disaggregate α-synuclein fibrils extracted from post-mortem brain tissue of multiple system atrophy (MSA) patients. We discovered that CNS-11G disaggregates MSA patient brain-derived fibrils and prevents seeding in an α-synuclein aggregation cell culture model(*29*). Therefore, we sought to additionally screen four of these ten chemical analogs, CNS-11A, CNS-11B, CNS-11D, and CNS-11G, for their ability to disaggregate tau fibrils extracted from post-mortem brain tissue of AD patients (**Figure 3A**).

We extracted fibrils from post-mortem brain tissue of three AD patients (**Supplementary Table 1**). We incubated the AD brain-derived fibrils with vehicle (DMSO), EGCG, CNS-11, or one of the four chemical analogs of CNS-11. EGCG, CNS-11, CNS-11D, and CNS-11G consistently reduced the number of AD brain-extracted fibrils across three patient brain samples (**Figure 3B-C, Supplementary Figure 2**).

Next, we determined whether these chemical analogs could prevent seeding by AD tau fibrils in a tau aggregation cell model. HEK293T biosensor cells stably express YFP-fused tau-K18(*17*). When HEK293T biosensor cells are seeded by exogenous tau fibrils, endogenous YFP-fused tau-K18 aggregates and forms fluorescent, quantifiable puncta. We incubated AD brain-derived fibrils from AD1 with vehicle (DMSO), EGCG, CNS-11, or one of the four chemical analogs of CNS-11 and seeded biosensor cells with the mixtures. EGCG, CNS-11, CNS-11A, CNS-11D, and CNS-11G reduced seeding by AD brain-derived fibrils in tau biosensor cells (**Figure 3D**).

**CNS-11D crosses the blood-brain barrier more readily than CNS-11 and CNS-11G**

Because CNS-11D and CNS-11G showed promise as tau disaggregators, we next assessed their ability to cross the blood-brain barrier. We previously determined that CNS-11 and CNS-11G penetrate the brain(*29*). They were measured in brain tissue with a range of concentrations of 5.7 to 17.8 ng/g of brain for CNS-11 and 3.5 to 25.5 ng/g of brain for CNS-11g. Because CNS-11 and CNS-11G penetrate the brain, we predicted that CNS-11D would penetrate the brain as well. We administered CNS-11D by tail vein injection at a dose of 1 mg/kg to wild-type B6C3F1/J mice (n = 8 for each compound). One hour after dosing, we euthanized the mice by cardiac perfusion and collected brain and plasma samples. A liquid chromatographic–tandem mass spectrometric multiple reaction monitoring (LC-MS/MS-MRM) assay was used to detect and quantify the drug levels in each tissue sample. The sample extraction protocol for the plasma and brain was optimized with spiking experiments in which the authentic compounds were added to the plasma and brain from drug-naive mice.

One hour following administration, CNS-11D was measured in the plasma of treated wild-type mice with a range of concentrations of 6.3 to 15.0 ng/mL (**Supplementary Figure 3A**). CNS-11D was measured in brain tissue with a range of concentrations of 31.2 to 121.1 ng/g of brain (**Supplementary Figure 3B**). The amount of plasma collected from three mice treated with CNS-11D was an insufficient volume for analysis by LC-MS/MS-MRM. Plasma levels of CNS-11D were not significantly different from those measured for CNS-11 and CNS-11G, but brain levels of CNS-11D were significantly higher than those measured for CNS-11 and CNS-11G (**Supplementary Figure 3A-B**).

**CNS-11D and CNS-11G reduce levels of insoluble tau in PS19 mice**

To determine whether CNS-11G and CNS-11D can disaggregate tau fibrils *in vivo*, we sought to characterize their efficacy in the PS19 mouse model. We stereotaxically seeded 15 two-month-old PS19 mice with tau-K18+ pre-formed fibrils in the left hippocampus and the right hippocampus. Beginning two weeks after surgery, we administered CNS-11 at a dose of 1 mg/kg by tail vein injection to n = 5 mice, and vehicle (1xPBS with 10% DMSO) to n = 5 mice, once a week for eight weeks (**Figure 4A**).

After eight weeks of treatment, we euthanized the mice by cardiac perfusion and collected their brain tissue for post-mortem analysis. We homogenized the right hippocampus in RIPA buffer, separated the homogenate into RIPA-soluble and RIPA-insoluble fractions, and performed Western blot analysis of the RIPA-soluble and RIPA-insoluble fractions. Treatment of PS19 mice with either CNS-11D or CNS-11G did not significantly change levels of tau in the soluble fraction (**Figure 4B-C, Supplementary Figure 4**) but treatment with either CNS-11D or CNS-11G significantly reduced levels of tau in the insoluble fraction (**Figure 4B&D, Supplementary Figure 4**).

Additionally, we collected plasma and major organs, including heart, lung, kidney, liver, and spleen. We measured plasma AST levels to assess liver function. Treatment with either CNS-11D or CNS-11G did not significantly change plasma AST levels, indicating that they do not affect liver function (**Figure 4E**). We performed hematoxylin and eosin (H&E) staining on sections of the major organs. We plan to observe the tissue sections for any morphological changes, necrosis, or other signs of toxicity (**Figure 4F**).

## Discussion

The small molecule EGCG, abundant in green tea, has long been known to disaggregate amyloid fibrils(*24*–*26*). In a recent study, to understand how EGCG can disaggregate stable fibrils, we used cryo-electron microscopy to determine the atomic structure of AD brain-extracted tau bound to EGCG(*28*). Using the EGCG binding position as a pharmacophore, we computationally screened thousands of drug-like compounds that have characteristics favoring BBB permeability. With experimental validation, we discovered lead compound CNS-11, which prevents seeding in a tau aggregation cell culture model and disaggregates AD patient brain-derived tau fibrils *in vitro*(*28*).

In this study, we further characterized CNS-11 and screened four of its chemical analogs for their ability to disaggregate AD patient brain-derived tau fibrils *in vitro*. We discovered two chemical analogs, CNS-11D and CNS-11G, that disaggregated AD patient brain-derived tau fibrils and prevented seeding in a tau aggregation cell culture model. Additionally, we found that brain levels of CNS-11D after one-time treatment were significantly higher than those previously reported for CNS-11 or CNS-11G(*29*). To determine whether CNS-11, CNS-11D, and CNS-11G can disaggregate tau *in vivo*, we assessed their ability to reduce insoluble tau in a mouse model of tauopathy. We found that eight weeks of treatment with these compounds significantly reduced levels of insoluble tau in the PS19 mouse model of tauopathy.

The mechanism of action by which these small molecules disaggregate tau fibrils remains unknown. Interestingly, CNS-11 and the four chemical analogs characterized all share the same central amide-type backbone. However, there is no obvious correlation between the differences in their chemical structures and their efficacy. Although CNS-11A is more similar to CNS-11 than either CNS-11D and CNS-11G, the latter two compounds demonstrated greater efficacy in

disaggregating AD brain-derived tau fibrils. To better understand the mechanism of action, we plan to use cryo-EM to determine structures of AD brain-derived tau in a complex with CNS-11 and its analogs, as previously done with EGCG(*28*). These atomic resolution structures could reveal whether these small molecules disaggregate tau through a mechanism similar to that of EGCG.

Treatment with CNS-11, CNS-11D, and CNS-11G each reduced levels of insoluble tau in PS19 mice. The use of these small molecules *in vivo* was greatly limited by their solubility. In future studies, we will investigate formulations that increase their solubility, permit administration in greater doses and through alternative routes (ex. intraperitoneal, subcutaneous), and potentially increase the concentration of small molecules that reach the brain. Interestingly, brain penetrance after one-time treatment was significantly higher for CNS-11D than CNS-11 or CNS-11G, but weekly treatment with CNS-11D, CNS-11, or CNS-11G similarly reduced levels of insoluble tau in PS19 mice. These results suggest accumulation of these small molecules in the brain after repeated administration.

In this study, we discover three small molecules that disaggregate AD brain-derived tau, prevent seeding in a tau aggregation cell culture model, and reduce levels of insoluble tau in a mouse model of tauopathy. This study demonstrates the potential of using structure-based methods to discover small molecules that can disaggregate tau for AD and related tauopathies.

## Methods

**Extraction of tau fibrils from patient brain tissue.** Human autopsy samples were obtained by UCLA Pathology Department according to HHS regulations from patients consenting to autopsy. Samples were provided to the researchers of this study as anonymized tissues. For purification of paired helical filaments (PHFs) and straight filaments (SFs) from AD brain tissue, extractions were performed according to the previously published protocol(*32*) without performing size exclusion chromatography. The fibers are resuspended in 100uL of 20 mM Tris-HCl pH 7.4 containing 100 mM NaCl per gram of tissue.

**Quantitative electron microscopy.** Negatively stained EM Grids were prepared by depositing 6 µl of sample on formvar/carbon-coated copper grids (400 mesh) for 3 min. The sample was rapidly wicked using filter paper without drying the grid and stained with 1% uranyl acetate for 2 min. For quantitative EM image (qEM), Negative-stain EM grids of each sample were screened at a magnification of ×11,500, collecting images in 5-micron increments. Fibrils were counted from collections of 40 micrographs for each experimental condition.

**Inhibitor screening in tau biosensor cells.** HEK293T cell lines stably expressing tau-K18 P301S-eYFP were obtained from Marc Diamond and used without further characterization or authentication. Cells were maintained in DMEM (Life Technologies, cat. 11965092) supplemented with 10% (vol/vol) FBS (Life Technologies, cat. A3160401), 1% penicillin/streptomycin (Life Technologies, cat. 15140122), and 1% Glutamax (Life Technologies, cat. 35050061) at 37 °C, 5% $CO_2$ in a humidified incubator. Fibrils and patient-derived crude brain extracts were incubated for 16–18 h at 4 °C with indicated inhibitor to yield a final inhibitor concentration of 10 µM (on the biosensor cells. Inhibitors were dissolved in DMSO. For seeding, inhibitor-treated seeds were sonicated in a cuphorn water bath for 3 min, and then mixed with 1

volume of Lipofectamine 3000 (Life Technologies, cat. 11668027) prepared by diluting 1 µl of Lipofectamine in 19 µl of OptiMEM. After twenty minutes, 10 µl of fibrils were added to 90 µl of tau biosensor cells. The number of seeded aggregates was determined by imaging the entire well of a 96-well plate in triplicate using a Celigo Image Cytometer (Nexcelom) in the YFP channel. The number of aggregates in each image was determined using an ImageJ 2.3.0 script, which subtracts the background fluorescence from unseeded cells, and then counts the number of aggregates as peaks with fluorescence above the background using the built-in Particle Analyzer. The number of aggregates was normalized to the confluence of each well, and dose-response plots were generated by calculating the average and standard deviations from triplicate measurements.

**Animal studies.** P301S transgenic mice (Prnp-MAPT*P301S PS19Vle/J, JAX stock #008169, the Jackson Laboratory, Bar Harbor, ME) and B6C3F1/J mice (JAX stock #100010, the Jackson Laboratory) were housed in groups of up to four in individually ventilated cages under standard conditions (22°C, 12-hour light-dark cycle) receiving food and water ad libitum. All animal experiments were performed in accordance with the National Institutes of Health regulations and approved by UCLA Animal Research Committee and performed under oversight of the Division of Laboratory Animal Medicine.

**Recombinant tau-K18+ expression and purification.** Recombinant tau-K18+ was expressed and purified as previously described(*33*).

**Stereotaxic seeding of mice with recombinant tau-K18+ fibrils.** For *in vivo* studies of CNS-11, 10 two-month-old, male PS19 mice were stereotaxically injected with 1.5 µl of recombinant tau-K18+ pre-formed fibrils (5 µg/µl) in the hippocampus (A/P, −2.5 mm from bregma; L, +2.0 mm; D/V, −1.4 mm) and frontal cortex (A/P, +2.0 mm; L, +2.0 mm; D/V, −1.7 mm), as previously

described(*31*). In addition, 4 wild-type, age-matched B6C3F1/J mice were stereotaxically injected with vehicle (1xPBS) to serve as controls. For *in vivo* studies of CNS-11D and CNS-11G, 15 two-month-old, male PS19 mice were stereotaxically injected with 3 µl of recombinant tau-K18+ pre-formed fibrils (5 µg/µl) in the left hippocampus (A/P, −2.0 mm from bregma; L, -2.0 mm; D/V, −1.4 mm and -1.7 mm, 1.5 µl per depth) and the right hippocampus (A/P, −2.0 mm from bregma; L, +2.0 mm; D/V, −1.4 mm and -1.7 mm, 1.5 µl per depth).

**Treatment of mice with CNS-11, CNS-11D, or CNS-11G.** For *in vivo* studies of CNS-11, the 10 PS19 mice were divided into two groups (n = 5 per group). Beginning four weeks after surgery, each group was intravenously administered with CNS-11 at a dose of 1 mg/kg by tail vein, or with vehicle (1xPBS with 10% DMSO), every week for 8 weeks. The weight of each mouse was recorded weekly. The 4 wild-type, age-matched B6C3F1/J mice were intravenously administered with vehicle to serve as a control. For *in vivo* studies of CNS-11D and CNS-11G, the 15 PS19 mice were divided into two groups (n = 5 per group). Beginning two weeks after surgery, each group was intravenously administered with CNS-11D or CNS-11G at a dose of 1 mg/kg by tail vein, or with vehicle (1xPBS with 10% DMSO), every week for 8 weeks. The weight of each mouse was recorded weekly.

**Euthanasia of mice.** Mice were sacrificed by overdose with pentobarbital and then transcardial perfusion with perfusion buffer (1x PBS with sodium vanadate, leupeptin, aprotinin, pepstatin, sodium pyrophosphate, sodium fluoride, PMSF). For *in vivo* studies of CNS-11, the brain was removed and immediately frozen in liquid nitrogen and stored at -80°C until used. For *in vivo* studies of CNS-11D and CNS-11G, the right hemisphere of the brain was removed and immediately frozen in liquid nitrogen and stored at -80°C until used. The left hemisphere of the brain was removed and underwent three nights post-fixation in neutral buffered formalin (Thermo Fisher Scientific), transfer to 70% EtOH, and processing and embedding in paraffin.

**Western blot analyses.** PBS-perfused unfixed brains were used for biochemical analysis by dissecting the hippocampi separately. Before analysis, the brain samples were sonicated in RIPA buffer (4 vol/g) [50 mM tris, 150 nM NaCl, 0.1% SDS, 0.5% sodium deoxycholate, 1% NP-40, 5 mM EDTA, 1 mM phenylmethylsulfonyl fluoride, 0.1% protease inhibitor mixture, and 0.5% phosphatase inhibitor (pH 8.0)] and centrifuged at 100,000g for 30 min at 4°C. The supernatants were saved as RIPA-soluble fractions, whereas the RIPA-insoluble pellets were washed with 1 M sucrose in RIPA buffer to remove myelin and associated lipids and centrifuged at 100,000g for 30 min at 4°C. The RIPA-insoluble pellets were then extracted in tissue (1 vol/g) with 2% SDS buffer [50 mM tris-HCl (pH 7.6)]. The protein contents of the samples were measured using the BCA Protein Assay Kit (Pierce, Bonn, Germany) and diluted to the same concentration (500 μg/ml). Soluble and insoluble fractions were analyzed by SDS-PAGE, followed by Western blotting using an anti-tau antibody (1:5000; A0024, Dako). β-Actin was used as a loading control (1:2000; sc-47778, Santa Cruz Biotechnology). Bands were quantified using ImageJ software.

**Determination of blood AST levels as an index of hepatic toxicity.** Blood samples were obtained by cardiac puncture and centrifuged at 2000 g for 20 min to separate the serum for collection. Activities AST was assayed using Mouse AST enzyme-linked immunosorbent assay kits (Abcam, ab263882) according to the manufacturer's protocols.

**Hematoxylin and eosin staining.** Major organs including heart, liver, spleen, lung, and kidney (n = 2) were fixed in 4% buffered formalin saline (Sigma-Aldrich) at 4°C overnight and then embedded in paraffin blocks. Tissue sections of 5 μm thickness were stained with hematoxylin and eosin (H&E). The morphology of the tissue was observed under a light microscope (Leica) at 20x magnification.

**Acknowledgements**

We thank the donors and their families without whom this work would not have been possible. Research reported in this publication was supported by 1R01AG070895 (D.S.E.) and R01 AG048120 (D.S.E.). H.P. is supported by the UCLA-Caltech Medical Scientist Training Program (GM08042), the UCLA Chemistry-Biology Interface Training Grant (5T32GM008496), and the Ruth L. Kirschstein National Research Service Award (1F30AG077832-01A1). We thank Marc Diamond from UT Southwestern for the generous gift of biosensor cells. We thank the UCLA Behavior Testing Core for assistance with behavior testing. We thank the UCLA Translational Pathology Core Laboratory for assistance in paraffin embedding mouse brain tissue.

**Author contributions**

H.P., X.C., J.Z., K.H., K.M., C.Z., M.M., T.H., G.E., R.A., and A.B. performed research; H.P., X.C., J.Z., H.M., J.P.W., G.M.C, and S.A.F analyzed data; C.K.W. and H.V.V. contributed patient brain samples; H.P., X.C., J.Z. and D.S.E wrote the manuscript with contributions from all other authors.

**Potential conflicts**

DSE is SAB chair and equity holder in ADRx, Inc.

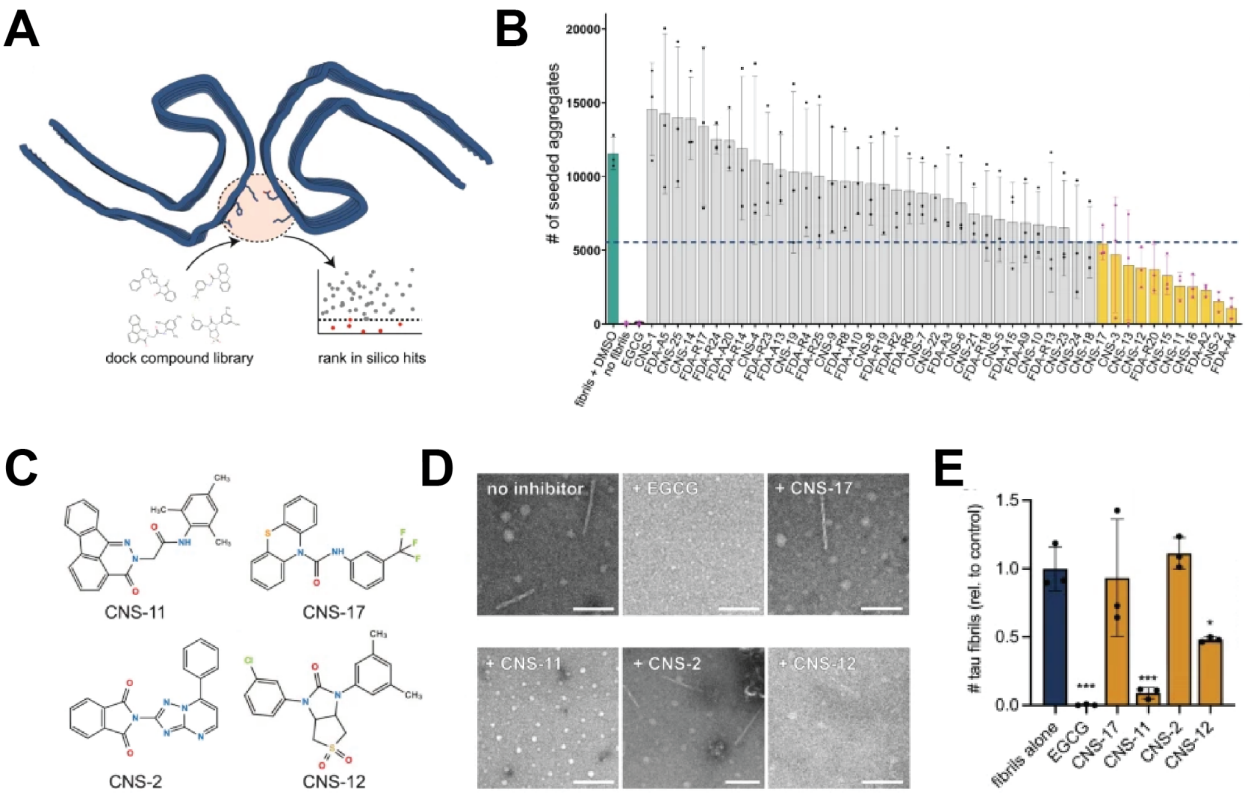


**Figure 1. Discovery of CNS-11 as a tau disaggregator.** Adapted from Seidler PM*, Murray KA*, Boyer DR*, et al. (*28*). **(A)** To identify novel compounds capable of fibril disaggregation, an *in silico* screen using the EGCG binding site to the tau PHF (red circle) was performed. Two libraries of compounds were docked to the site using two computational methods (AutoDock and Rosetta), and hits were ranked and selected for experimental characterization. **(B)** Compounds were initially screened using an *in vitro* biosensor cell assay. Fibrils treated with vehicle (DMSO) served as a control (turquoise bar). The dashed line indicates a 50% reduction in the number of aggregates. Yellow bars indicate any compound that produces a >50% reduction in aggregate formation. Error bars represent ±SD, all experiments were performed with n = 3 experimental replicates. **(C)** Top hits from the *in silico* and biosensor cell screens were selected for further experimental characterization. Four compounds were selected, CNS-11, CNS-17, CNS-2, and CNS-12. **(D)** Electron micrographs of brain-derived tau fibrils after

incubation with each compound and EGCG. Scale bars represent 250 nm. **(E)** Quantitation of fibril number present on EM images with and without compound treatment. N = 33 images were taken from random points on the EM grid, and fibrils were counted. Error bars represent the standard deviation of triplicate technical measurements.

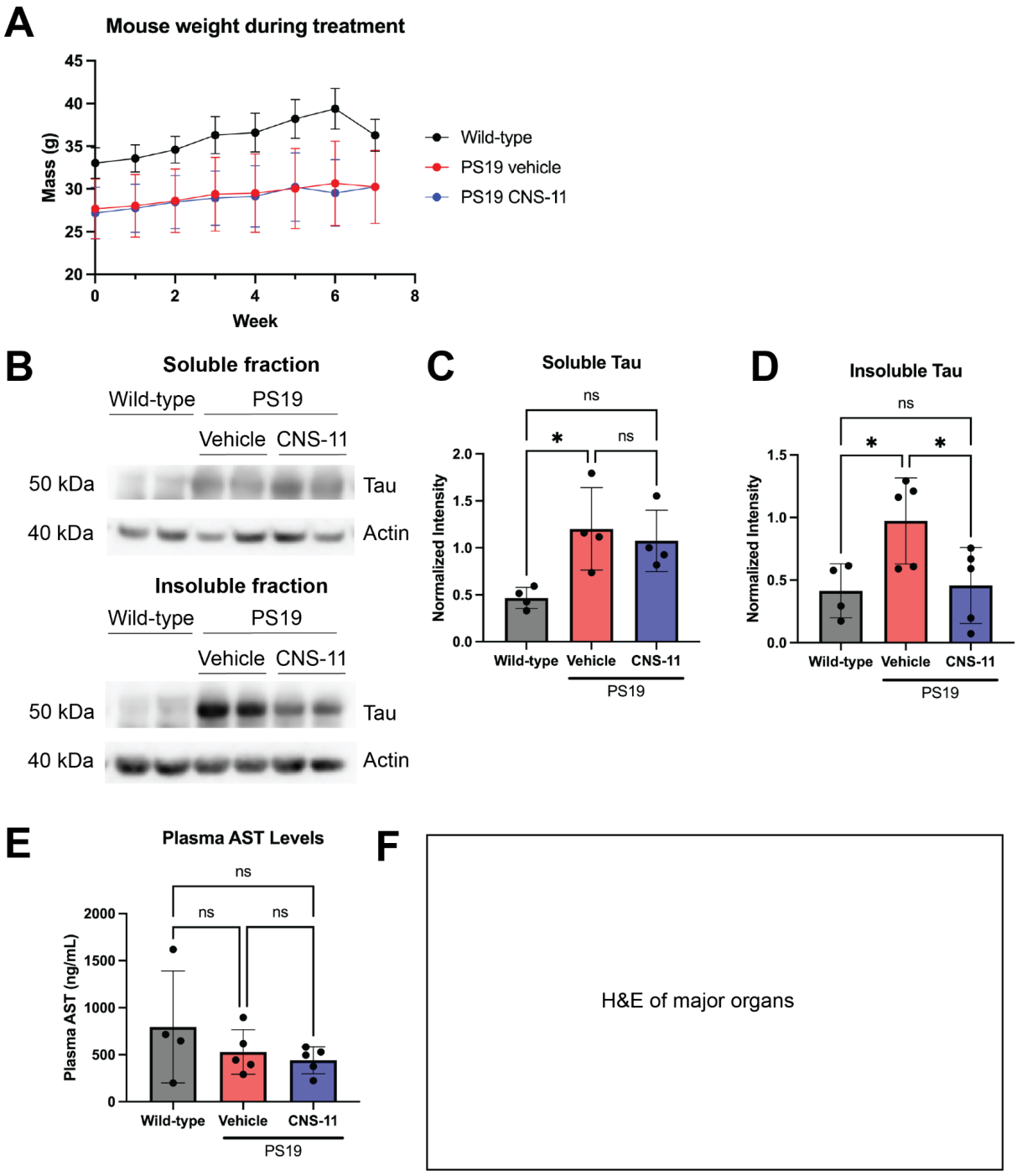


**Figure 2. CNS-11 reduces levels of insoluble tau in PS19 mice without causing obvious toxicity. (A)** CNS-11 at a dose of 1 mg per kg of body weight (mg/kg) was administered by tail vein injection to n = 5 mice, and vehicle (1xPBS with 10% DMSO) was administered to n = 5

mice, once a week for eight weeks. The weight of each mouse was recorded weekly. **(B)** The right hippocampus of each mouse was homogenized in RIPA buffer, separated into RIPA-soluble and RIPA-insoluble fractions, and analyzed by Western blot analysis. **(C)** Seeded PS19 mice had significantly higher levels of soluble tau compared to wild-type mice. Treatment of PS19 mice with CNS-11 did not significantly change levels of tau in the soluble fraction. Statistical analysis was performed using two-way ANOVA (multiple comparisons using Šídák's multiple comparisons test; ns, $p > 0.05$; *, $p < 0.05$; **, $p < 0.01$; ***, $p < 0.001$; ****, $p < 0.0001$) in GraphPad Prism. **(D)** Seeded PS19 mice had significantly higher levels of in soluble tau compared to wild-type mice. Treatment of PS19 mice with CNS-11 significantly reduced levels of tau in the insoluble fraction. Statistical analysis was performed using two-way ANOVA (multiple comparisons using Šídák's multiple comparisons test; ns, $p > 0.05$; *, $p < 0.05$; **, $p < 0.01$; ***, $p < 0.001$; ****, $p < 0.0001$) in GraphPad Prism. **(E)** Treatment with CNS-11 did not significantly change plasma AST levels, indicating that it does not affect liver function. Statistical analysis was performed using two-way ANOVA (multiple comparisons using Šídák's multiple comparisons test; ns, $p > 0.05$; *, $p < 0.05$; **, $p < 0.01$; ***, $p < 0.001$; ****, $p < 0.0001$) in GraphPad Prism. **(F)** H&E-stained tissue sections from major organs will be observed for any morphological changes, necrosis, or other signs of toxicity.

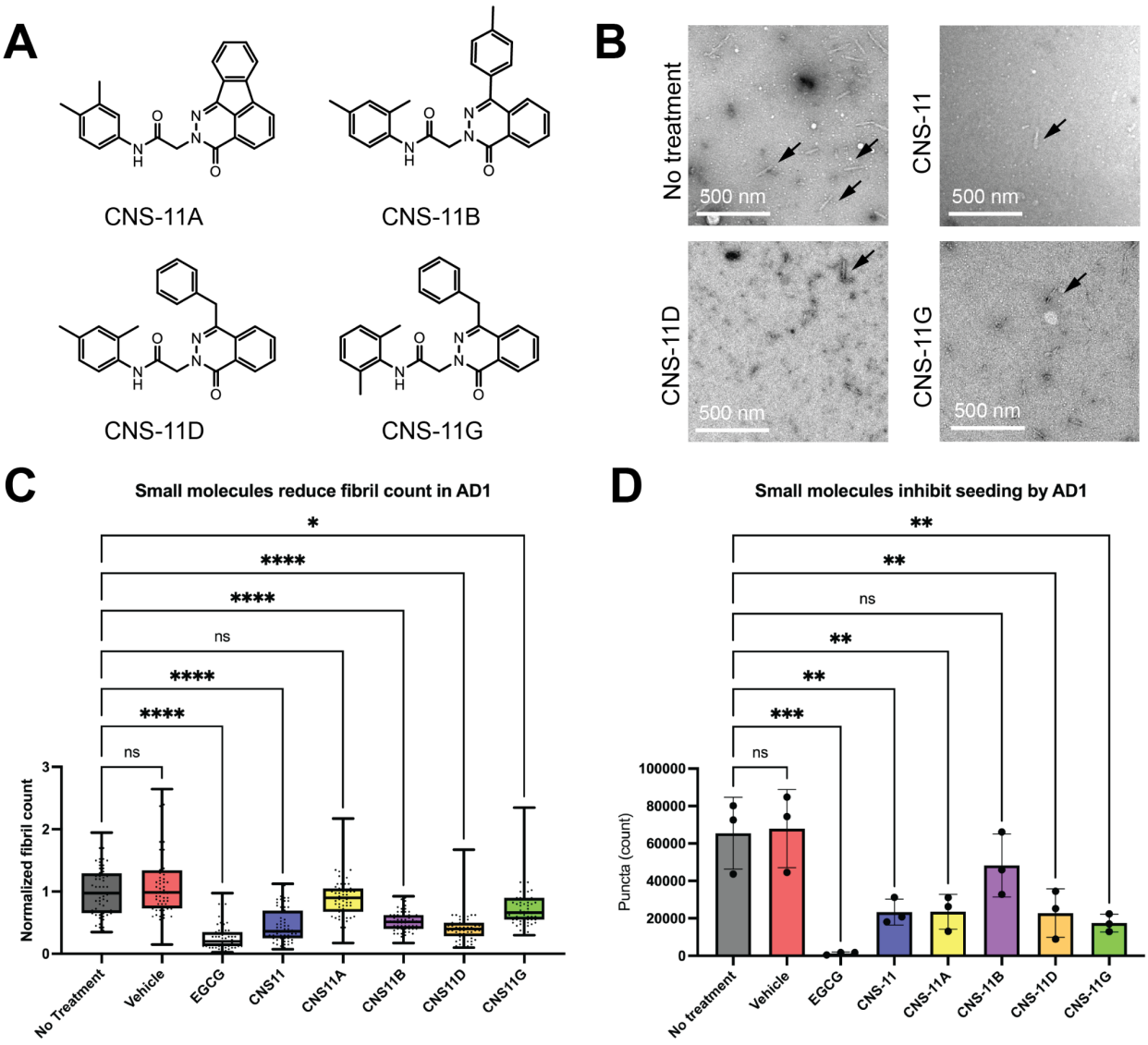


**Figure 3. Chemical analogs of CNS-11 also disaggregate tau fibrils from AD patients and prevent seeding in HEK293 biosensor cells.** **(A)** Chemical analogs of CNS-11. **(B)** Electron micrographs of AD brain-derived tau fibrils from AD1 after incubation with no treatment, vehicle (DMSO), EGCG, CNS-11, or one of the four chemical analogs of CNS-11. **(C)** Quantification of AD brain-derived tau fibrils (black arrows) present on EM images (n = 40 images taken from random points on the EM grid). Images were approximately 4x the size of images in (B). Statistical analysis was performed using a Kruskal–Wallis test followed by a Dunn's multiple

comparison test (ns, P > 0.05; *P ≤ 0.05; **P ≤ 0.01; ***P ≤ 0.001; ****P ≤ 0.0001) in GraphPad Prism. **(D)** Quantification of fluorescent puncta formed in HEK293T biosensor cells seeded with AD brain-derived fibrils from AD1. Prior to seeding, fibrils were incubated with no treatment, vehicle (DMSO), EGCG, CNS-11, or one of the four chemical analogs of CNS-11. Statistical analysis was performed using one-way ANOVA followed by a Tukey's multiple comparison test (ns, P > 0.05; *P ≤ 0.05; **P ≤ 0.01; ***P ≤ 0.001; ****P ≤ 0.0001) in GraphPad Prism.

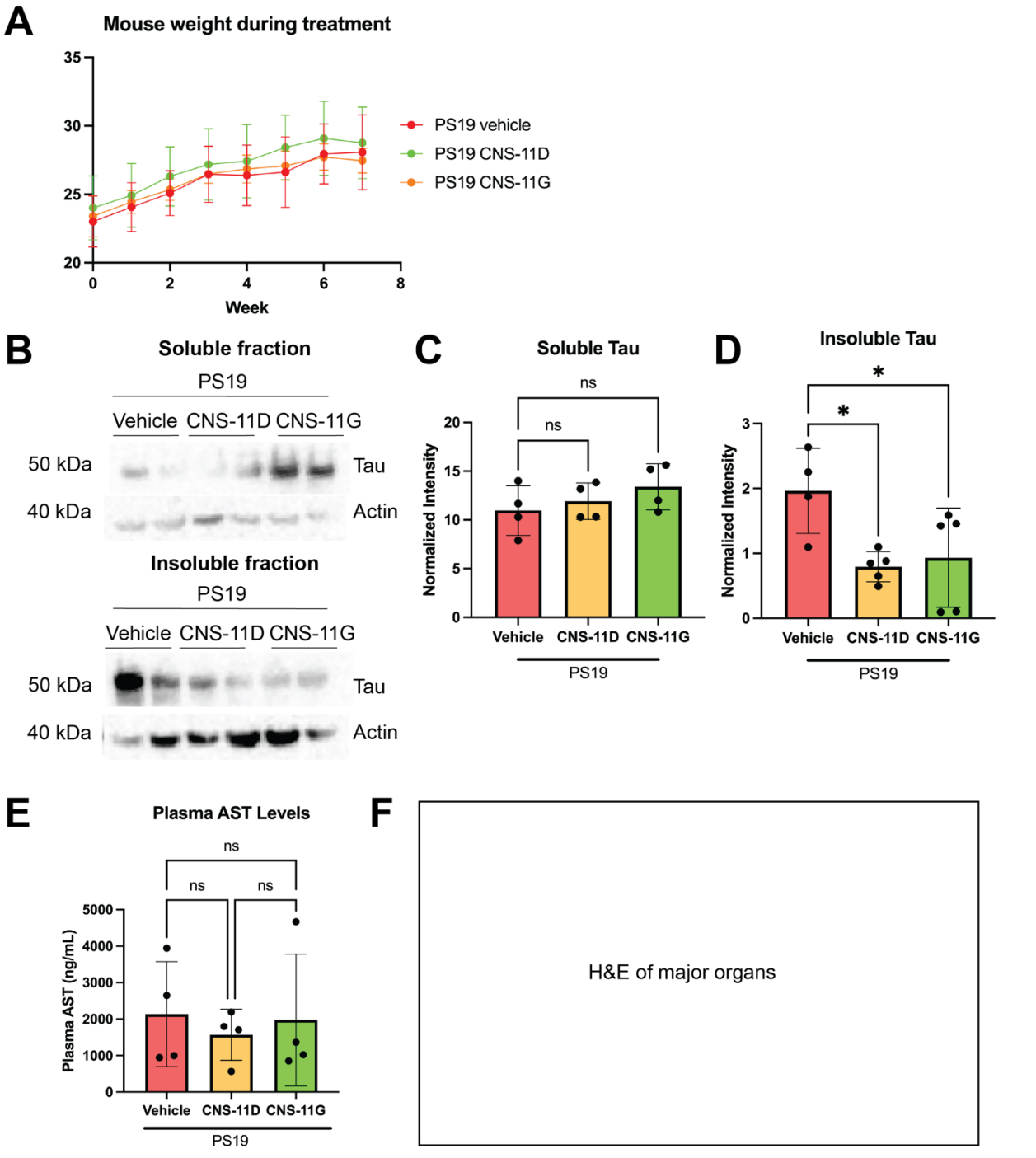


**Figure 4. CNS-11D and CNS-11G reduce levels of insoluble tau in PS19 mice without causing obvious toxicity. (A)** CNS-11D or CNS-11G at a dose of 1 mg per kg of body weight (mg/kg) was administered by tail vein injection to n = 5 mice, and vehicle (1xPBS with 10%

DMSO) was administered to n = 5 mice, once a week for eight weeks. The weight of each mouse was recorded weekly. **(B)** The right hippocampus of each mouse was homogenized in RIPA buffer, separated into RIPA-soluble and RIPA-insoluble fractions, and analyzed by Western blot analysis. **(C)** Treatment of PS19 mice with CNS-11D or CNS-11G did not significantly change levels of tau in the soluble fraction. Statistical analysis was performed using two-way ANOVA (multiple comparisons using Šídák's multiple comparisons test; ns, $p > 0.05$; *, $p < 0.05$; **, $p < 0.01$; ***, $p < 0.001$; ****, $p < 0.0001$) in GraphPad Prism. **(D)** Treatment of PS19 mice with either CNS-11D or CNS-11G significantly reduced levels of tau in the insoluble fraction. Statistical analysis was performed using two-way ANOVA (multiple comparisons using Šídák's multiple comparisons test; ns, $p > 0.05$; *, $p < 0.05$; **, $p < 0.01$; ***, $p < 0.001$; ****, $p < 0.0001$) in GraphPad Prism. **(E)** Treatment with CNS-11D or CNS-11G did not significantly change plasma AST levels, indicating that they do not affect liver function. Statistical analysis was performed using two-way ANOVA (multiple comparisons using Šídák's multiple comparisons test; ns, $p > 0.05$; *, $p < 0.05$; **, $p < 0.01$; ***, $p < 0.001$; ****, $p < 0.0001$) in GraphPad Prism. **(F)** H&E-stained tissue sections from major organs will be observed for any morphological changes, necrosis, or other signs of toxicity.

**References**


1. J. Sevigny, P. Chiao, T. Bussière, P. H. Weinreb, L. Williams, M. Maier, R. Dunstan, S. Salloway, T. Chen, Y. Ling, J. O'Gorman, F. Qian, M. Arastu, M. Li, S. Chollate, M. S. Brennan, O. Quintero-Monzon, R. H. Scannevin, H. M. Arnold, T. Engber, K. Rhodes, J. Ferrero, Y. Hang, A. Mikulskis, J. Grimm, C. Hock, R. M. Nitsch, A. Sandrock, The antibody aducanumab reduces Aβ plaques in Alzheimer's disease. *Nature* **537**, 50–56 (2016).
2. C. J. Swanson, Y. Zhang, S. Dhadda, J. Wang, J. Kaplow, R. Y. K. Lai, L. Lannfelt, H. Bradley, M. Rabe, A. Koyama, L. Reyderman, D. A. Berry, S. Berry, R. Gordon, L. D. Kramer, J. L. Cummings, A randomized, double-blind, phase 2b proof-of-concept clinical trial in early Alzheimer's disease with lecanemab, an anti-Aβ protofibril antibody. *Alzheimers Res. Ther.* **13**, 80 (2021).
3. P. V. Arriagada, J. H. Growdon, E. T. Hedley-Whyte, B. T. Hyman, Neurofibrillary tangles but not senile plaques parallel duration and severity of Alzheimer's disease. *Neurology* **42**, 631–639 (1992).
4. T. Gómez-Isla, R. Hollister, H. West, S. Mui, J. H. Growdon, R. C. Petersen, J. E. Parisi, B. T. Hyman, Neuronal loss correlates with but exceeds neurofibrillary tangles in Alzheimer's disease. *Ann. Neurol.* **41**, 17–24 (1997).
5. P. Giannakopoulos, F. R. Herrmann, T. Bussière, C. Bouras, E. Kövari, D. P. Perl, J. H. Morrison, G. Gold, P. R. Hof, Tangle and neuron numbers, but not amyloid load, predict cognitive status in Alzheimer's disease. *Neurology* **60**, 1495–1500 (2003).
6. D. A. Bennett, J. A. Schneider, R. S. Wilson, J. L. Bienias, S. E. Arnold, Neurofibrillary tangles mediate the association of amyloid load with clinical Alzheimer disease and level of cognitive function. *Arch. Neurol.* **61**, 378–384 (2004).
7. V. Haroutunian, P. Davies, C. Vianna, J. D. Buxbaum, D. P. Purohit, Tau protein abnormalities associated with the progression of alzheimer disease type dementia. *Neurobiol. Aging* **28**, 1–7 (2007).

8. H. Cho, J. Y. Choi, M. S. Hwang, J. H. Lee, Y. J. Kim, H. M. Lee, C. H. Lyoo, Y. H. Ryu, M. S. Lee, Tau PET in Alzheimer disease and mild cognitive impairment. *Neurology* **87**, 375–383 (2016).

9. L. Wang, T. L. Benzinger, Y. Su, J. Christensen, K. Friedrichsen, P. Aldea, J. McConathy, N. J. Cairns, A. M. Fagan, J. C. Morris, B. M. Ances, Evaluation of Tau Imaging in Staging Alzheimer Disease and Revealing Interactions Between β-Amyloid and Tauopathy. *JAMA Neurol.* **73**, 1070–1077 (2016).

10. C. Xia, S. J. Makaretz, C. Caso, S. McGinnis, S. N. Gomperts, J. Sepulcre, T. Gomez-Isla, B. T. Hyman, A. Schultz, N. Vasdev, K. A. Johnson, B. C. Dickerson, Association of In Vivo [18F]AV-1451 Tau PET Imaging Results With Cortical Atrophy and Symptoms in Typical and Atypical Alzheimer Disease. *JAMA Neurol.* **74**, 427–436 (2017).

11. R. La Joie, A. V. Visani, S. L. Baker, J. A. Brown, V. Bourakova, J. Cha, K. Chaudhary, L. Edwards, L. Iaccarino, M. Janabi, O. H. Lesman-Segev, Z. A. Miller, D. C. Perry, J. P. O'Neil, J. Pham, J. C. Rojas, H. J. Rosen, W. W. Seeley, R. M. Tsai, B. L. Miller, W. J. Jagust, G. D. Rabinovici, Prospective longitudinal atrophy in Alzheimer's disease correlates with the intensity and topography of baseline tau-PET. *Sci. Transl. Med.* **12**, eaau5732 (2020).

12. H. Braak, E. Braak, Neuropathological stageing of Alzheimer-related changes. *Acta Neuropathol. (Berl.)* **82**, 239–259 (1991).

13. H. Braak, E. Braak, Staging of Alzheimer's disease-related neurofibrillary changes. *Neurobiol. Aging* **16**, 271–278; discussion 278-284 (1995).

14. B. Frost, J. Ollesch, H. Wille, M. I. Diamond, Conformational diversity of wild-type Tau fibrils specified by templated conformation change. *J. Biol. Chem.* **284**, 3546–3551 (2009).

15. B. Frost, R. L. Jacks, M. I. Diamond, Propagation of tau misfolding from the outside to the inside of a cell. *J. Biol. Chem.* **284**, 12845–12852 (2009).

16. J. L. Guo, V. M.-Y. Lee, Seeding of normal Tau by pathological Tau conformers drives

pathogenesis of Alzheimer-like tangles. *J. Biol. Chem.* **286**, 15317–15331 (2011).

17. B. B. Holmes, J. L. Furman, T. E. Mahan, T. R. Yamasaki, H. Mirbaha, W. C. Eades, L. Belaygorod, N. J. Cairns, D. M. Holtzman, M. I. Diamond, Proteopathic tau seeding predicts tauopathy in vivo. *Proc. Natl. Acad. Sci. U. S. A.* **111**, E4376-4385 (2014).
18. F. Clavaguera, T. Bolmont, R. A. Crowther, D. Abramowski, S. Frank, A. Probst, G. Fraser, A. K. Stalder, M. Beibel, M. Staufenbiel, M. Jucker, M. Goedert, M. Tolnay, Transmission and spreading of tauopathy in transgenic mouse brain. *Nat. Cell Biol.* **11**, 909–913 (2009).
19. F. Clavaguera, H. Akatsu, G. Fraser, R. A. Crowther, S. Frank, J. Hench, A. Probst, D. T. Winkler, J. Reichwald, M. Staufenbiel, B. Ghetti, M. Goedert, M. Tolnay, Brain homogenates from human tauopathies induce tau inclusions in mouse brain. *Proc. Natl. Acad. Sci. U. S. A.* **110**, 9535–9540 (2013).
20. M. Iba, J. L. Guo, J. D. McBride, B. Zhang, J. Q. Trojanowski, V. M.-Y. Lee, Synthetic tau fibrils mediate transmission of neurofibrillary tangles in a transgenic mouse model of Alzheimer's-like tauopathy. *J. Neurosci. Off. J. Soc. Neurosci.* **33**, 1024–1037 (2013).
21. S. Boluda, M. Iba, B. Zhang, K. M. Raible, V. M.-Y. Lee, J. Q. Trojanowski, Differential induction and spread of tau pathology in young PS19 tau transgenic mice following intracerebral injections of pathological tau from Alzheimer's disease or corticobasal degeneration brains. *Acta Neuropathol. (Berl.)* **129**, 221–237 (2015).
22. J. L. Guo, S. Narasimhan, L. Changolkar, Z. He, A. Stieber, B. Zhang, R. J. Gathagan, M. Iba, J. D. McBride, J. Q. Trojanowski, V. M. Y. Lee, Unique pathological tau conformers from Alzheimer's brains transmit tau pathology in nontransgenic mice. *J. Exp. Med.* **213**, 2635–2654 (2016).
23. S. Narasimhan, J. L. Guo, L. Changolkar, A. Stieber, J. D. McBride, L. V. Silva, Z. He, B. Zhang, R. J. Gathagan, J. Q. Trojanowski, V. M. Y. Lee, Pathological Tau Strains from Human Brains Recapitulate the Diversity of Tauopathies in Nontransgenic Mouse Brain. *J. Neurosci. Off. J. Soc. Neurosci.* **37**, 11406–11423 (2017).

24. D. E. Ehrnhoefer, J. Bieschke, A. Boeddrich, M. Herbst, L. Masino, R. Lurz, S. Engemann, A. Pastore, E. E. Wanker, EGCG redirects amyloidogenic polypeptides into unstructured, off-pathway oligomers. *Nat. Struct. Mol. Biol.* **15**, 558–566 (2008).

25. J. Bieschke, J. Russ, R. P. Friedrich, D. E. Ehrnhoefer, H. Wobst, K. Neugebauer, E. E. Wanker, EGCG remodels mature alpha-synuclein and amyloid-beta fibrils and reduces cellular toxicity. *Proc. Natl. Acad. Sci. U. S. A.* **107**, 7710–7715 (2010).

26. S. K. Sonawane, H. Chidambaram, D. Boral, N. V. Gorantla, A. A. Balmik, A. Dangi, S. Ramasamy, U. K. Marelli, S. Chinnathambi, EGCG impedes human Tau aggregation and interacts with Tau. *Sci. Rep.* **10**, 12579 (2020).

27. V. Andreu-Fernández, L. Almeida Toledano, N. Pizarro, E. Navarro-Tapia, M. D. Gómez-Roig, R. de la Torre, Ó. García-Algar, Bioavailability of Epigallocatechin Gallate Administered With Different Nutritional Strategies in Healthy Volunteers. *Antioxid. Basel Switz.* **9**, 440 (2020).

28. P. M. Seidler, K. A. Murray, D. R. Boyer, P. Ge, M. R. Sawaya, C. J. Hu, X. Cheng, R. Abskharon, H. Pan, M. A. DeTure, C. K. Williams, D. W. Dickson, H. V. Vinters, D. S. Eisenberg, Structure-based discovery of small molecules that disaggregate Alzheimer's disease tissue derived tau fibrils in vitro. *Nat. Commun.* **13**, 5451 (2022).

29. K. A. Murray, C. J. Hu, H. Pan, J. Lu, R. Abskharon, J. T. Bowler, G. M. Rosenberg, C. K. Williams, G. Elezi, M. Balbirnie, K. F. Faull, H. V. Vinters, P. M. Seidler, D. S. Eisenberg, Small molecules disaggregate alpha-synuclein and prevent seeding from patient brain-derived fibrils. *Proc. Natl. Acad. Sci. U. S. A.* **120**, e2217835120 (2023).

30. Y. Yoshiyama, M. Higuchi, B. Zhang, S.-M. Huang, N. Iwata, T. C. Saido, J. Maeda, T. Suhara, J. Q. Trojanowski, V. M.-Y. Lee, Synapse loss and microglial activation precede tangles in a P301S tauopathy mouse model. *Neuron* **53**, 337–351 (2007).

31. E. Peeraer, A. Bottelbergs, K. Van Kolen, I.-C. Stancu, B. Vasconcelos, M. Mahieu, H. Duytschaever, L. Ver Donck, A. Torremans, E. Sluydts, N. Van Acker, J. A. Kemp, M.

Mercken, K. R. Brunden, J. Q. Trojanowski, I. Dewachter, V. M. Y. Lee, D. Moechars, Intracerebral injection of preformed synthetic tau fibrils initiates widespread tauopathy and neuronal loss in the brains of tau transgenic mice. *Neurobiol. Dis.* **73**, 83–95 (2015).

32. A. W. P. Fitzpatrick, B. Falcon, S. He, A. G. Murzin, G. Murshudov, H. J. Garringer, R. A. Crowther, B. Ghetti, M. Goedert, S. H. W. Scheres, Cryo-EM structures of tau filaments from Alzheimer's disease. *Nature* **547**, 185–190 (2017).

33. K. Hou, H. Pan, H. Shahpasand-Kroner, C. Hu, R. Abskharon, P. Seidler, M. Mekkittikul, M. Balbirnie, C. Lantz, M. R. Sawaya, J. L. Dolinsky, M. Jones, X. Zuo, J. A. Loo, S. Frautschy, G. Cole, D. S. Eisenberg, D-peptide-magnetic nanoparticles fragment tau fibrils and rescue behavioral deficits in a mouse model of Alzheimer's disease. *Sci. Adv.* **10**, eadl2991 (2024).

| Patient | Braak | Age | Sex | Region |
|---|---|---|---|---|
| AD1 | VI | 67 | F | RT |
| AD2 | VI | 78 | F | LT |
| AD3 | VI | 62 | F | LT |

**Supplementary Table 1. Pathology information for AD patient-derived samples.**

| Recovery of CNS-11D from mouse brain | | | | | | |
|---|---|---|---|---|---|---|
| Sample ID | | CNS-11D 398.1 →249.2 | CNS-11D 398.1 →277.2 | | Internal Standard 396.2 →233.1 | Internal Standard 396.2 →261.0 |
| | rt | area | area | rt | area | area |
| Br. 1A | 16.90 | 36650 | 40677 | 17.00 | 2557 | 2230 |
| Br. 1B | 17.00 | 39725 | 44825 | 17.10 | 2779 | 2476 |
| Br. 1C | 17.00 | 44993 | 50418 | 17.10 | 3276 | 2859 |
| Br. 2A | 17.00 | 66567 | 74862 | 17.10 | 2706 | 2407 |
| Br. 2B | 17.00 | 30108 | 33286 | 17.10 | 1135 | 976 |
| Br. 2C | 16.90 | 71266 | 79883 | 17.00 | 2691 | 2345 |
| Br. 3A | 16.90 | 51890 | 59288 | 17.00 | 2641 | 2334 |
| Br. 3B | 16.90 | 53289 | 60382 | 17.00 | 2768 | 2439 |
| Br. 3C | 16.90 | 65835 | 74231 | 17.00 | 3626 | 3249 |
| Br. 4A | 16.90 | 33981 | 38174 | 17.00 | 1437 | 1326 |
| Br. 4B | 16.90 | 76038 | 85590 | 17.00 | 4050 | 3624 |
| Br. 4C | 16.90 | 51965 | 58396 | 17.00 | 2186 | 1980 |
| Br. 5A | 17.00 | 48273 | 55832 | 17.10 | 2440 | 2269 |
| Br. 5B | 17.00 | 39416 | 46530 | 17.10 | 1945 | 1807 |
| Br. 5C | 17.00 | 48126 | 57030 | 17.10 | 2521 | 2372 |
| Br. 6A | 17.00 | 27439 | 31849 | 17.10 | 2091 | 1844 |
| Br. 6B | 17.00 | 40593 | 47416 | 17.10 | 3071 | 2789 |
| Br. 6C | 17.00 | 30534 | 35610 | 17.10 | 2063 | 1855 |
| Br. 7A | 17.00 | 31322 | 36192 | 17.10 | 3252 | 2934 |
| Br. 7B | 17.00 | 27704 | 32091 | 17.10 | 2754 | 2555 |
| Br. 7C | 17.00 | 50116 | 59037 | 17.10 | 5750 | 5308 |
| Br. 8A | 17.00 | 32398 | 37912 | 17.10 | 3746 | 3488 |
| Br. 8B | 17.00 | 28906 | 34056 | 17.10 | 3215 | 3016 |
| Br. 8C | 17.00 | 34020 | 40190 | 17.10 | 4026 | 3722 |
| Std. 1 (1 pmole) | 16.90 | 2687 | 3073 | 17.00 | 3923 | 4849 |
| Std. 2 (1 pmole) | 16.90 | 3490 | 3934 | 17.00 | 5040 | 4684 |
| Std. 3 (1 pmole) | 16.90 | 2445 | 2733 | 17.00 | 3274 | 2896 |
| Std. 4 (2.5 pmoles) | 16.90 | 16028 | 18355 | 17.00 | 3998 | 3656 |
| Std. 5 (2.5 pmoles) | 16.90 | 15087 | 17257 | 17.00 | 3778 | 3400 |
| Std. 6 (2.5 pmoles) | 16.90 | 11718 | 13324 | 17.00 | 2733 | 2490 |
| Std. 7 (5 pmoles) | 16.90 | 25781 | 29319 | 17.00 | 3467 | 3122 |
| Std. 8 (5 pmoles) | 16.90 | 28792 | 32598 | 17.00 | 3278 | 2986 |
| Std. 9 (5 pmoles) | 16.90 | 18580 | 21001 | 17.00 | 2348 | 2082 |
| Std. 10 (10 pmoles) | 16.90 | 27796 | 31374 | 17.00 | 1920 | 1647 |
| Std. 11 (10 pmoles) | 16.90 | 53272 | 60410 | 17.00 | 3641 | 3136 |
| Std. 12 (10 pmoles) | 16.90 | 6821 | 7695 | 17.00 | 436 | 366 |
| Std. 13 (20 pmoles) | 17.00 | 81513 | 96591 | 17.10 | 3658 | 3311 |
| Std. 14 (20 pmoles) | 17.00 | 58467 | 69281 | 17.10 | 2556 | 2425 |
| Std. 15 (20 pmoles) | 17.00 | 64798 | 76572 | 17.10 | 2693 | 2529 |
| Std. 16 (50 pmoles) | 17.00 | 184065 | 221619 | 17.10 | 3669 | 3466 |
| Std. 17 (50 pmoles) | 17.00 | 167148 | 201722 | 17.10 | 3900 | 3506 |
| Std. 18 (50 pmoles) | 17.00 | 171837 | 204287 | 17.10 | 3260 | 2973 |

**Supplementary Table 2. Raw LC-MS/MS data, brain tissue.**

| Recovery of CNS-11D from mouse plasma | | | | | | |
|---|---|---|---|---|---|---|
| Sample ID | | CNS-11D 398.1 →249.2 | CNS-11D 398.1 →277.2 | | Internal Standard 396.2 →233.1 | Internal Standard 396.2 →261.0 |
| | rt | area | area | rt | area | area |
| Pl. 3A | 16.90 | 3541 | 3978 | 17.00 | 4666 | 4206 |
| Pl. 4A | 16.90 | 4782 | 5385 | 17.00 | 5954 | 5441 |
| Br. 4B | 16.90 | 3242 | 3637 | 17.00 | 4041 | 3654 |
| Pl. 5A | 16.90 | 11572 | 13389 | 17.00 | 4698 | 4408 |
| Pl. 5B | 16.90 | 8492 | 9812 | 17.00 | 5561 | 5011 |
| Pl. 6A | 17.00 | 9442 | 10747 | 17.10 | 8206 | 7520 |
| Pl. 7A | 17.00 | 12176 | 14189 | 17.10 | 6942 | 6307 |
| Br. 7B | 17.00 | 15869 | 18185 | 17.10 | 7185 | 6528 |
| Std. 1 (1 pmole) | 16.90 | 4573 | 5075 | 17.00 | 4500 | 3997 |
| Std. 2 (1 pmole) | 16.90 | 8047 | 8950 | 17.00 | 5654 | 4910 |
| Std. 3 (2.5 pmoles) | 16.90 | 17687 | 20444 | 17.00 | 5483 | 4819 |
| Std. 4 (2.5 pmoles) | 16.90 | 24814 | 27794 | 17.00 | 6447 | 5731 |
| Std. 5 (5 pmoles) | 16.90 | 32683 | 36685 | 17.00 | 4667 | 4252 |
| Std. 6 (5 pmoles) | 16.90 | 41069 | 45375 | 17.00 | 6001 | 5284 |
| Std. 7 (10 pmoles) | 16.90 | 80950 | 90261 | 17.00 | 5621 | 5053 |
| Std. 8 (10 pmoles) | 16.90 | 67386 | 74634 | 17.00 | 4596 | 4175 |

**Supplementary Table 3. Raw LC-MS/MS data, plasma.**

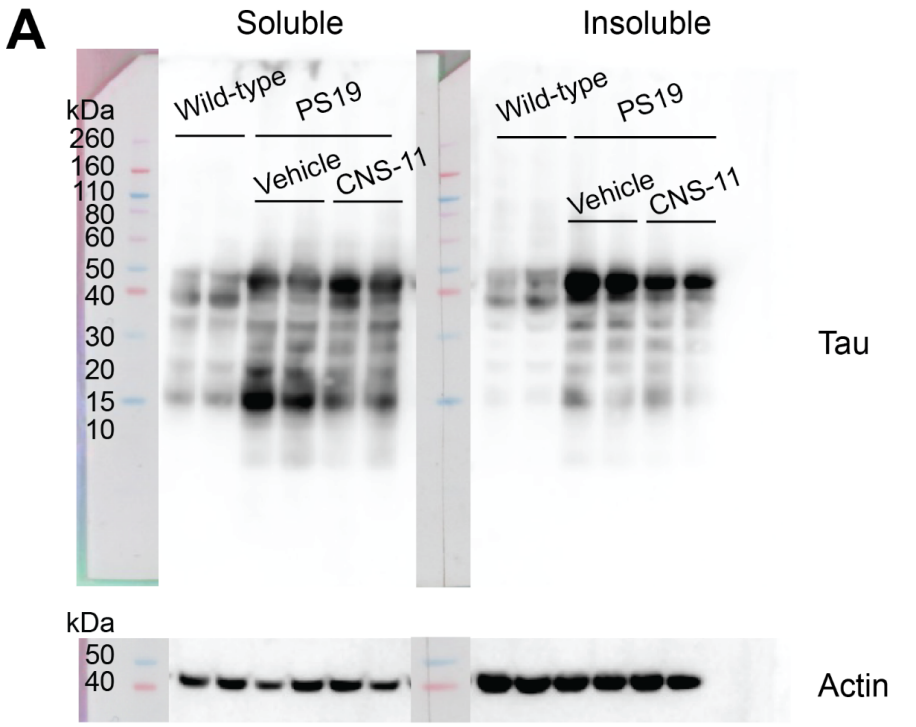
A
Soluble
Insoluble
kDa
260
160
110
80
60
50
40
30
20
15
10
Wild-type
PS19
Vehicle
CNS-11
Wild-type
PS19
Vehicle
CNS-11
Tau
kDa
50
40
Actin

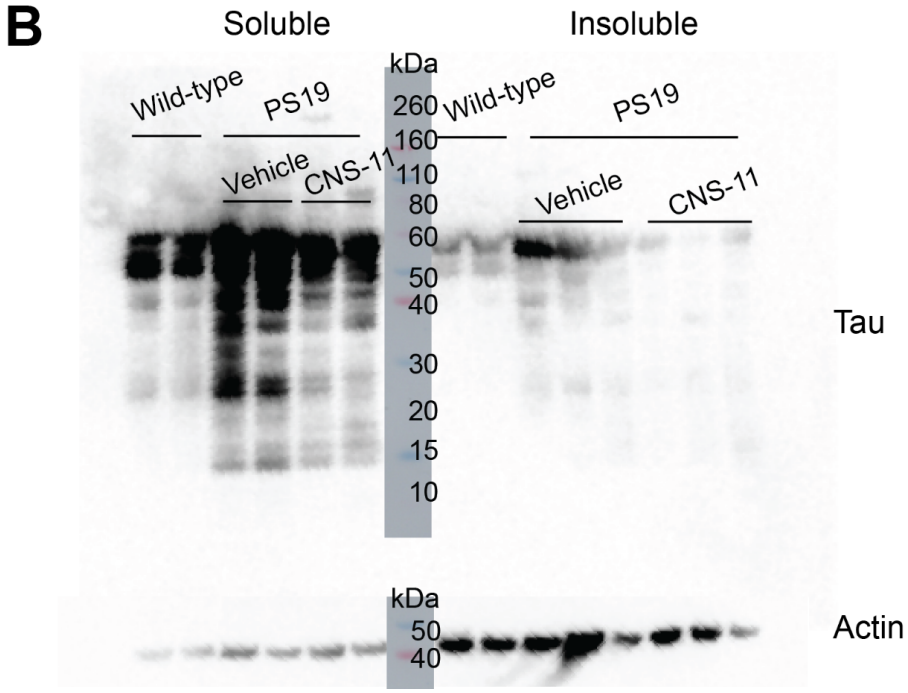
B
Soluble
Insoluble
Wild-type
PS19
Vehicle
CNS-11
kDa
260
160
110
80
60
50
40
30
20
15
10
Wild-type
PS19
Vehicle
CNS-11
Tau
kDa
50
40
Actin

**Supplementary Figure 1. CNS-11 reduces levels of insoluble tau in PS19 mice. (A-B)** The right hippocampus of wild-type mice and PS19 mice treated with vehicle or CNS-11 was homogenized in RIPA buffer, separated into RIPA-soluble and RIPA-insoluble fractions, and analyzed by Western blot analysis. **(A)** Wild-type mice #1, 2; vehicle-treated PS19 mice #1, 2; CNS-11-treated PS19 mice #1, 2. **(B)** Wild-type mice #3, 4; vehicle-treated PS19 mice #3, 4, 5; CNS-11-treated PS19 mice #3, 4, 5.

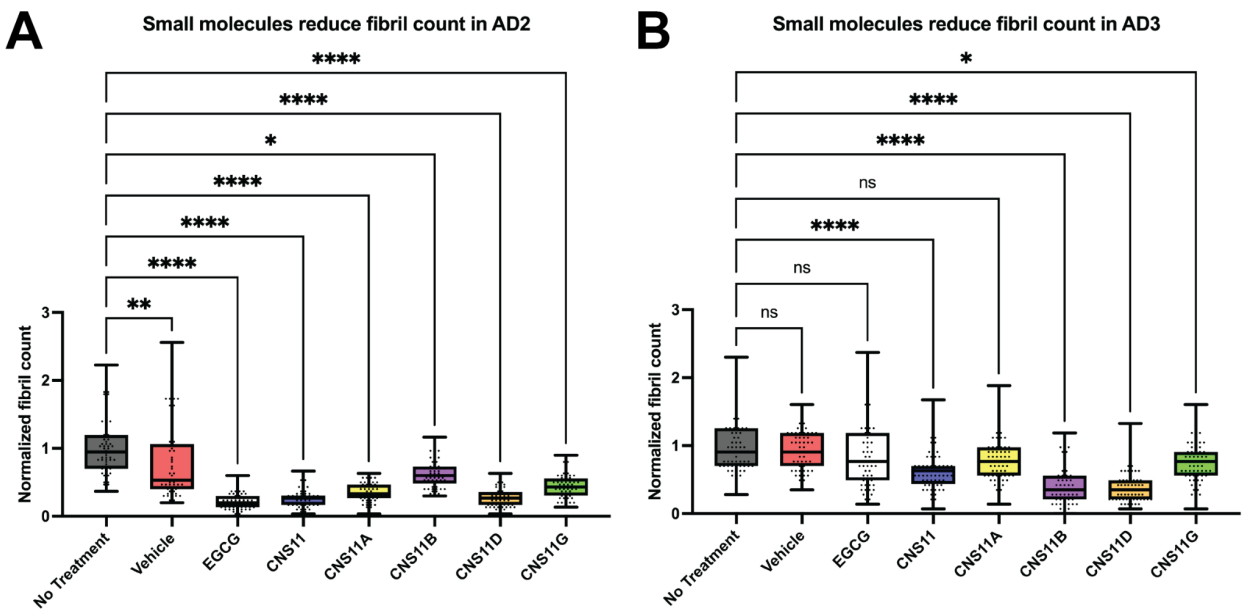


**Supplementary Figure 2. Chemical analogs of CNS-11 also disaggregate tau fibrils from AD patients. (A-B)** Quantification of AD brain-derived tau fibrils from **(A)** AD2 and **(B)** AD3 present on EM images after incubation with no treatment, vehicle (DMSO), EGCG, CNS-11, or one of the four chemical analogs of CNS-11 (n = 40 images taken from random points on the EM grid). Statistical analysis was performed using a Kruskal–Wallis test followed by a Dunn's multiple comparison test (ns, $P > 0.05$; *$P \leq 0.05$; **$P \leq 0.01$; ***$P \leq 0.001$; ****$P \leq 0.0001$) in GraphPad Prism.

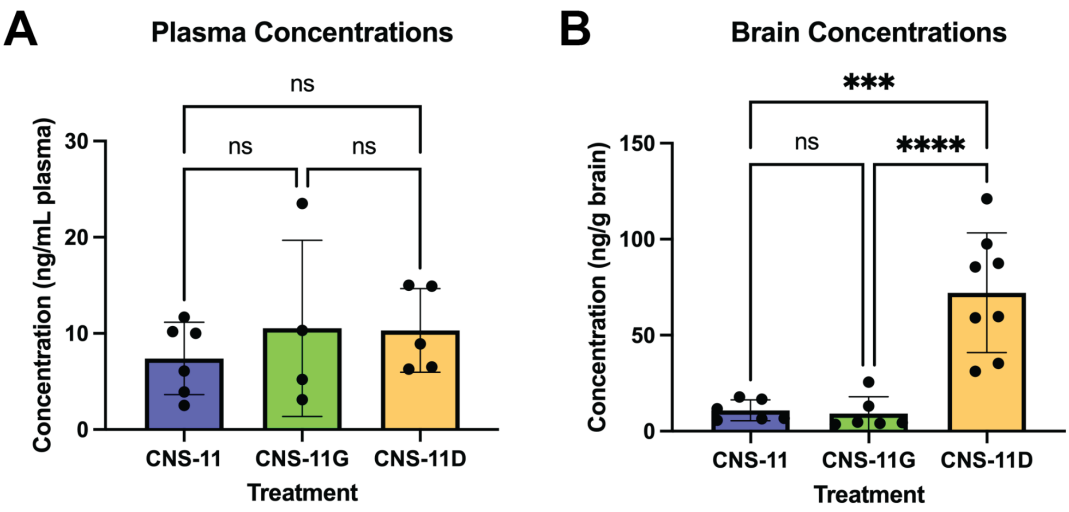


**Supplementary Figure 3. Brain penetration of CNS-11D in mice. (A-B)** Mice were injected intravenously with 1 mg/kg of CNS-11D (n = 8) and euthanized 1 h after dosing. Compound levels in **(A)** plasma and **(B)** brain tissue were analyzed using an LC-MS/MS-MRM method. Statistical analysis was performed using two-way ANOVA (multiple comparisons using Šídák's multiple comparisons test; ns, $p > 0.05$; *, $p < 0.05$; **, $p < 0.01$; ***, $p < 0.001$; ****, $p < 0.0001$) in GraphPad Prism.

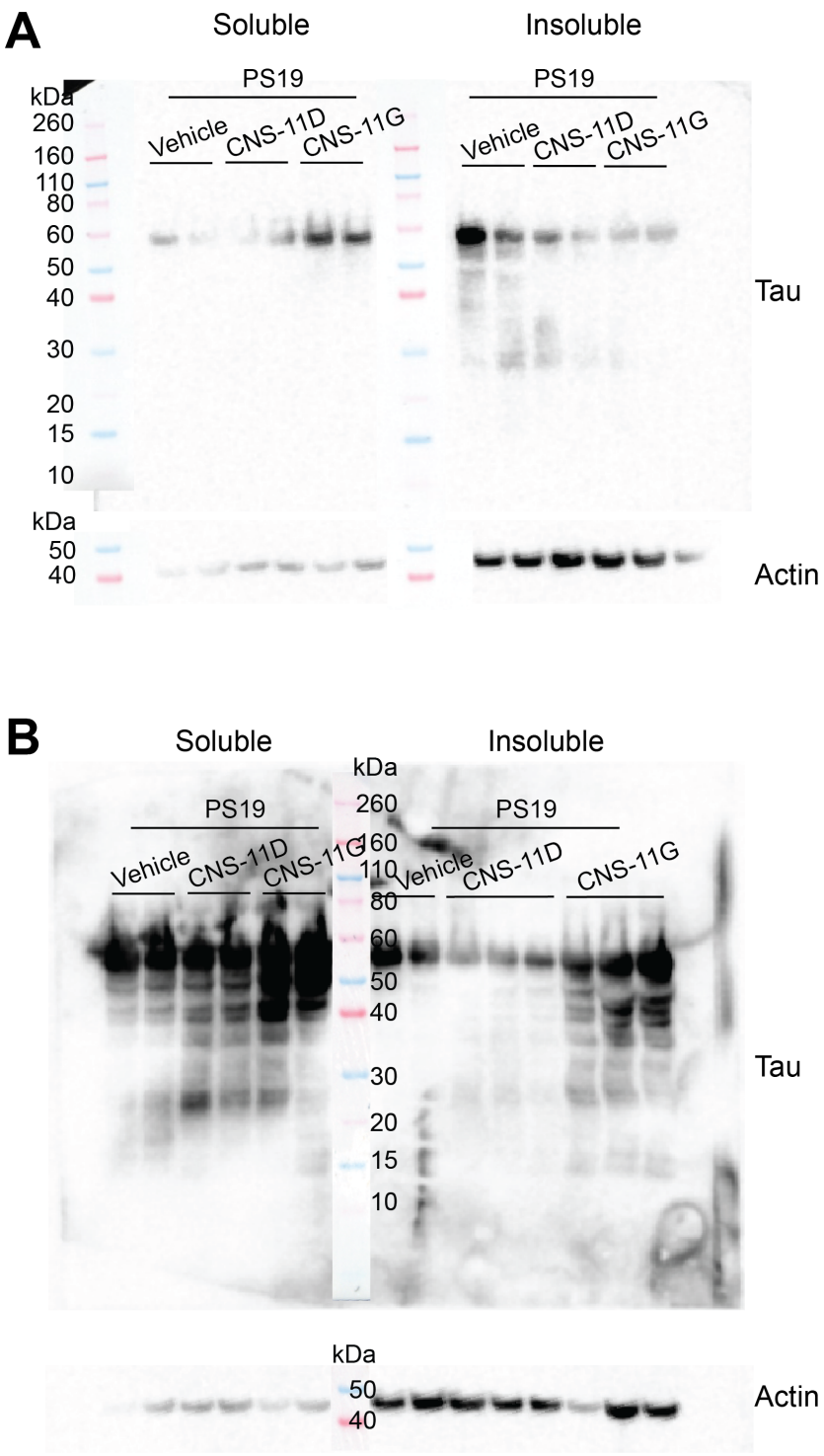


**Supplementary Figure 4. CNS-11D and CNS-11G reduce levels of insoluble tau in PS19 mice. (A-B)** The right hippocampus of PS19 mice treated with vehicle, CNS-11D, or CNS-11G

was homogenized in RIPA buffer, separated into RIPA-soluble and RIPA-insoluble fractions, and analyzed by Western blot analysis. **(A)** Vehicle-treated PS19 mice #1, 2; CNS-11D-treated PS19 mice #1, 2; CNS-11G-treated PS19 mice #1, 2. **(B)** Vehicle-treated PS19 mice #3, 4; CNS-11D-treated PS19 mice #3, 4, 5; CNS-11G-treated PS19 mice #3, 4, 5.

CHAPTER 5

# Conclusion

In the past twenty years, a wealth of atomic resolution structures of amyloid fibrils determined by x-ray crystallography and cryo-electron microscopy have expanded the possibilities for using structure to guide drug design for amyloid-related diseases. In this dissertation research, I characterized three of these structure-based designs as potential diagnostics and therapeutics for AD and PD. First, I characterized magnetic nanoparticles functionalized with an α-syn-targeting peptide and determined that they can be used as an MRI contrast agent to distinguish mice with α-syn pathology from wild-type control mice. Second, I characterized a bivalent nanobody that can inhibit seeding by post-mortem brain extracts from AD patients and determined it can cross the blood-brain barrier in mice. Third, I characterized three small molecules that can disaggregate AD brain-extracted fibrils and determined that they can each reduce levels of aggregated tau in mice with tau pathology.

Together, the studies in this dissertation demonstrate the potential of using structure-based design of diagnostics and therapeutics for diseases caused by the misfolding of amyloid-forming proteins. In the future, it remains to be determined whether these structure-based designs will be useful in the clinic. One aspect in which these designs can be improved is their target-binding affinity, as well as inhibition/disaggregation efficacy for the therapeutic designs. Another aspect is their pharmacokinetic properties: absorption and brain penetration, characterized in these studies, and metabolism and clearance, which have yet to be studied. Importantly, structure-based design is an iterative process. With modifications informed by structural insights and experimental validation, there will be continuous improvements in these and other structure-based designs for amyloid-related diseases.